Flexible and Stretchable Lithium-Ion Batteries Based on Solid Polymer Nanocomposite Electrolyte

A Dissertation

Presented to

the Faculty of the Department of Mechanical Engineering

University of Houston

Partial Fulfillment

of the Requirements for the Degree

Doctor of Philosophy

in Mechanical Engineering

by

Mejdi Kammoun

December 2016

Flexible and Stretchable Lithium-Ion Batteries Based on Solid Polymer Nanocomposite Electrolyte

Mejdi Kammoun

Approved:

Chair of the Committee
Dr. Haleh Ardebili, Associate Professor,Mechanical Engineering

Committee Members:

Dr. Yashashree Kulkarni, Associate Professor, Mechanical Engineering

Dr. Jae-Hyun Ryou, Assistant Professor, Mechanical Engineering

Dr. Dong Liu, Associate Professor, Mechanical Engineering

Dr. Yan Yao, Assistant Professor, Electrical & Computer Engineering

Dr. Suresh K. Khator, Associate Dean, Cullen College of Engineering

Dr. Pradeep Sharma, Department Chair of Mechanical Engineering

Acknowledgements

First and foremost, I would like to thank my advisor, Dr. Haleh Ardebili, for giving me the opportunity to work within her group, and for all the support provided inside and outside the academic work. Her intellectual support at various stages of this work has been invaluable in enabling me to carry this work to completion. I cannot go without expressing my admiration to her genuine ideas and physical intuitions that make her a successful advisor. She always trusted me as an independent researcher and was open to new ideas while making sure our research stayed in the right path.

Second, I would like to thank the chairman of the mechanical engineering department, Dr. Pradeep Sharma, for all his advices and his continuous support.

Third, I would like to acknowledge my committee members, Dr. Yashashree Kulkarni, Dr. Yan Yao, Dr. Jae-Hyun Ryou and Dr. Dong Liu for reviewing my dissertation. All the fruitful discussions, valuable suggestions, and the constructive criticisms have been much appreciated.

I appreciate the financial support from NSF, TcSUH that funded the research discussed in my dissertation.

I would like to acknowledge my talented colleagues: Taylor Kelly and Sean Berg. The creative ideas in this work would never be possible without their contribution.

My Ph.D. student years would not have been so enjoyable without all my actual and previous labmates: Eric Wood, Qin Li, Ahmet Aktürk, Mengying Yuan, Bahar Moradi, Sarah Ardeyani, and William Walker. I greatly appreciate all the support and help I got from them.

I would like to thank my wonderful parents, Mohamed Kammoun and Najia Ben Hamida, for raising me with an open mind and loving me unconditionally. They have inspired me to be curious and have supported me in every single step of my life. I want to add a special thanks to my amazing mother. Without her continuous support and encouragement I would have never been able to achieve my goals. I dedicate this work for her and I hope she will get better soon.

I would also like to thank my sister and brother and their families, Maroua and Mehdi Kammoun for bringing enjoyment and looking after our parents.

Last but not least, I am forever indebted to my new family, in particular, my father in law Monem Hammami, my mother in law Habiba Hammami and my brother in law Firas Hammami for their endless support and confidence.

Finally, a special thank you to my wife and my son; Farah and Rayen Kammoun. Words cannot describe how lucky I am to have them in my life. My little family has selflessly given more to me than I ever could have asked for. I love you, and this work would not have been possible without your presence and support.

Flexible and Stretchable Lithium-Ion Batteries Based on Solid Polymer Nanocomposite Electrolyte

An Abstract

of a

Dissertation

Presented to

the Faculty of the Department of Mechanical Engineering

University of Houston

Partial Fulfillment

of the Requirements for the Degree

Doctor of Philosophy

in Mechanical Engineering

by

Mejdi Kammoun

December 2016

Abstract

The prevalence of flexible electronics including the ubiquitous touch-screens, roll-up displays, implantable medical devices and wearable sensors has motivated the development of high performance flexible energy storage devices. High energy density lithium-ion batteries (LIBs) are the leading candidates to convert into flexible and stretchable batteries to integrate with the flexible and stretchable applications. The ultimate challenge is to obtain mechanical flexibility while conserving the high electrochemical performance of conventional LIBs including high capacity and cycling stability.

In this study, two types of polymer nanocomposite electrolytes are investigated for battery and fuel cell applications. The first polymer studied is based on Nafion, and a key problem in PEMFCs is the dehydration of Nafion and the subsequent low performance especially at higher temperatures. We introduced a bio-friendly coconut shell activated carbon (AC) nanoparticles into the Nafion membranes. We showed that a small amount (i.e., 0.7%) of AC nanofillers could dramatically enhance proton conductivity without significantly compromising the mechanical properties.

The second type of polymer for lithium-ion battery application is based on the polyethylene oxide (PEO)|Li salt system. It offers enhanced safety, stability and thin-film manufacturability compared to the traditional organic liquid electrolytes. The electrochemical properties of the pure polymer are improved by adding 1% graphene oxide (GO) nanosheets. We developed a high performance flexible Li ion battery based on the solid polymer nanocomposite electrolyte. The flexible battery exhibits a capacity

higher than 0.1 mAh cm^{-2} at 1 mA current and excellent cycling stability over 100 charge/discharge cycles.

PEO/GO electrolyte was also incorporated in a novel design of spiral stretchable battery capable of large out-of-plane deformation. The spiral Li-ion battery displays robust mechanical stretchability and an energy density of 4.862 mWh/cm^3 at 650% out-of-plane deformation and provides an average capacity above 0.1 mAh/cm^2 in different stretching configurations.

We also investigated the temperature effects on solid polymer electrolyte based batteries. A 1-D LIB model that predicts the discharge behavior of coin cell batteries at different temperatures was developed. The modeling simulations based on electrochemical-thermal coupling show good agreement with experimental results and provide fundamental insights on the battery operation at different conditions.

Table of Content

Acknowledgements ..... **v**

Abstract ..... **viii**

Table of Content ..... **x**

List of Figures ..... **xiv**

List of Tables ..... **xviii**

CHAPTER 1: INTRODUCTION **1**

1.1 MOTIVATION AND OBJECTIVES 1

1.2 ENERGY STORAGE 2

1.2.1 Overview *2*

1.2.2 Capacitors *3*

1.2.3 Fuel Cells *5*

1.2.4 Batteries *6*

1.3 FLEXIBLE AND STRETCHABLE LITHIUM-ION BATTERY: OVERVIEW AND PROGRESS 14

1.4 MODELING AND SIMULATION OF THE LIB 15

1.4.1 Comsol *16*

1.4.2 Applications and Limits *17*

1.5 METHODS 18

1.5.1 Preparation Techniques *18*

1.5.2 Characterization Techniques *19*

1.6 OUTLINE OF THE DISSERTATION 21

CHAPTER 2: SOLID POLYMER NANOCOMPOSITE ELECTROLYTES **23**

2.1 INTRODUCTION 23

2.2 POLYMER AND LITHIUM SALT SELECTION 24

2.3 IONIC CONDUCTIVITY 24

2.4 NANO-SIZED FILLER 26

2.5 BATTERY APPLICATION 27

2.6 FUEL CELL APPLICATION 28

2.7 POLYETHYLENE OXIDE-GRAPHENE OXIDE NANOCOMPOSITE ELECTROLYTE FOR LITHIUM-ION BATTERY 29

2.7.1 Overview 29

2.7.2 Experimental 30

2.7.3 Results and Discussion 32

2.7.4 Conclusions 38

2.8 NAFION MEMBRANE WITH COCONUT SHELL NANOFILLERS FOR HYDROGEN FUEL CELL 39

2.8.1 Overview 39

2.8.2 Materials and Methods 41

2.8.3 Results and Discussion 45

2.8.4 Conclusions 56

CHAPTER 3: FLEXIBLE THIN-FILM BATTERY BASED ON GRAPHENE-OXIDE EMBEDDED IN SOLID POLYMER ELECTROLYTE 58

3.1 INTRODUCTION 58

3.2 EXPERIMENTAL SECTION 62

3.2.1 Flexible Battery Fabrication 62

3.2.2 Flexible Battery Electrochemical and Mechanical Testing 63

3.3 RESULTS AND DISCUSSION 64

3.4 CONCLUSIONS 69

CHAPTER 4: STRETCHABLE SPIRAL THIN-FILM BATTERY CAPABLE OF OUT-OF-PLANE DEFORMATION 71

4.1 INTRODUCTION 71

4.2 EXPERIMENTAL 74

4.2.1 Stretchable Spiral Battery Fabrication 74

4.2.2 Electrochemical and Mechanical Testing of Spiral Batteries 74

4.3 RESULTS AND DISCUSSION 75

4.4 CONCLUSION 81

CHAPTER 5: TEMPERATURE EFFECTS IN NANOCOMPOSITE POLYMER BASED LITHIUM-ION BATTERIES 82

5.1 INTRODUCTION 82

5.2 EXPERIMENTS 84

5.2.1 Coin Cell Battery Fabrication 84

5.2.2 LIB Electrochemical and High Temperature Testing 84

5.3 1D ISOTHERMAL MODEL 84

5.3.1 Nomenclature 84

5.3.2 Model assumptions 85

5.3.3 Governing Equations 86

5.4 RESULTS AND DISCUSSION 91

5.5 CONCLUSIONS 96

CHAPTER 6: CONCLUSIONS AND FUTURE WORK 97

6.1 CONCLUSIONS 97

6.1.1 Polymer Nanocomposite Electrolytes for Battery and Fuel Cell Applications. 97

6.1.2 Polymer Based Flexible Battery 98

6.1.3 Polymer based Spiral Stretchable Battery 99

6.1.4 Modeling and Simulations 99

6.2 FUTURE WORK 100

6.2.1 Enhancement of the Ionic Conductivity Model for the Nafion/AC Electrolyte 100

6.2.2 Enhancement of the Properties for the Solid Polymer Electrolyte and the Performance of the Flexible and Spiral LIBs. 101

6.2.3 Improvement of the Simulation Model 102

REFERENCES **103**
APPENDIX A **128**
APPENDIX B **131**
APPENDIX C **141**
APPENDIX D **144**

List of Figures

Figure 1-1: General categories of energy storage technologies (Courtesy of H. Ardebili). 4

Figure 1-2: Schematic representations of (a) capacitor and (b) fuel cell. 6

Figure 1-3: Comparison of the rechargeable battery technologies as a function of volumetric and specific energy density [10]. 7

Figure 1-4: Surface Scanning electron micrographs (SEM) of (a) graphite (b) Celgard 2325 (PP/PE/PP) separator [14](c) liCoO_2. Schematic representation of a LIB, (d) the while the battery is charging and (e) while the battery is charging 9

Figure 1-5: Voltage versus capacity for positive and negative electrode materials for LIB [6]. 12

Figure 1-6: (a) Schematic open-circuit energy diagram of an aqueous electrolyte.**(b)** Schematic of the relative positions of the Fermi energy in an itinerant electron band for $LixC_6$ and the Co^{4+}/Co^{3+}redox couple for $LixCoO_2$ [4]. 14

Figure 2-1: Schematic of the ionic conductivity mechanism within (a) Pure and, (b) Nanocomposite polymer electrolyte 26

Figure 2-2: Polarization light microscopy (PLM) of (a), (c) pure PEO and (b), (d) PEO/1 wt% GO. Scanning electron microscopy images of (e) GO powder and (f) PEO/1 wt% GO. 33

Figure 2-3: (a) Li salt dissociation fractions of polymer electrolyte films (b) Melting point (Tm) and glass transition temperature (Tg) [79]. 34

Figure 2-4: (a) Thermogram comparison of solid PEO/1%GO and organic liquid

electrolyte, (b)-(d) liquid electrolyte flammability test, (e) image of the PEO/1 wt%GO film, and (f)-(h) solid PEO/1 wt%GO flammability test. 35

Figure 2-5: Current–voltage response of full cell batteries made with different type of electrolytes obtained at room temperature. 36

Figure 2-6: (a)A.C. impedance spectra of PEO|LiClO4 and PEO|LiClO4 +1 wt%GO electrolytes (b) Fitting circuit..... 37

Figure 2-7: DC polarization of the symmetric cell based on the PEO| LiClO4 and PEO| LiClO4 +1 wt%GO. 38

Figure 2-8: The chemical structure of PFSA Nafion membrane and a depiction of nanochannel[102]..... 40

Figure 2-9: Scanning electron microscopy (SEM) image of (a) coconut shell activated carbon (AC) powder, (b) Nafion nanocomposite with 15 wt% AC, and (c) with 0.5 wt% AC [102]. 44

Figure 2-10: Mechanical properties of pure and composite Nafion membranes at room temperature and 50 % RH: (a) tensile modulus, (b) Nafion/AC membrane under DMA tensile testing, and (c) stress– strain curves..... 45

Figure 2-11: (a) Water sorption and (b) ion conductivity of pure and composite membranes [102]. 46

Figure 2-12: Nyquist plot for different contents of AC (0.5 and 0.7 wt.%, top inset) with the equivalent model circuit at (a) room temperature and (b) 70 °C [102]. 49

Figure 2-13: (a) Schematics of AC nanoparticles inside Nafion, (b) the proposed mechanisms of conductivity enhancement and adverse effects plotted separately, and (c) our model fitted to the experimental data [102]. 54

Figure 3-1: (a) Images of flexible Li ion battery based on solid PEO/1%GO electrolyte powering an LED, (b) schematics of the flexible LIB materials and configuration. 61

Figure 3-2: (a) SEM image of the cross-section of the flexible LIB, (b) impedance spectra of flexible LIB based on pure PEO and PEO/1 wt% GO, compared in the first charge/discharge cycle and (c) after 100 cycles. 63

Figure 3-3: (a) Cyclic voltammetry of the flexible batteries, (b) voltage vs. capacity for each battery, (c) discharge capacity during 100 cycles, and (d) coulombic efficiencies of the flexible batteries, discharged at 1 mA (2C) at room condition. .. 65

Figure 3-4: (a) Flexible LIB (based on PEO/1 wt% GO electrolyte) subjected to cyclic bending and in situ voltage measurements, and (b) voltage retention vs. bending cycle number at a speed of 8 mm s^{-1}**.** 66

Figure 3-5: (a) Stresses in flexible LIB after the lamination process, (b) a flexible LIB being fed into the lamination machine, (c) bending stresses in flexible battery based on PEO/1 wt% GO electrolyte, and (d) Contact pressure vs. bending curvature in LIBs [159]. 68

Figure 4-1: (a)-(b) The schematics of the spiral Li-ion battery, (c)-(d) photo image of the fabricated spiral battery in stretched positions lighting a red LED, (e) spiral battery in flat position [173]..... 73

Figure 4-2: Cyclic voltammetry of the spiral battery under flat and stretched conditions [173]. 76

Figure 4-3: (a) Discharge capacity during 100 cycles, (b) coulombic efficiencies of the spiral batteries, (c) capacity vs. stretching distances, (d) impedance spectra for unstretched (flat) and stretched batteries (d) in fresh condition 78

Figure 4-4: (a) The voltage retention vs. stretching cycle number of spiral LIB at a speed of 1000 mm/min, (b) image of the spiral LIB subjected to cyclic bending and in-situ voltage measurements [173]. 79

Figure 4-5: (a) Finite element model of spiral battery (b) strain variation in stretched spiral battery (c) stress variation in spiral battery, (d) cross-sectional force variation indicating the state of torsion in the spiral battery [173]. 80

Figure 5-1: Equilibrium potential vs SOC for (a) $LiCoO_2$ and (b) graphite. 88

Figure 5-2: Temperature dependence of ion conductivity (1 wt% GO content)[79]..... 92

Figure 5-3: High Temperature cycling profile of the battery based on nanocomposite electrolyte (PEO+1 wt% GO) with plasticizer. 94

Figure 5-4: Comparison of the simulated results of the battery based on the nanocomposite electrolyte with the experimental data at different temperatures..... 95

List of Tables

Table 1-1. Characteristics of Commercial Battery Electrode Materials [18]..... 11

Table 2-1. The transference numbers of the PEO| $LiClO_4$ and PEO| $LiClO_4$+ 1 wt%GO 38

Table 2-2. Proton conductivities of pure and composite membranes at room temperature 43

Table 2-3. Proton conductivities of pure and composite membranes at 70^{o}C 44

Table 2-4. Comparison of selective studies on ion conductivity and water uptake of proton exchange membranes..... 50

Table 5-1. Model parameter values for the coin cell battery based on nanocomposite electrolyte..... 91

Chapter 1: Introduction

1.1 Motivation and Objectives

Energy storage continues to retain an important role in the global market, especially with the rise in need for portable devices, like cell phones, tablets and laptops, and the expected depletion of conventional hydrocarbon resources. This expanding demand has prompted energy storage requirements including smaller size, lighter weight, improved safety and stability to meet the perpetually expanding and multifaceted requests of the 21st century consumer.

Lithium-ion battery (LIB) technology, available in the market since 1991, has demonstrated its ability to provide large-scale energy storage due to its high energy density, high output voltage and long life operation. These strong characteristics are useful in applications including remote area and back up power supplies, distributed power generation and an array of portable electronics. However, the revolution in the microelectronic industry requires the adaptation of LIBs to fit into thin, portable and deformable electronics, which has not yet been achieved and is causing a bottleneck in the advancement of portable electronics.

The tremendous business opportunity in LIB advancement within the mobile device industry elevates researchers and specialists to find new materials and structures for designing advanced LIBs. Other than the general necessities from the energy storage point of view, the mechanical adaptability of LIBs has likewise pulled in expanding consideration.

The primary objective of this research is to seek new materials and designs for advanced flexible and stretchable energy storage devices. Two types of polymer nanocomposite electrolytes with enhanced properties were investigated for applications in batteries and fuel cells. A potentially suitable solid polymer nanocomposite electrolyte was fabricated and characterized for battery application that can offer the necessary mechanical stability for flexible and stretchable LIBs while conserving the overall electrochemical performance of the battery. The development of mathematical and simulation models was another imperative goal in this research to provide critical insights into the evolution of the mechanical behavior, enhancement mechanisms and the diminution of the experimental work and cost.

1.2 Energy Storage

1.2.1 Overview

The acceleration in technological development has opened the door to continuous international economic growth and has in fact allowed the world to achieve energy sustainability using a wide range of energy sources.

In 2012, the Energy Information Administration (EIA) estimated that primary energy sources worldwide consisted of petroleum 34.6%, coal 28.0%, and natural gas 23.6%, amounting to an 86.3% share for fossil fuels. Although fossil fuels are constantly being formed via natural processes, they are, for the most part, thought to be non-renewable resources because they take many years to form and the known possible reserves are being exhausted faster than the emerging ones [1].

In addition, the use of fossil fuel raises serious ecological concerns. The burning of fossil fuels produces around 21.3 billion tons (21.3 gigatons) of carbon dioxide (CO_2) per

year, however, it is estimated that natural processes can absorb only half of that amount, so there is a net increment of 10.65 billion tons of atmospheric carbon dioxide every year [1]. CO_2 is a greenhouse gas that contributes to global warming, causing the average temperature of the Earth to ascend accordingly, which will lead to major and adverse impacts on the environment. A global development toward the era of renewable energy is underway to help reduce international greenhouse gas emissions [2].

The implementation of renewable energy sources has not yet been perfected and has suffered setbacks in efficiency, reliability, cost effectiveness and availability [3-5]. Therefore, energy management is a key element for the success of the exploitation of green resources. Energy storage is the solution to grid-scale frequency balancing and consumption stability by storing energy generated from renewable resources for use during high-peak hours when energy consumption is more significant [6]. In addition to large-scale energy needs, the necessity for advanced energy storage solutions is evident in the electric vehicle and consumer gadgets industries. **Figure 1.1** presents the most recognized energy storage devices [6]. In the next section, the most commonly used energy storage devices – capacitors, fuel cells and batteries are discussed.

1.2.2 Capacitors

A capacitor is a passive electronic component that stores energy in the form of an electrostatic field. In its simplest configuration, a capacitor consists of two conducting plates separated by a non-conductive material known as a dielectric **(Figure 1.2.a) [7].**

The capacitance is directly proportional to the surface areas of the plates, and is inversely proportional to the separation distance between the plates. Capacitance also depends on the dielectric constant of the material separating the plates [8], and is defined

as

$$C = \frac{A}{\varepsilon d}, \tag{1.1}$$

where **ε** is the dielectric permittivity, **A** is surface area and **d** is the distance between the two plates. According to this equation, considering the small spacing between the two charged surfaces, the capacitance would be significantly increased. This is how the energy storage is predominantly achieved in the case of electric double-layer capacitors (EDLC). The separation of charge distance in a double-layer capacitance is on the order of a few Angströms (0.3 - 0.8 nm).

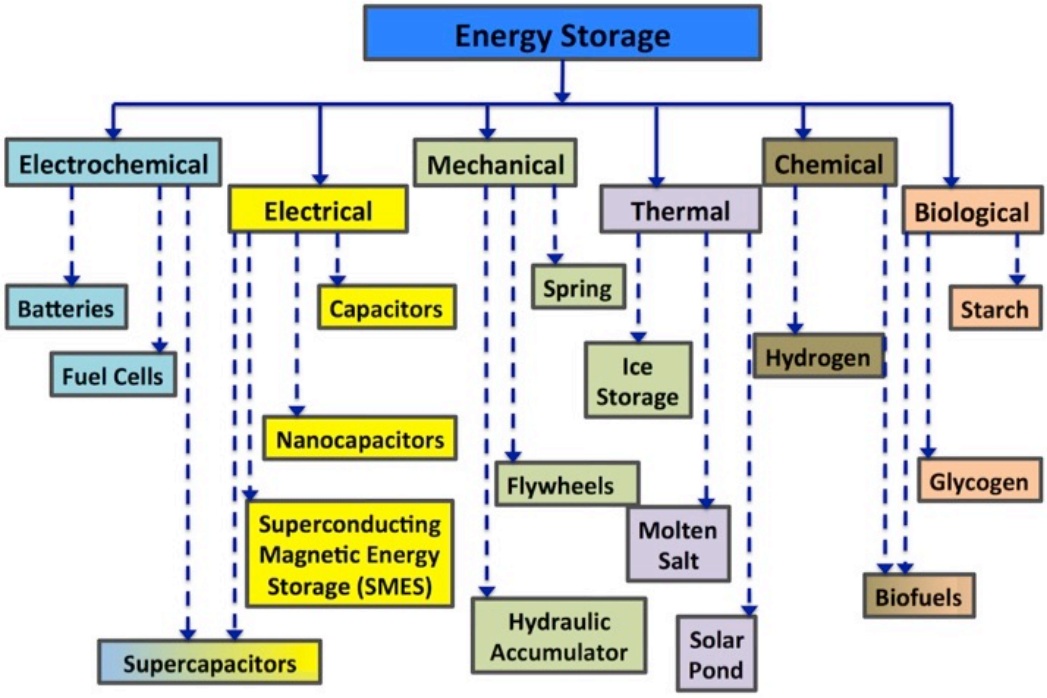

Figure 1-1: General categories of energy storage technologies (Courtesy of H. Ardebili).

The capacitance of a supercapacitor is determined by another type of storage principle, which is the pseudocapacitance. The storage of the electrical energy is achieved

by redox reactions or intercalation on the surface of the electrode by ion absorption that results in a reversible faradaic charge-transfer on the electrode.

Supercapacitors can be fully charged and discharged over a few seconds and supply a low energy density of about 5 $Wh.kg^{-1}$ and a much higher power density (10 $kW.kg^{-1}$). They can replace or compliment batteries in electrical energy storage based on the application needs [8].

1.2.3 Fuel Cells

A fuel cell is an electrochemical device that transforms chemical energy from a fuel (commonly hydrogen) into electricity through chemical reactions occurring at the electrodes. In this process, fuel is continuously passed over a porous cathode that splits the fuel to positive and negative ions. The electrons pass through an external circuit whereas the positive ions (after passing through a liquid or membrane electrolyte) travel to a porous anode to be combined with oxygen to create water or carbon dioxide. Fuel cells achieve a high efficiency compared to the other energy storage devices **Figure 1.2.b** [9].

The main difference between fuel cells and batteries is that fuel cells require a permanent source of fuel and oxidizing agent to maintain the chemical reaction, which makes them an open system. Batteries, on the other hand, are a closed system where the chemicals react with each other to produce an electromotive force. Fuel cells can deliver energy persistently as long as the fuel inputs are supplied [9].

Proton exchange membrane fuel cells (PEMFCs) have captured considerable attention in recent years due to their higher energy density, renewability and environmental friendliness. Upon the ionization of hydrogen and oxygen in the hydrogen

fuel cell, the protons must transport through a membrane referred to as proton exchange membrane (PEM) and then, combine with oxygen ions to produce water. This membrane can play a critical role in the fuel cell. In the next chapter, the Nafion membrane filled with activated carbon (AC) nanoparticles was investigated and show that enhanced water sorption and ion conductivity can be achieved.

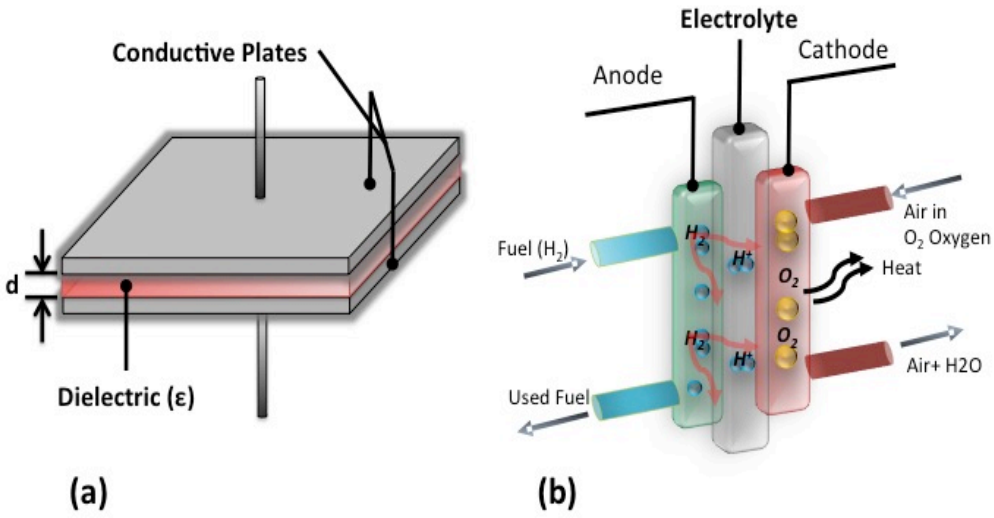

Figure 1-2: Schematic representations of (a) capacitor and (b) fuel cell.

1.2.4 Batteries

Batteries are transducers that convert the chemical energy to the electrical energy and vice versa. The main components of any battery are an anode, cathode and the electrolyte. Batteries can be classified into primary and secondary categories:

- Primary batteries (non rechargeable) irreversibly transform chemical energy into electrical energy. At the point when the supply of reactants is depleted, energy cannot be restored to the battery.
- Secondary batteries (reversible) can be recharged; they can be switched by

supplying electrical energy to the cell, roughly reestablishing their initial composition.

All types of batteries are usually composed of three main components: a positive (cathode) and a negative electrode (anode) separated by a separator and electrolyte. During discharging, the electrochemical reactions occur at the cathode and the anode, generating electrons and enabling the current flow in the external circuit. In the case of rechargeable batteries, during charging, an external voltage or current is applied to the terminals and reverse the movement of electrons and reactions at the electrodes and the energy storage.

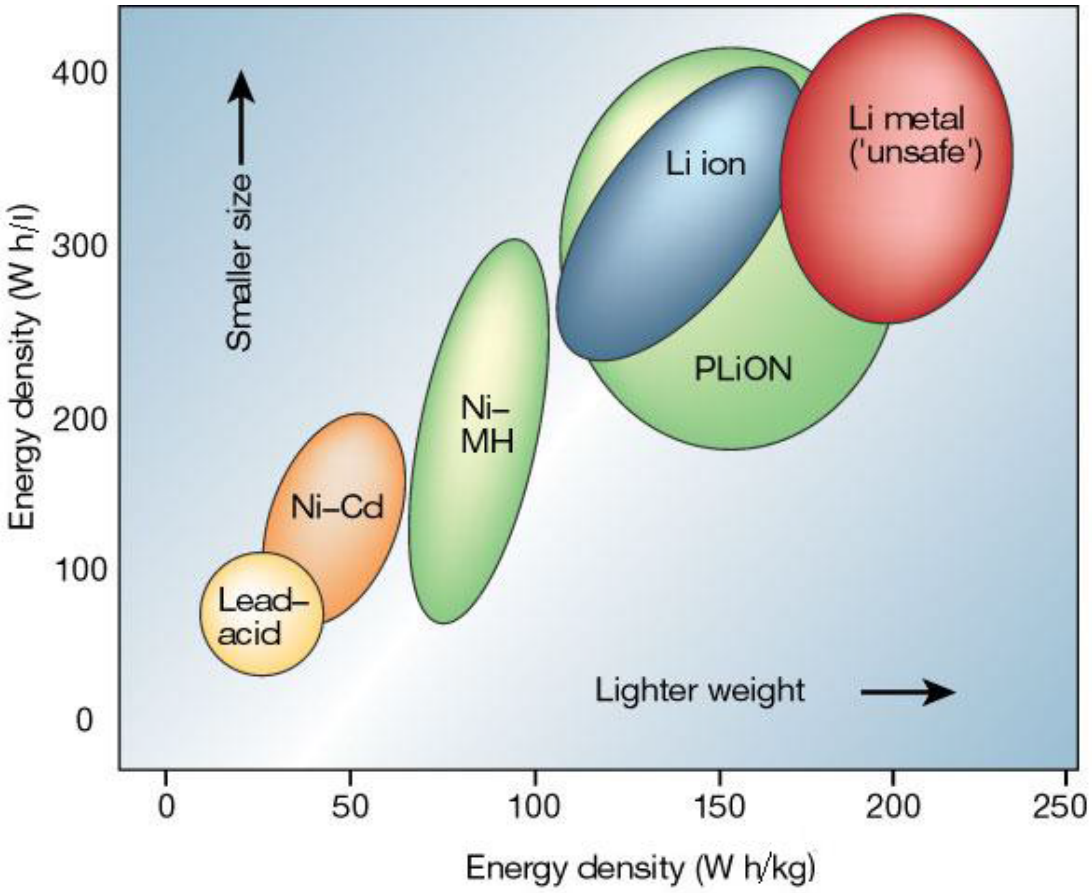

Figure 1-3: Comparison of the rechargeable battery technologies as a function of volumetric and specific energy density [10].

Since the cyclability is one of the most desired factors for different applications like the electrical vehicles (EVs) and portable electronic, herein, this work will focus on the secondary type of battery. According to the mechanisms and components of their electrodes, rechargeable batteries can be further separated into the following categories: lead-acid, zinc-air, nickel-cadmium, nickel-hydrogen, sodium-sulfur, sodium-nickel-chloride, and lithium-ion. Nevertheless, common problems exist in these types of batteries: safety issues, low energy density, slow recharging, low cyclability, adverse environmental impact, and expense [11].

1.2.4.1 Lithium-Ion Batteries

LIBs have been one of the most important energy storage systems for a wide variety of applications because they offer many advantages compared to the other commercially available secondary batteries like high voltage, low self-discharge, long cycling life, low toxicity, and high reliability [12]. Owing to almost unmatched volumetric energy density, Li-based batteries have dominated over other energy storage technologies. In other words, rechargeable LIBs offer high energy densities and up to 6 times higher power densities than lead acid, Ni-Cd, Ni-MH batteries (**Figure 1.3**).

A standard LIB, shown in **Figure 1.4**, consists of a cathode (positive) and an anode (negative), together with an electrolyte and a separator. The separator has two main functions: preventing electrodes from direct contact to avoid a short circuit and allowing the transfer of lithium-ions. The most common separator for LIBs is a glass membrane [13]. It is usually made of a single layer polyolefine with a thickness of 15 ~ 40 μm and the porosity of more than 40%. This type of membrane has a good balance of rigidity and flexibility.

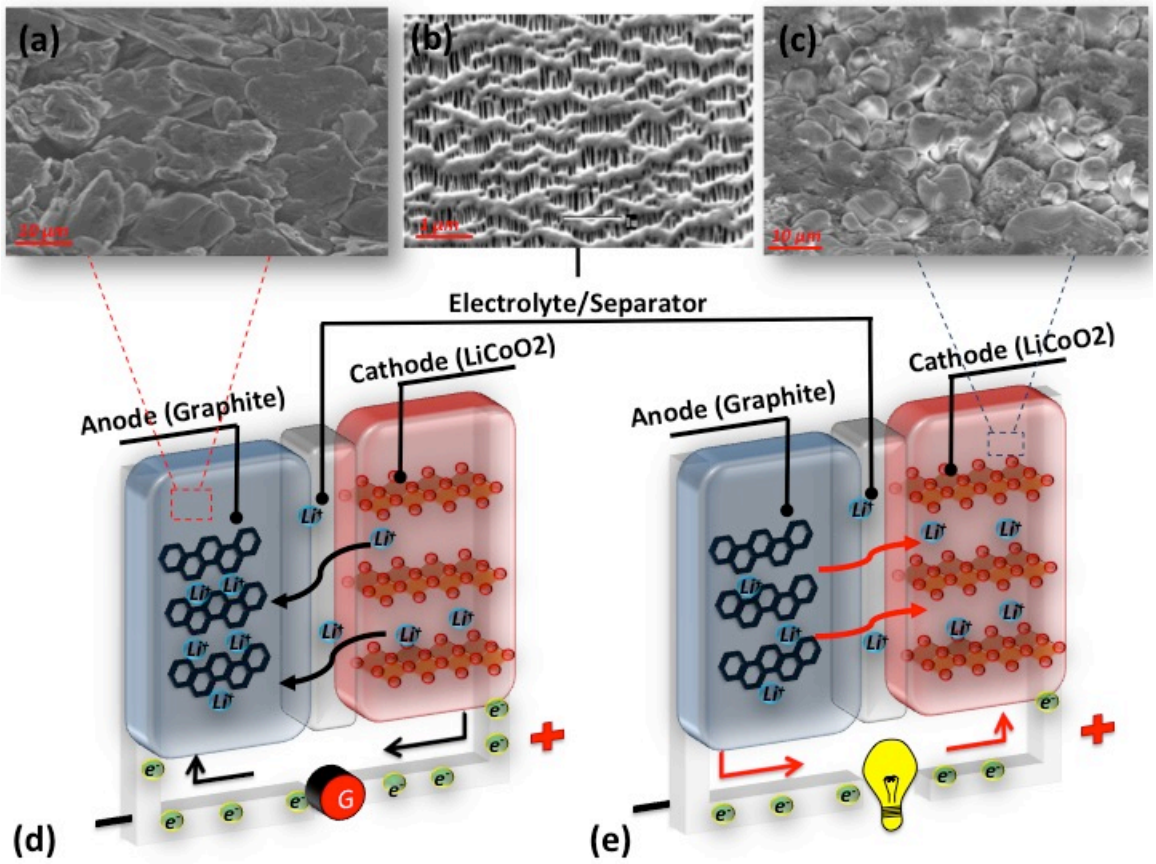

Figure 1-4: Surface Scanning electron micrographs (SEM) of (a) graphite (b) Celgard 2325 (PP/PE/PP) separator [14](c) $liCoO_2$. Schematic representation of a LIB, (d) the while the battery is charging and (e) while the battery is charging

1.2.4.2 Standard Electrodes for LIB

Lithium, 'Li,' is desirable element for use as a battery anode due to its strong electronegative potential (-3.04 V vs. standard hydrogen electrode) and its lightweight property (molar mass M = 6.94 $g.mol^{-1}$, and density $\rho = 0.53$ $g.cm^{-3}$).

In the 1970's, the assembly of primary Li cells first demonstrated the advantage of using Li metal [15]. Lithium metal rechargeable cells could have the highest energy of all battery systems. Unfortunately, during recharge, lithium has a strong tendency to form mossy deposits and dendrites at the anode surface, especially in battery systems using

conventional liquid organic solvents. This limits the battery life to 100-150 cycles (considerably lower than the 300 cycles required for a commercial cell), as well as increasing the risk of safety incidents [16]. Lithium metal is extremely reactive and the key to control its reactivity and build a stable battery chemistry is the identification of a solvent system that spontaneously forms a very thin protective layer on the surface of the metallic lithium, called the solid electrolyte interphase (SEI) layer. This passivation layer is electrically insulating and allows lithium-ion transport. Lithium batteries show higher energy density than alkaline cells, but have a lower rate capability because of the lower conductivity of nonaqueous electrolytes and the low lithium-ion transport rate through the SEI.

In **Figure 1.5** the output voltage values for Li-ion cells or Li-metal cells is represented. It is clear that there is a vast difference in capacity between Li metal and the other negative electrodes, which is the reason for the great interest in solving the problem of dendrite growth [6].

A breakthrough in the LIB industry came with the invention of carbon-based materials for anodes as a substitute to Li metal anodes. The typical negative electrode (anode) material can be grouped into several categories: insertion-type materials (C, TiO_2, etc.), alloying-type materials (Si, Sn, etc.), which offer the highest gravimetric capacity (mAh/g), and conversion-type materials (iron oxides, nickel oxides, cobalt oxides, etc.). Positive electrode (cathode) materials for LIBs are layer-structured metal oxides containing Li (such as $LiCoO_2$), olivine structured materials (such as $LiFePO_4$) and tunnel-structured materials (such as $LiMn2O_4$). Goodenough was the first who proposed the families of lithium metal oxide ($LixMO_2$) compounds [5, 17].

In **Table 1.1**, we have listed the most common commercial positive and negative electrode materials.

Table 1-1. Characteristics of Commercial Battery Electrode Materials [18]

	Potential vs. Li/Li^+(V)	**Specific Capacity, (mAh/g)**	**Advantages**	**Disadvantages**
Positive Electrodes				
$LiCoO_2$	3.9	140	Performance	Cost and resource limitations of Co, low capacity
$LiMn_2O_4$	4.1	100–120	Low cost and abundance of Mn, high voltage, moderate safety, excellent rate performance	Limited cycle life, low capacity
$LiFePO_4$	3.45	170	Excellent safety, cycling, and rate capability, low cost and abundance of Fe, low toxicity	Low voltage and capacity (substituted variants), low energy density
Negative Electrodes				
Graphite	0.1	372	Long cycle life, abundant	Relatively low energy density; inefficiencies due to Solid Electrolyte Interface formation
$Li_4Ti_5O_{12}$	1.5	175	"Zero strain" material, good cycling and efficiencies	High voltage, low capacity (low energy density)

Because the carbon negative electrode is empty from Li when the battery is first assembled, the positive electrode must act as the source of Li; this is why the positive electrode limits the overall capacity of the battery. For instance, taking $LiCoO_2$ as a cathode and graphite C as an anode in a typical LIB, the complete chemical reactions are described as follows:

At the cathode: $LiCoO_2 - Li^+ - e^- \leftrightarrow Li_{0.5}CoO_2$ // 143 mAh/g

At the anode: $6C + Li^+ + e^- \leftrightarrow LiC_6$ //372 mA3h/g

Overall reaction: $C + LiCoO_2 \leftrightarrow LiC6 + Li_{0.5}CoO_2$

According to these equations, we can notice that the electrode materials play key roles in determining the performance of LIBs.

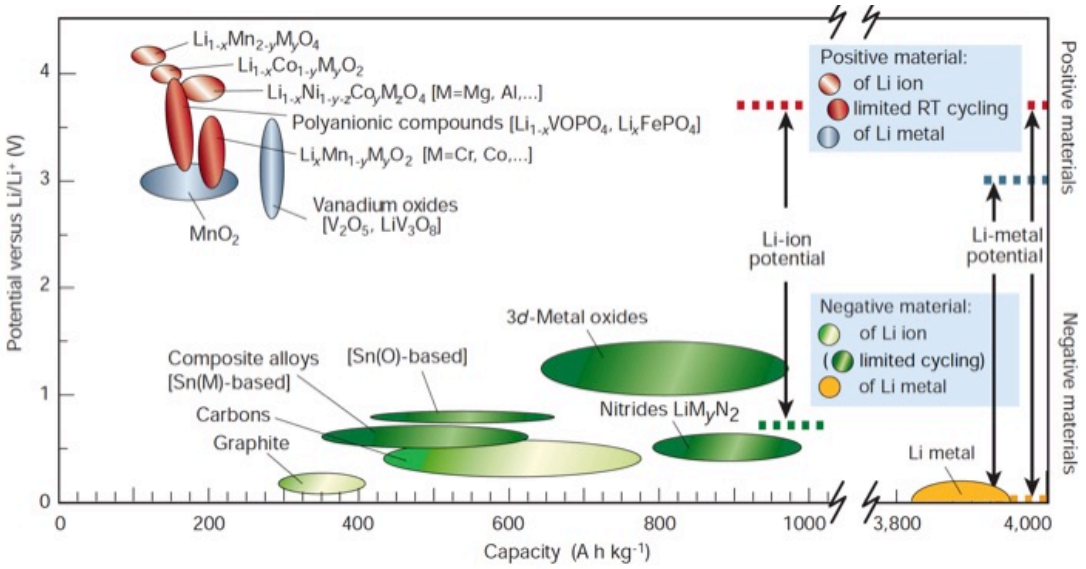

Figure 1-5: Voltage versus capacity for positive and negative electrode materials for LIB [6].

1.2.4.3 Electrolytes

The electrolyte, which is the key component for Li^+ ion transportation during charge/discharge cycling, consists of a lithium salt and its hosting material. So far several different electrolyte systems have been developed, such as liquid, gel, ceramic, ionic liquid and solid polymer [19]. Among all these, the most widely used electrolyte is the non-aqueous liquid electrolyte, for instance, LiPF6 salt in ethylene carbonate (EC) and diethyl carbonate (DEC), due to its superior Li^+ ion conductivity at room temperature.

The electrolyte should not undergo any chemical changes during operation, and all reactions are expected to occur within the electrodes. Ideally, a perfect electrolyte should satisfy the following criteria:

- It should be an excellent ionic conductor and electronic insulator to ensure Li+ ion transport, avoid short circuiting and keep self-discharge at a minimum level;

- It should have a wide electrochemical window and be able to generate a stable passivation layer (SEI) to block the electron transfer at the surface of the electrodes. Figure 1.6.a presents an open-circuit energy diagram of an aqueous electrolyte and electrodes. This figure explains the mechanism of the electrolyte degradation. The operational window "Eg" of the electrolyte is the energy difference between its lowest unoccupied molecular orbital (LUMO) and its highest occupied molecular orbital (HOMO). The electrolyte will be oxidized if the electrochemical potential of the cathode "μc" is below the HOMO. The reduction of the electrolyte occurs on the side of the anode if the electrochemical potential of the anode "μA" is above the LUMO of the electrolyte [4]. The determination of the energy of a given μA or μC corresponds to the Fermi energy in an itinerant-electron band, as is the case for graphite, or the energy of a redox couple of a transition-metal cation like Co4+/Co3+ presented in **Figure 1.6.b**.
- It should be inert to other cell components such as the current collectors, separator, and cell packaging materials;
- It should be thermally stable and safe, especially for the case of the flammable electrolytes;
- It should be environmentally friendly and abundant;
- It should be cheap and the syntheses and fabrication processes should be simple as possible.

The choice of the solid polymer electrolyte to fabricate the different prototypes in this study is founded on its mechanical properties compared to the other classes of

electrolytes. In addition, the solid polymer electrolyte offers many advantages including safety, stability and simple manufacturability. However, one of the considerable challenges is related to the enhancement of ionic conductivity of the solid polymer electrolyte (SPE). Ion conductivity suffers at Room Temperature RT (10^{-8} S cm^{-1}) compared to liquid electrolyte (> 10^{-2} S cm^{-1}). Furthermore, non-ideal interfacial contact results in low utilization of the of the electrode materials. More details about the SPE will be presented in the next chapter.

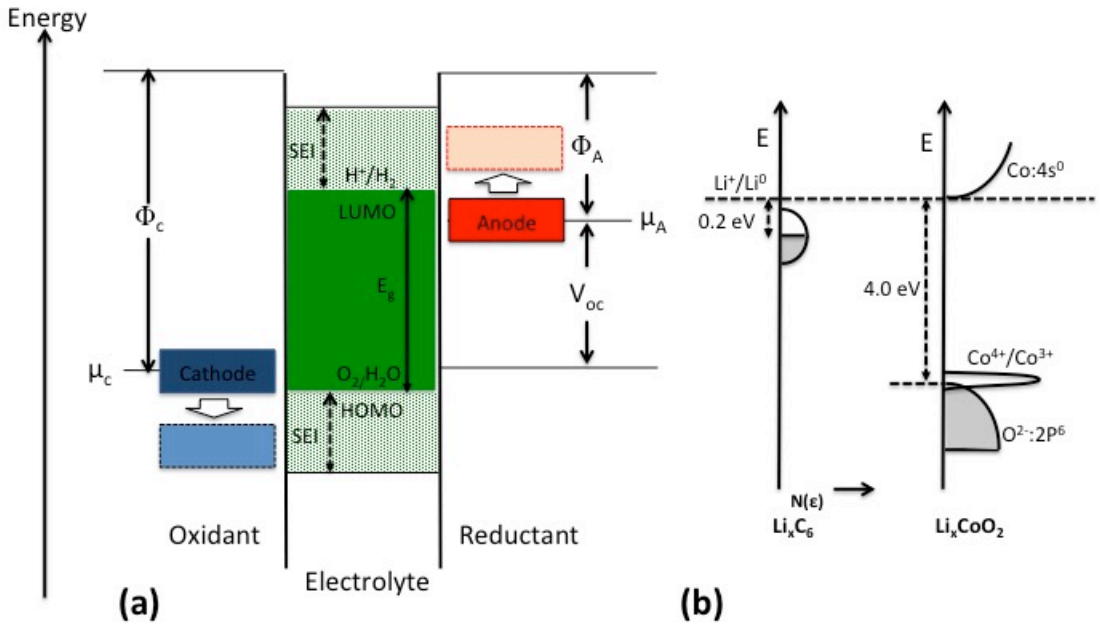

Figure 1-6: (a) Schematic open-circuit energy diagram of an aqueous electrolyte.**(b)** Schematic of the relative positions of the Fermi energy in an itinerant electron band for $LixC_6$ and the Co^{4+}/Co^{3+}redox couple for $LixCoO_2$ [4].

1.3 Flexible and Stretchable Lithium-Ion Battery: Overview and Progress

The enthusiasm for developing ultrathin, flexible, stretchable and safe LIBs for

applications like wearable and [20] rollup devices is opposed by the manufacturing difficulty[21-24]. The difficulty lies in the fabrication of a durable battery that satisfies the requirements set forth by deformable device applications while ensuring battery longevity. Several designs have been proposed to assemble a stable and robust device [20-23, 25, 26].One being the creation of a single structure battery, which would eliminate sliding, or shifting of the different battery components. However, this method is also faced with high fabrication costs and difficult in finding alternative materials that could satisfy the mechanical integrity requirement. The second proposed design approach calls for the fabrication of separate stretchable and flexible components, such as the electrodes and the electrolyte, which are later assembled. Recently, nano-engineered materials like metal oxide nanowires [27, 28] and carbon materials including CNTs [25, 29-32], carbon nanofibers and graphene [33-35] have been demonstrated for use as battery electrode or current collector [36] materials in flexible LIB and have shown good electrochemical performance. Another major breakthrough in the development of flexible LIBs occured with the progress of high performance flexible SPEs [11, 37-45]. Furthermore, flexible batteries must possess a rational assembly process that incorporates a hermetic and flexible seal [21].

In the current work we propose to incorporate the fundamental parts of the LIB into a single cell to generate a thin-film that represents a mechanically flexible or stretchable energy storage device.

1.4 Modeling and Simulation of the LIB

Experimental analyses is an expensive and time consuming, yet necessary, process for investigating new phenomena and discovering how LIBs are impacted by the

implementation of novel findings in materials science. Using computational modelling and simulations to supplement experimental analyses can lead to significant time and cost savings. Computational methods and analyses play an important role in the investigation of novel designs and providing mechanistic insights.

Mathematical models are able to simulate the performance of LIB cells and were first published early in the 1990s by Professor Newman at the University of California [46]. These models are based on electrochemical and thermodynamic concepts and they describe the processes that take place in the battery during operation.

In the current thesis, a theoretical study was conducted to build a model that provides insight into some physical mechanisms and describes the behavior of particular battery properties. Although, models are usually in the form of complex mathematical equations, the theoretical validation of the model could be proficient by comparing the modeling results with experimental data. In the present study COMSOL is used as a simulation tool to solve our mathematical model.

1.4.1 Comsol

This work investigates the behavior of the SPE-based LIB at elevated temperatures and proposes an electro-thermal coupling model.

Thermal management is crucial for improving the charge–discharge efficiency and cycling life of LIB. A mathematical model coupling electronic conduction, energy balance and electrochemical mechanisms is developed. The solution of the model is obtained using the finite element commercial software COMSOL MULTIPHYSICS® (Version 5.0).

COMSOL is a powerful simulation tool that can be used for modeling all types of

batteries, with the most robust features for simulating the electrochemical behavior [47-49]. In this work, we used the Partial Differential Equation PDE interface in COMSOL to investigate the diffusion of lithium in the active material particles (cathode and anode) which is described by Fick's second law

$$\frac{\partial c_s}{\partial t} = \nabla.(D_s \nabla c_s), \tag{1.2}$$

where $\mathbf{c_s}$ is the concentration of lithium in the solid particles and $\mathbf{D_s}$ is the solid phase diffusion coefficient.

1.4.2 Applications and Limits

COMSOL is a user-friendly multiphysics software [49] that allows for the coupling of different physical interfaces and integrates the simulation results of one model to another in order to explore additional physical phenomena. This model demonstrates the discharge process of a LIB for a given set of material properties under specific conditions. Battery developers can use the model to investigate the influence of various design parameters such as operation temperatures, materials, dimensions, and particle size of the active materials.

However, there are always some limitations associated with any mathematical solver [49]. The accuracy of a numerical method depends upon the complexity of the model equations, including initial and boundary conditions, and the numerical algorithm. Another major disadvantage is that the user cannot modify COMSOL's numerical implementations and generally when optimization fails while using COMSOL-like codes, detective work is required to determine whether the numerical simulation was robust enough to provide accurate numerical results.

1.5 Methods

1.5.1 Preparation Techniques

1.5.1.1 Polymer Electrolyte Film Preparation

The polymer electrolyte used for the different battery prototypes presented in this work was prepared using solution-casting technique. This method was selected based on the materials involved, the fabrication simplicity and the sample form.

The preparation process includes the following steps:

- Dispersion of the polymer in non-aqueous acetonitrile. For fuel cell application, Dimethylformamide (DMF) was used as solvent for Nafion.
- Addition of the Li salt (LiClO4) in the SPE for battery application.
- Dispersion of filler in the mixture for the SPNE
- Mixing by means of a stirrer and ultrasonic equipment to disperse the particles homogeneously throughout the polymer matrix
- Casting the mixture on a substrate
- Drying in vacuum
- Storage in an inert atmosphere (argon for PEO and Deionized (DI) water for Nafion).

1.5.1.2 Battery Fabrication

Aluminum foil coated with $LiCoO_2$ (cathode) and copper foil coated with graphite (anode) both with a ~0.1 mm total thickness were purchased from MTI Corporation.

All components of the LIB were stacked onto two commercial sheets of plastic paper with a simple lamination process inside the glove box. Lightweight copper tape was used as current collectors for both the anode and cathode and were bonded on the battery

electrode materials using the adhesive face of the copper.

1.5.2 Characterization Techniques

1.5.2.1 Morphological Characterizations

Scanning Electron Microscopy (Zeiss, Model: Leo 1525 Gemini) and Polarized Light Microscopy (PLM) (Advanced EPI Trinocular Inffinity Polarizing Microscope 50x-1600x) were used to investigate the morphology and the structure of the SPEs.

1.5.2.2 Electrochemical Characterizations

Electrochemical Impedance Spectroscopy (EIS) (Autolab FRA module) is a technique to measure the impedance of the SPE. During EIS, a small AC voltage is applied to the SPE, sandwiched between two blocking electrodes, or the full cell battery over a defined range of frequencies, typically from 1MHz to 1Hz. An equivalent circuit is fitted to the resulting impedance data to determine the internal resistance of the battery.

Using the measured electrolyte resistance, circular sections of the polymer electrolyte films were cut for ionic conductivity measurements and mounted between two stainless steel blocking electrodes. The two-probe setup was placed in eight-channel coin/button cell testing board facilitate the connection to Metrohm Autolab. The ionic conductivity (σ) of the synthesized solid polymer electrolytes was determined from

$$\boldsymbol{\sigma} = \frac{\boldsymbol{l}}{\boldsymbol{R}\,\boldsymbol{A}}, \tag{1.3}$$

where **l, R**, and **A** represent the thickness, ionic resistance and surface area, respectively, of the electrolyte sample.

The transference number of an electrolyte is a dimensionless parameter that describes the total current carried by the respective ion across a given medium. Ideally, the

transference number of the electrolyte should be unity, inferring that all ions are carried across the electrolyte membrane. In addition to the ionic conductivity of solid-state electrolytes, the transference number is an important parameterin rechargeable LIB.

The transference numbers of the pure and nanocomposite polymer electrolyte are obtained by applying a small potentiostatic signal to a simple symmetrical cell, Li|Electrolyte|Li, for each type of electrolyte.

The first approximation is to assume that the electrolyte is comprised of dissociated salt (C^+ and A^-) .The lithium transference number tLi is calculated by taking the ratio of the steady-state current Iss (t= ∞) to the initial current I_0 (t=0) [50].

Cyclic voltammetry (CV) is a potentiodynamic electrochemical measurement where the working electrode potential is ramped linearly with time. The CV measurements were performed on the SPE using a Metrohm Autolab at RT. Full cell batteries were assembled with different types of electrolytes.

All batteries were charged and discharged under constant current (CC) conditions within a predefined operation voltage window and then subjected to multiple charge–discharge cycles. Their performances (capacity, energy density and power density) were measured using an Arbin BT2000.

1.5.2.3 Thermal Analysis and Characterization

Changes in physical and chemical properties of the SPE as a function of increasing temperature are measured (with constant heating rate) using thermogravimetric analysis (TGA) (TA instrument Model Q50). Also, flammability tests of both solid and liquid electrolytes were performed using a flame source. The solid electrolyte and liquid electrolyte were placed in the middle of a petri dish and heated directly with a lighter.

High Temperature Testing of LIB: All batteries were tested in a RH chamber (BTL 433), using the Arbin BT2000 with direct charge-discharge chronopotentiometry procedure and by applying a constant current rate with defined lower and higher cut-off voltage.

1.5.2.4 Mechanical Characterization and Testing

A Dynamic Mechanical Analysis (DMA) (Model Q800 from TA Instruments) was used for the mechanical characterization of different polymers. The samples were placed between a fixed and moveable clamp and a static tensile load was applied at room conditions. A precise control of the strain and stress determines critical mechanical properties of polymer such as the young's modulus, yield strength and % elongation.

A mechanical fatigue test of the LIB prototypes was conducted using a motorized mechanical testing stand (Mark-10-ESM301L).

1.6 Outline of the Dissertation

The main objective of this thesis work is to investigate new materials and designs to achieve enhanced properties, new mechanical features, and flexibility and stretchability in lithium ion batteries, without compromising the device electrochemical functionalities. Chapter 1 presents the motivation and objectives of this study. Relevant background is introduced including energy storage, lithium-ion battery, modeling and simulation. Chapter 2 proposes two types of solid polymer electrolytes for different applications (Fuel cell and Lithium-Ion Batteries). In this chapter, the mechanism of ionic conductivity enhancement by incorporating nano-particles filler to the Nafion matrix and polyethylene oxide (PEO)-based solid polymer electrolyte is discussed. Related research approaches and experimental results are discussed. Chapter 3 focuses on a novel flexible

Li ion battery based on a solid polymer nanocomposite electrolyte that exhibits a good average capacity and excellent cycling stability. Various factors are examined to evaluate the electrochemical and mechanical performances of the prototype including capacity fading, voltage retention and coulombic efficiency. Chapter 4 proposes a model for a stretchable LIB composed of solid-state materials arranged in a spiral shape under plastic sheet packaging. This new concept is promising to overcome the one-dimensional deformation issue while providing reasonable energy density and cyclic stability. Chapter 5 investigates the behavior of the solid polymer based batteries at elevated temperatures. In this chapter, the electrochemical performances of the battery are determined. In addition, a mathematical model is developed and the simulation results are validated with experimental data. Finally, Chapter 6 summarizes the research work and associated findings in this thesis. An outlook is also discussed pertaining to the specific limitations and further developments needed for potential future uses.

Chapter 2: Solid Polymer Nanocomposite Electrolytes

2.1 Introduction

Polymer electrolytes are an important class of electrolytes because their inherent safety compared to some classical electrolytes. High-molecular-weight polymers electrolytes are essentially nonflammable and nonvolatile, and they have the potential to be multifunctional.

In lithium-ion battery applications, organic electrolyte can lead to catastrophic failure, which often occurs due to the ignition of flammable organic solvent. Furthermore, polymer electrolytes are suitable for open systems such as fuel cells. Nafion, as an example, is the most commonly used polymer in fuel cell applications known for its excellent ionic conductivity, high water retention, and exceptional thermal and mechanical stability.

However, the room temperature ionic conductivity of polymer electrolytes is far lower than that desired for any practical energy storage application. For example, the ionic conductivity of lithium-ion battery polymer electrolytes ranges from 10^{-8} to 10^{-5} S/cm compared to that of liquid, which achieves ionic conductivities of 10^{-2} to 10^{-1} S/cm. In fuel cells, one method for improving the conductivity of polymer electrolytes is through the addition of nanofillers. The filler material type and dimensions should be carefully selected to form a stable system with the polymer matrix and other components of the electrolyte without adversely affecting other materials functional properties, such as the lithium salt in the case of LIBs.

In this chapter, two different types of solid polymer nanocomposite electrolytes are investigated for lithium-ion battery and fuel cell applications. The present work compares

the electrochemical properties of nanocomposite and pure polymer electrolytes and aims to provide a mechanistic explanation as to why the addition of nanofillers results in an apparent enhancement of these properties.

2.2 Polymer and Lithium Salt Selection

The current work is focused on poly (ethylene oxide) (PEO) based materials for their excellent salt-dissolving ability, availability at various molecular weights, compatibility with battery electrodes, and attractive mechanical properties. PEO has a glass transition temperature of -60°C and an ionic conductivity of 10^{-5} S/cm in temperatures ranging from 40 - 60°C [51]. Poly (ethylene oxide) was first suggested as a solid electrolyte material because of its aptitude to form coordination complexes with lithium salts [52-55]. This has opened up new perspectives on suitable electrolyte types and the lithium/PEO complexes could be deployed as solid electrolytes that can perfectly match the intercalation electrodes [56]. Conventional lithium salts combined with PEO containing Li^+ coordinating groups have the form of LiX, where X is preferably large anions such as perchlorate (ClO_4^-) or trifluoromethanesulfonyl imide ($(CF_3SO_2)_2N^-$). Many solid polymeric electrolytes with reported high ion conductivities contain Li-salt solvated in high molecular weight PEO and/or poly (propylene oxide) (PPO). These electrolytes are able to comply with shape changes making them ideal electrolyte candidates for flexible and stretchable batteries.

2.3 Ionic Conductivity

From a microscopic perspective, the ionic conductivity of a polymer electrolyte is dependent on the Nernst-Einstein relation between ion mobility diffusion as well as the Cohen-Turnbull model of the free volume theory. The ionic conductivity is defined as:

[57-59]

$$\sigma = \frac{nq^2}{k_B T} C_0 \exp\left(-\frac{\gamma v^*}{v_f}\right), \tag{2.1}$$

where **n** is the concentration of free ions involved in ionic transport, **q** is the charge carried by an ion, $\mathbf{k_B}$ is Boltzmann's constant , **T** is temperature, $\boldsymbol{C_o}$ is a pre-exponential constant that is related to gas kinetic velocities, **γ** is an overlap correction factor accounting for free volume being shared by neighboring molecules, **v*** is the minimum free volume needed to facilitate ion hopping, and $\mathbf{v_f}$ is the average free volume per molecule.

One accepted theory describing the lithium-ion transport mechanism in polymer electrolytes relies on ion hopping as a result of polymer chain segmental motion (**Figure 2.1.a**). It is generally perceived that within the PEO matrix the positively charged lithium-ions are coordinating with the negatively charged ether-oxygen molecules [60]. According to **Equation 2.1**, fast ionic transport is dependent on the free volume between molecules due to flexible polymer chains and the irregular chain packing within amorphous regions of the polymer structure.

PEO-based electrolytes are semi-crystalline materials with an approximate 60% crystallinity at room temperature while the remaining 40% of the polymer is in an amorphous elastomeric phase. This high degree of crystallinity, which adversely affects polymer chain motion, is responsible for the low ionic conductivity of SPEs. To remedy this, considerable effort has been made to synthesize PEO with a large and stable amorphous phase, that remains amorphous over a wide temperature range, in order to achieve faster ionic transport [38]. The most common approach to enhancing ionic conductivity is plasticization, which organic solvents or ionic liquids are added to the

SPE [61, 62]. Plasticized electrolytes have been reported to achieve ionic conductivities between 10^{-4} to 10^{-3} S/cm at room temperature. However, the addition of the plasticizer introduces a liquid phase into the SPE and substantially compromises the film's mechanical properties[63].

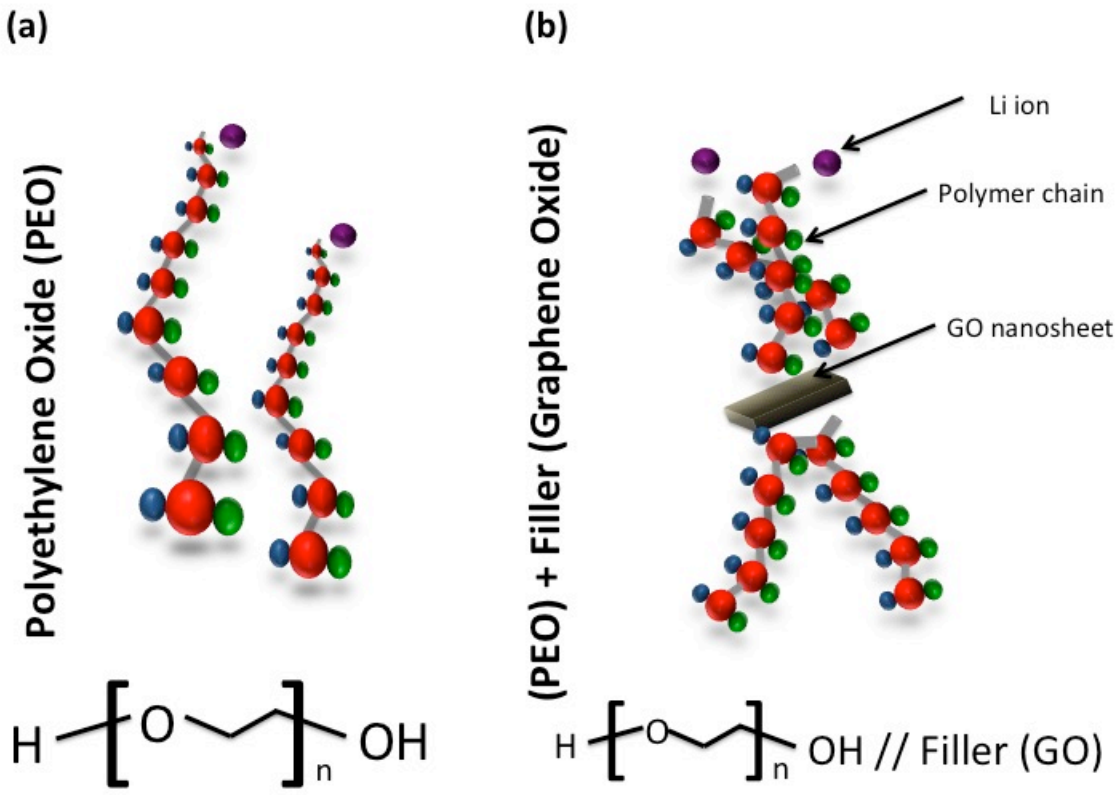

Figure 2-1: Schematic of the ionic conductivity mechanism within (a) Pure and, (b) Nanocomposite polymer electrolyte

2.4 Nano-sized Filler

In an effort to enhance the ionic conductivity without negatively affecting the mechanical stability of the polymer, researchers have developed solid polymer nanocomposite electrolytes, in which the chemically inert filler is introduced into the polymer matrix. Ceramic fillers including titanium dioxide (TiO_2), lithium aluminum

oxide ($LiAlO_2$), fumed silica (SiO_2), and aluminum oxide (Al_2O_3) [40, 64-67] have been shown to increase conductivity from 10^{-8} S/cm, for pure polymers, to 10^{-6} S/cm by reducing the degree of crystallinity of the polymer. Furthermore, composite electrolytes have been shown to demonstrate better electrochemical stability and the nanometer-scale additives may also enhance the mechanical strength and interfacial properties of the polymer electrolyte. However, the structure and the size of the additive caused undesirable effects such stiffness and aggregation. It is expected that smaller particles will improve the performance of the polymer electrolyte compared to larger size particles because they have high surface area. Nevertheless, the mechanisms in which these fillers actuate such improvements are not yet well understood and the attained ionic conductivity is still insufficient for high performance LIB applications.

2.5 Battery Application

Organic liquid electrolyte is the most commonly used battery electrolyte for its high ionic conductivity at room temperature. However, the poor thermal and chemical stability of the liquid electrolyte coupled with the risk for leakage of the flammable organic solvents exacerbates thermal runaway events, which result in catastrophic battery fires. This presents a significant safety concern associated with traditional liquid electrolytes. Conventional LIBs require a rigid and well-sealed container to prevent electrolyte leakage, thus limiting the mechanical flexibility and increasing the overall weight of the battery, but does not address the issue of material instability.

In response to growing safety concerns, dry solid electrolytes have gained notable consideration as liquid electrolyte replacements, specifically inorganic ceramic and solid polymers. Ceramic electrolytes are of particular interest for their high ion conductivities

and exceptional stability in hostile environments. Ion conduction in ceramics is based on the general diffusion mechanism by which ions move through vacancy and interstitial sites within the material. However, their inelastic behavior and high electrolyte-electrode interface impedance make ceramic electrolytes incompatible with the flexible and stretchable batteries. Solid polymers, on the other hand, are both stable and deformable, making them an ideal electrolyte material for flexible and stretchable battery applications. However, as previously discussed, scientists must overcome the low ion conductivity limitations of dry polymers to make them a feasible LIB electrolyte option for commercial applications.

2.6 Fuel Cell Application

Hydrogen fuel cells offer superior energy density and environmental-friendly solution to the global energy demands however there are still several issues that need to be addressed [68]. Among them are the transport properties of the proton exchange membrane (PEM) and specifically, the degradation of conductivity as a consequence of membrane dehydration. The most advanced proton exchange membrane fuel cell (PEMFC) technology is based on Nafion membrane that operates efficiently only under fully hydrated condition. This fluorinated sulfonic acid membrane was developed by DuPont Co. [69] Since PEMs are the key components in the operation in the fuel cell system, researchers have focused on developing a modified polymer with high proton conductivity, low electronic conductivity, good chemical and thermal stability, good mechanical properties and low cost. The modified Nafion composite membranes are a promising solution to meet the demanding performance of the PEMFC industry. Doping the pristine Nafion with different inorganic oxide fillers such as SiO_2, TiO_2, ZrO_2 [70-

78], shows enhancement in the proton conductivity and thermal and mechanical stability.

This chapter explores the use of nanofillers to improve polymer properties for battery or fuel cell applications, including a biomaterial-based nanofiller to accomplish the same goal. Activated carbon (AC) nanoparticles derived from coconut shells have the ability to absorb liquid and can be excellent candidates for hydrating the Nafion membrane. In addition, AC nanofiller can be obtained from renewable resources, which gives them sustainable and environmental friendly qualities.

2.7 Polyethylene Oxide-Graphene Oxide Nanocomposite Electrolyte for Lithium-Ion Battery

2.7.1 Overview

Many researchers have attempted to improve the properties of the polyethylene oxide by adding different types of ceramic fillers [40]. This study investigated a solid polymer with enhanced properties such as high ionic conductivity and improved transference number induced by the network of dispersed nanofillers.

This section focuses on the properties of PEO based solid polymer electrolytes modified with nano sized Graphene Oxide (GO) fillers (**Figure 2.1.b**). Our research group has reported previously the successful use of the (GO), demonstrating an increase in both ionic conductivity and mechanical stability of PEO [79]. Other studies have investigated the incorporation of GO sheets into the PEO host and showed a good agreement with our findings [80-82]. The choice of the $LiClO_4$ salt, the EO:Li (16:1) molar ratio, and the ideal amount of filler were carefully evaluated in a previous work [79] in order to meet the electrochemical and mechanical requirements for the SPE

synthesis. The calculations of EO:Li molar ratio and the filler content are presented in **Appendix A**.

2.7.2 Experimental

2.7.2.1 Polymer Electrolyte Film Preparation

100,000 Mw PEO, with chemical formula $C_{2n} + 2H_{4n} + 6O_n + 1$, and $LiClO_4$ salt (99.99%) were purchased from Sigma Aldrich. The solid polymer electrolyte was prepared by mixing 2 g of PEO and 0.3 g of Li salt in a 4 oz. jar half filled with the solvent, acetonitrile (C_2H_3N). The electrolyte solution was sonicated (Branson 3510 Sonicator) for 30 minutes and then solution cast into a Teflon petri dish (area = 76.9 cm^2) where it dried at room temperature for ~24 h. The resulting free standing solid electrolyte films had a thickness of ~200 μm. To ensure the removal of the solvent, the membranes were vacuum dried at 50 °C for an additional 24 hours and stored in the glove box, under constant Argon flow (H_2O < 0.5 ppm), prior to testing.

The nanocomposite polymer electrolyte fabrication process is similar to that of the pure polymer films, except that a 1 wt% of GO (Graphene Supermarket) content was added to the solution. GO is electrically insulating, thus eliminating the risk of any possible short circuit in the battery. GO also has excellent mechanical properties and enhances the overall mechanical strength of the polymer. The nanoscale GO powder was synthesized using the Hummer's method (**Appendix A**).

2.7.2.2 Morphological Characterization of the SPEs

Polarized light microscopy (PLM), carried out with an Advanced EPI Trinocular Infinity Polarizing Microscope (50X- 1600X-), was used to investigate the morphology and the crystallinity of the PEO films. The structure of GO filler was observed using the

Scanning electron microscopy (SEM), utilizing a Zeiss Model: Leo 1525 Gemini.

2.7.2.3 Electrochemical Window of the Polymer Electrolyte

The electrochemical stability window of the polymer electrolyte was obtained by a linear voltammetry sweep [83]. Full cell LIBs, containing graphite, $LiCoO_2$, and either the pure or nanocomposite polymer electrolytes, were charged at a scan rate of 25 mV/s, and data was collected using an Autolab Potentiostat.

2.7.2.4 Thermal Characterization

Thermogravimetric analysis (TGA) data of the polymer nanocomposite electrolyte was collected using a TA instrument Model Q50 TGA. The polymer was heated at 20°C/min from room temperature to 500°C in a nitrogen atmosphere. Flammability tests of both solid and liquid electrolytes (nanocomposite PEO and commercial electrolyte $LiPF_6$-EC/DEC, respectively), were also performed by heating the electrolyte materials directly with a lighter.

2.7.2.5 Ion conductivity and Transference Number Characterization

The ion conductivities of the pure and nanocomposite PEO electrolyte films were determined using electrochemical impedance spectroscopy method carried out by a Metrohm Autolab Potentiostat. The samples were sandwiched between two stainless steel electrode discs and the complex impedance spectra was obtained in the frequency range of 1 Hz to 1 MHz using the frequency response analysis (FRA) module of the Autolab.

In addition to ion conductivity, the transference numbers of the solid nanocomposite and pure polymer electrolytes were also determined to provide further insights into the effects of GO fillers of electrochemical performance. The transference numbers of the

pure and nanocomposite polymer electrolytes were obtained by applying a small potentiostatic signal (10mV) to a symmetrical Li|Electrolyte|Li cell. The lithium transference number t_{Li} is calculated by taking the ratio of the steady-state current I_{ss} to the initial current I_0 [50].

2.7.3 Results and Discussion

Adding a low content of GO can disrupt the ordered packing of semi-crystalline PEO chains and reduce the polymer crystallinity. This is verified using polarization light microscopy (PLM) of the pure PEO and PEO/1 wt% GO, depicted in **Figure 2.2. a-d**, where the addition of 1 wt% GO is shown to increase the amorphous regions of the PEO. The SEM images present the shape and size of the GO layers in **Figure 2.2.e** and the morphology of the PEO/GO composite electrolyte polymer in **Figure 2.2.f**. The two dimensional, GO sheets with their ultra-large surface area make them promising candidates for improving the ionic conductivity of the electrolyte by decreasing the crystanillity of the polymer.

Conversely, nanofiller aggregation can adversely affect ionic transport by reducing the available free volume necessary for ion hopping. In particular, GO has a tendency to aggregate because of its high surface area and this is exacerbated with an increasing filler content. To reduce this adverse effect, a very low concentration of nanofiller was used for the fabrication of the polymer electrolyte.

Yuan et al., determined that a 1 wt% of GO can facilitate salt dissociation by calculating the fraction of free $ClO4^{-1}$ from the Fourier transform infrared (FTIR) spectra for pure and nanocomposite PEO with various GO contents, seen in **Figure 2. 3a**. Moreover, **Figure 2. 3b** shows that the addition of a small amount of filler enhances the

thermodynamic properties of the polymer [79].

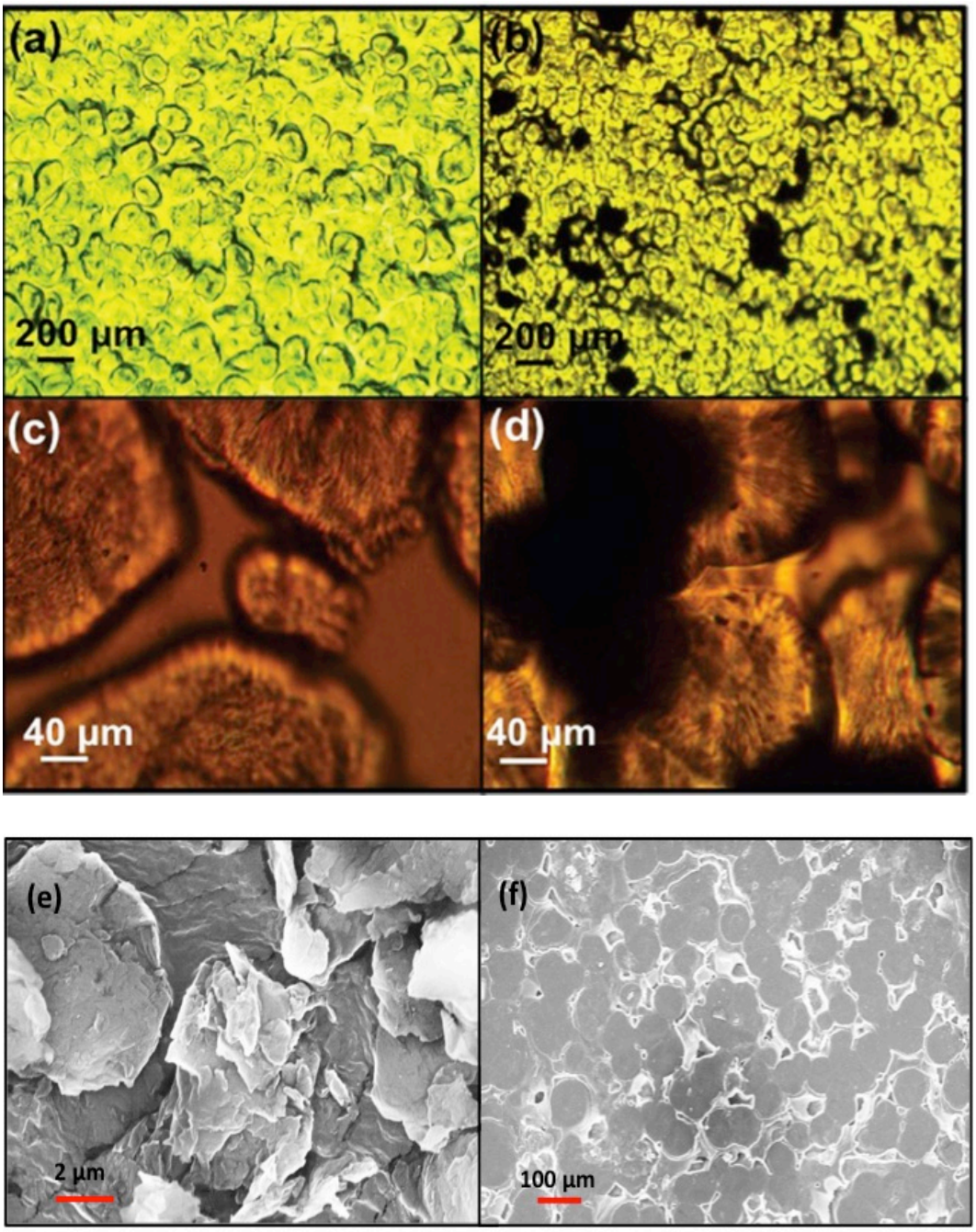

Figure 2-2: Polarization light microscopy (PLM) of (a), (c) pure PEO and (b), (d) PEO/1 wt% GO. Scanning electron microscopy images of (e) GO powder and (f) PEO/1 wt% GO.

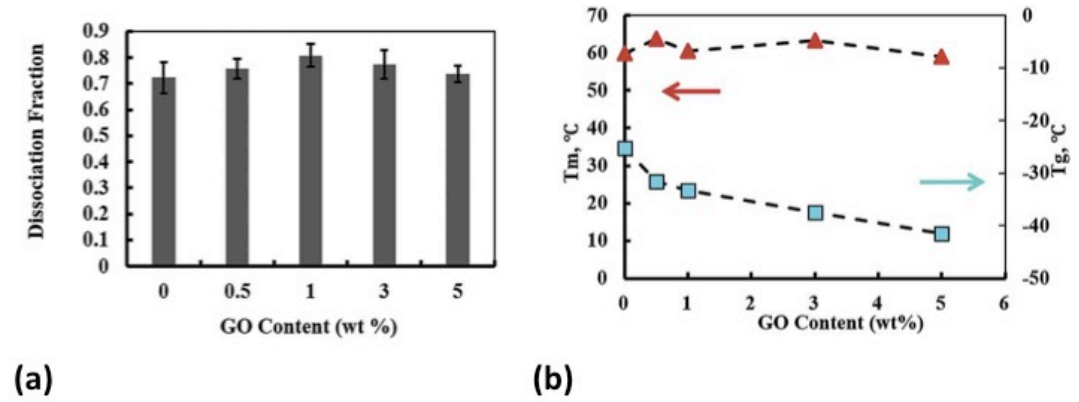

Figure 2-3: (a) Li salt dissociation fractions of polymer electrolyte films (b) Melting point (Tm) and glass transition temperature (Tg) [79].

Thermogravimetric analysis and flammability tests were performed to compare the thermal stability of the nanocomposite PEO (PEO/GO/$LiClO_4$) electrolyte and conventional liquid electrolyte. The TGA curve in **Figure 2.4a** demonstrates that PEO/GO/$LiClO_4$ is thermally stable up to 350 °C. At approximately 350°C to 370°C, the PEO/GO/$LiClO_4$ film undergoes a significant weight loss due to polymer decomposition. Furthermore, ignition of the organic liquid (**Figures 2.4b-2.4d)** and solid PEO/GO/$LiClO_4$ electrolytes (**Figure 2.4f-2.4h**) was attempted by bringing a flame to the electrolyte materials. **Figure 2.4e** displays the captured image of the free standing and mechanically stable solid PEO/GO/$LiClO_4$ film. After 30 seconds of ignition with a flame source, the solid PEO/GO/$LiClO_4$ electrolyte did not show any combustion, revealing its nonflammable nature. However, the commercial electrolyte (LiPF6-EC/DEC, 1:1 in volume) was highly flammable and easily ignited once in contact with the flame.

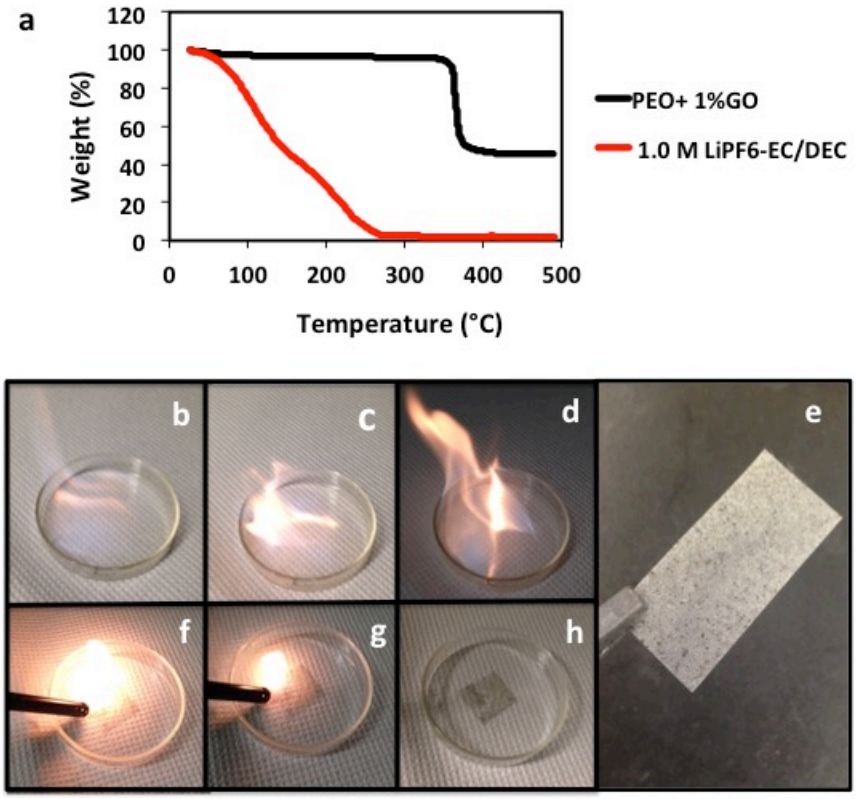

Figure 2-4: (a) Thermogram comparison of solid PEO/1%GO and organic liquid electrolyte, (b)-(d) liquid electrolyte flammability test, (e) image of the PEO/1 wt%GO film, and (f)-(h) solid PEO/1 wt%GO flammability test.

Figure 2. 5 compares the electrochemical stability window of full cell batteries made with conventional liquid (LiPF6) electrolyte (blue), nanocomposite PEO electrolyte + 5 wt% LiPF6 (red), pure PEO electrolyte + 5 w% LiPF6 (green), nanocomposite PEO (purple), or pure PEO electrolyte (orange). The irreversible onset of the current determines the electrolyte's breakdown voltage. In the case of the conventional LIB, using a liquid electrolyte (LiPF6 with a 1:1 vol of EC+DEC), the electrochemical stability window only extends to 4V. The battery cells with the prepared SPNE show a wider electrochemical window, exceeding 5V, than those with the pure polymer electrolyte. This demonstrates that the composite electrolyte has a stable electrochemical

window that extends the overall operating voltage of the cell, which is 4.2V.

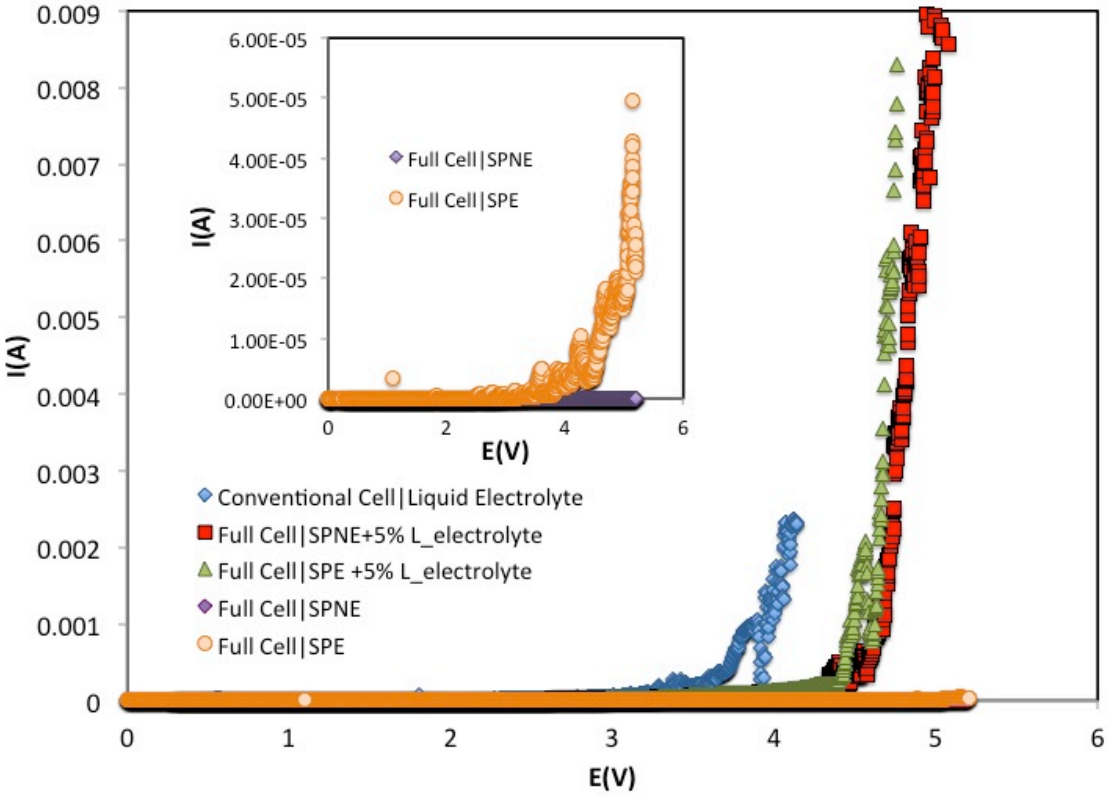

Figure 2-5: Current–voltage response of full cell batteries made with different type of electrolytes obtained at room temperature.

Figure 2.6 compares the impedance spectroscopy of battery cells with pure and nanocomposite PEO electrolyte. The details of the ionic conductivity calculation are presented in **Appendix A**. The nanocomposite electrolyte shows a near one order of magnitude enhancement in ion conductivity (10^{-7} S/cm) compared to that of pure polymer electrolyte (10^{-8} S/cm). This ion conductivity improvement can be attributed to the two dimensional, single-atomic-thickness structure, and ultra-large surface area of GO nanoparticles, which reduces the crystallinity and increases polymer chain mobility. Furthermore, potential formation of GO ion transport channels and increase in salt

dissociation can lead to fast ionic transport within the SPNE compared to the pure polymer electrolyte.

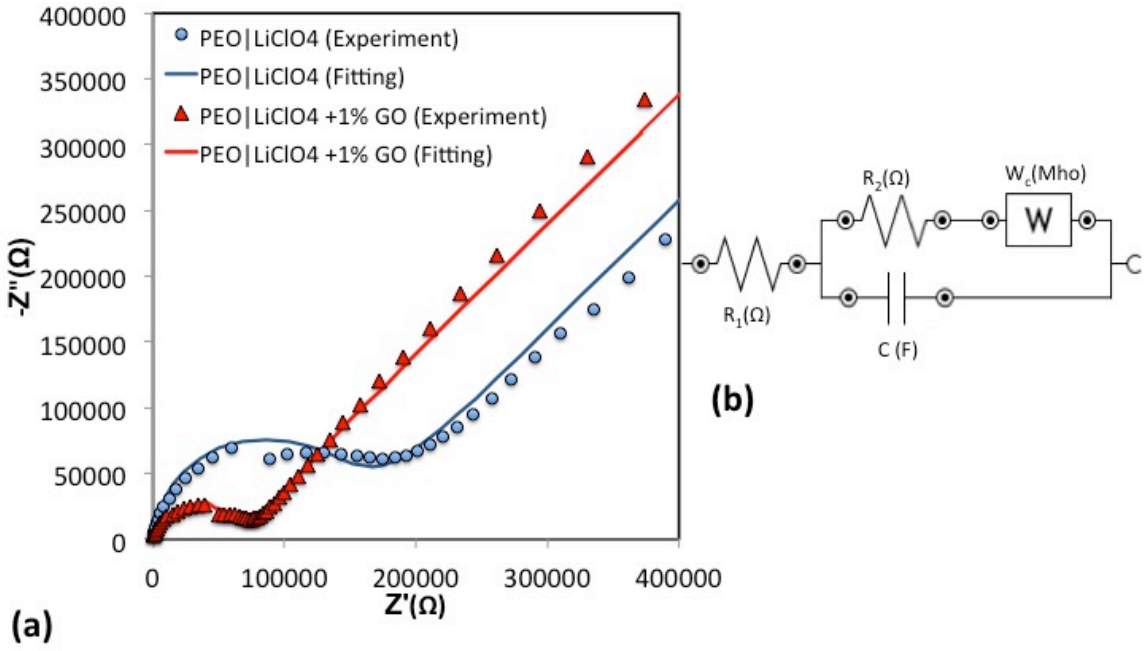

Figure 2-6: (a)A.C. impedance spectra of PEO|LiClO4 and PEO|LiClO4 +1 wt%GO electrolytes (b) Fitting circuit.

The transference number of the electrolyte is also an important criteria to consider when choosing LIB polymer electrolyte materials. Chrono potentiometry was used to determine the transference numbers of the pure and nanocomposite PEO electrolytes, seen in **Figure 2.7**. The results calculated transference numbers in addition to the ionic conductivities of the pure and nanocomposite PEO electrolytes are summarized in **Table 2. 1.** The PEO/GO polymer electrolyte shows a higher transference number compared to the pure PEO electrolyte. The calculated transference number of the pure PEO with LiClO4 salt is in agreement with values previously reported [11, 84].

Table 2-1. The transference numbers of the PEO| LiClO4 and PEO| LiClO4+ 1 wt%GO

Electrolyte	I_0 (A)	I_{ss} (A)	t_{Li}
PEO | $LiClO_4$ +1 wt%GO	7.14×10^{-7}	1.87×10^{-7}	0.262
PEO | $LiClO_4$	7.41×10^{-6}	1.41×10^{-6}	0.190

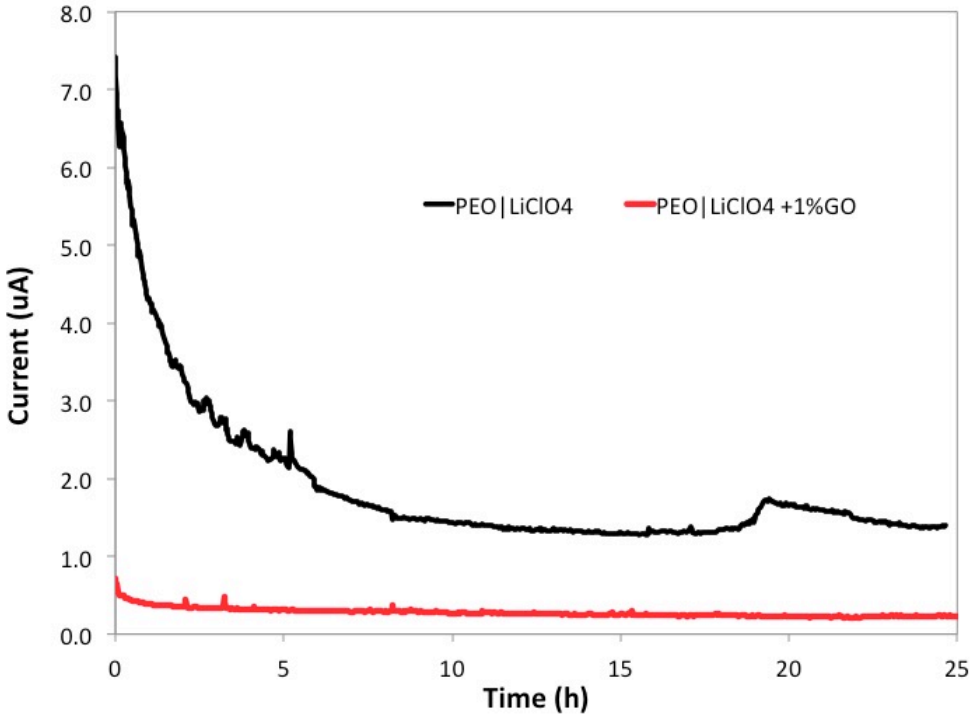

Figure 2-7: DC polarization of the symmetric cell based on the PEO| LiClO4 and PEO| LiClO4 +1 wt%GO.

2.7.4 Conclusions

In summary, novel solid polymer nanocomposite electrolyte with graphene oxide nanosheets was fabricated using an evaporation casting method and the effects of the nanofiller on the electrochemical properties of PEO-based electrolytes was investigated. The comparison between the pure and nanocomposite polymers shows that a 1 wt% GO content significantly enhances the ion conductivity of the pure PEO electrolyte by more than one order of magnitude. Furthermore, GO nanosheets improve the transference number, confirming enhanced ion transport, and widen the electrochemical voltage

window, suggesting enhanced safety during operation. The noteworthy electrochemical enhancements of SPE materials due to the addition of fillers, is the key factor for safer LIBs, especially for special applications like flexible and stretchable batteries.

2.8 Nafion Membrane with Coconut Shell Nanofillers for Hydrogen Fuel Cell

2.8.1 Overview

Proton exchange membrane fuel cells (PEMFCs) have captured worldwide attention due to their high energy density, renewability, and environmental friendliness. [78, 85-89] One of the key aspects in PEMFCs is the ion conductivity in the proton exchange membrane (PEM). The proton exchange membrane must facilitate fast proton (H^+) transport, insulate electron conduction, and exhibit adequate thermal and mechanical stability among others [69]. A widely used PEM material is the sulfonated tetrafluoroethylene-based fluoropolymer–copolymer known as Nafion® developed by DuPont in the 1960s [78]. The Nafion® molecule is comprised of a hydrophilic sulfunate head and a hydrophobic Teflon-based backbone or tail as shown in **Figure 2. 8** [69, 90]The hydrophilic sulfunates cluster and align together to form pores and nanochannels that allow fast proton transport while the hydrophobic backbones provide mechanical support and stability [69, 90, 91].

Many studies have shown that the Nafion membrane must be fully hydrated for high proton conductivity [70, 92-96]. This presents a challenge especially at higher operating temperatures of the PEM fuel cells where the environment can become dry [87, 97]. Humidification systems are often utilized to keep the membrane hydrated at all times

leading to additional cost, weight, and volume of the fuel cells [98, 99]. Several studies have demonstrated that nano-sized fillers including metal oxides (i.e., SiO_2, TiO_2, ZrO_2) [70-78], carbon nanotubes [87, 99-101], and activated carbon [91] can assist in the hydration and "self humidification" of the Nafion. Here we investigate the Nafion membrane filled with coconut shell activated carbon (AC) nanoparticles and show that enhanced water sorption and ion conductivity can be achieved with very small percentage of fillers (0.7 wt.%) without a significant compromise in the mechanical properties.

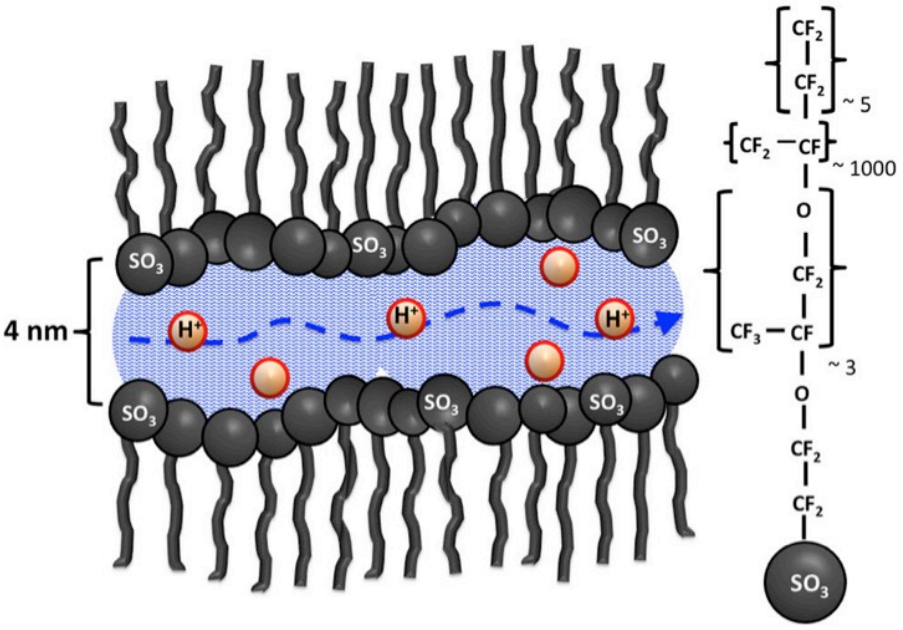

Figure 2-8: The chemical structure of PFSA Nafion membrane and a depiction of nanochannel[102].

Several models of ion conductivity for pure Nafion membranes have been proposed in the past [103-107]; however, modeling of polymer composite proton conductivity remains open. Here, we propose a semi-empirical model of ion conductivity for a Nafion/AC composite and elucidate the general effects of filler particles on both enhancement and degradation of PEM conductivity.

Coconut shells are typically made into charcoal by burning at a temperature between 500 and 900 °F. They are activated (made porous) using steam in a kiln or furnace [108, 109].

Activated carbon nanoparticles derived from coconut shells have the ability to absorb liquid like a "molecular sponge" [91, 110] and can be excellent candidates for self-hydration of the Nafion membrane. The water extraction from the Nafion membrane occurs via capillary action. In addition to availability and bio-friendliness, no pretreatment may be required to process the raw coconut shell material and the granular coconut-based carbon shows the least rate of physical degradation. Also, coconut based ACs have a predominance of pores that can account for 95% of their available internal surface area making them ideal for adsorption of small molecular weight species [98]. The specific surface area (SSA) of ACs has been reported to be greater than 1300 m^2/g [111]. Our experimental investigations show that very small content of coconut-based AC nanoparticles can increase water sorption to 70 wt.%, demonstrating 84 % enhancement compared to that of pure Nafion and improve ion conductivity by about an order of magnitude.

2.8.2 Materials and Methods

Nafion was purchased from Ionic Liquid, Inc. (LQ-1105— 1100 EW) as a 5 wt.% solution in a mixture of alcohol and water. The coconut-shell-based activated carbon was purchased from US Research Nanomaterials, Inc (**Appendix A**). All chemical products were used without further purification. Deionized (DI) water was used throughout the membrane fabrication process. The pure and nanocomposite films were fabricated by evaporation casting technique [94, 112-118]. Five volumes of the Nafion solution, five

volumes of denatured ethanol [ethanol/DI water mixture (4:1 wt. ratio)] and three volumes of dimethyl formamide (DMF) (25:25:15 ml) were combined in a 4 oz. jar.

As-received coconut-based activated carbon (AC) powder was further ground using a mortar and pestle. The AC powder was then dried in the oven at 80 °C for 24 h and stored at high temperature after sonication for 30 min in a Branson 3510 sonicator. The weight of the AC filler was measured according to the desired percentage of the composite membrane (**Appendix A**). The fine powder was incorporated into the liquid solution through 24 h of stirring followed by 30 min of sonication. The polymer–composite solution was then poured into a Teflon petri dish (area=76.9 cm^2) and placed in an oven at 80 °C under vacuum for 24 h. Following casting, the membranes were pre-treated as follows: The membrane was boiled in 5 wt.% hydrogen peroxide (H_2O_2) at 85 °C for 1 h and then rinsed with distilled water for 15min.

Then, it was placed in 0.5M sulfuric acid (H_2SO_4) at 85 °C for 1 h. The membrane was then rinsed with the DI water until the acidity level dropped to neutral level using a pH meter. Next, the membrane was boiled in DI water at 85 °C for 2 h to ensure high water sorption. The coated membrane was stored in doubly DI water at room temperature (RT) for at least 24 h prior to testing.

For ionic characterization, the membranes were cut into discs of 15 mm and 19 mm diameter. The thickness of each disc was measured using a Mitutoyo micrometer with a resolution of 1 μm and the thickness ranged from 40 to 99 μm.

The samples were removed from DI water and gently wiped with an absorbent paper to remove liquid water from the surfaces. The samples were sandwiched between two stainless steel cylindrical blocking electrodes (area=2.84 cm^2) with identical diameters.

An eight-channel coin/button cell testing board was used to facilitate the connection between the Autolab and the two-probe setup. At least three samples were tested for each membrane and each measurement was repeated three times to ascertain reproducibility and statistical confidence.

For high temperature measurement, the eight-channel coin/button cell testing board was placed inside an oven with controlled RH (50 %) and temperature (70 °C). Complex impedance spectra were obtained using Metrohm Autolab Frequency Response Analysis (FRA 2) with frequency range capability from 10 μHz to 1MHz. The voltage amplitude was set at 10 mV. The impedance measurements were fitted to a constant phase element or imperfect capacitor (**Q**) in series with an ideal capacitor (**C**) and total membrane resistance (**R**) in parallel. The typical fitted values of the circuit elements and the average proton conductivities of pure and composite membranes are listed in **Tables 2.2** and **2.3**, at room temperature and 70 °C, respectively.

Table 2-2. Proton conductivities of pure and composite membranes at room temperature

Membrane	**Circuit components**						σ_{avg}
Wt .%	**Q [S]**	**N**	**C [F]**	**R [Ohm]**	**Thickness [mm]**	**Area [mm^2]**	**[mS cm^{-1}]**
Pure	2.02 x10^{-5}	0.8174	2.20 x10^{-7}	9.261	0.079	176.62	0.493
0.5	4.10 x10^{-5}	0.8369	6.05 x10^{-6}	1.419	0.050	176.62	2.000
0.7	1.01 x10^{-3}	0.8281	3.60 x10^{-3}	0.592	0.060	176.62	3.491
1	2.39 x10^{-5}	0.8401	9.00 x10^{-13}	2.613	0.084	176.62	1.909
2	8.31 x10^{-6}	0.7470	9.00 x10^{-7}	3.531	0.084	176.62	1.412
3	3.24 x10^{-5}	0.8047	5.03 x10^{-7}	5.086	0.069	176.62	0.762
5	2.67 x10^{-5}	0.5737	6.36 x10^{-7}	6.314	0.081	283.38	0.458

For morphological characterization, a scanning electron microscope was used with SEM Zeiss Model: Leo 1525 Gemini. For mechanical testing, Nafion membrane samples

were immersed in DI water for 24 h and were tested using the Dynamic Mechanical Analysis (DMA) Model Q800 from TA Instruments, at room temperature and 50 % relative humidity (RH).

Table 2-3. Proton conductivities of pure and composite membranes at 70°C

Membrane Wt .%	Circuit components				Thickness [mm]	Area [mm^2]	σ_{avg} [mS cm^{-1}]
	Q [S]	N	C [F]	R [Ohm]			
Pure	2.37×10^{-4}	0.7524	9.00×10^{-13}	2.6848	0.084	176.62	1.760
0.5	1.38×10^{-4}	0.7697	9.00×10^{-13}	1.0986	0.063	176.62	3.290
0.7	1.10×10^{-4}	0.8071	9.00×10^{-13}	0.9257	0.081	176.62	4.845
1	3.98×10^{-5}	0.8458	9.00×10^{-13}	1.0488	0.084	176.62	3.706
2	7.20×10^{-5}	0.8410	1.17×10^{-5}	1.2595	0.063	176.62	2.729
3	7.08×10^{-6}	0.8696	9.00×10^{-13}	3.3349	0.098	176.62	1.744
5	4.28×10^{-6}	0.7328	9.00×10^{-13}	4.9720	0.077	176.62	0.867

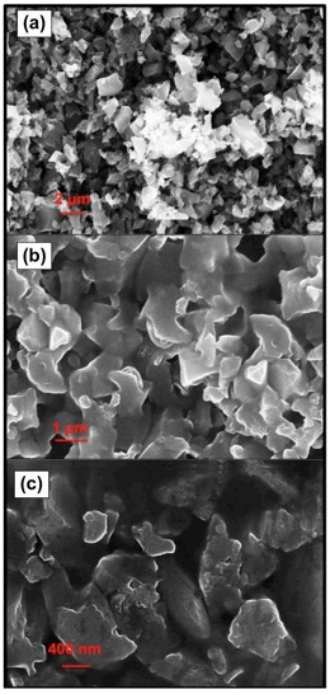

Figure 2-9: Scanning electron microscopy (SEM) image of (a) coconut shell activated carbon (AC) powder, (b) Nafion nanocomposite with 15 wt%

AC, and (c) with 0.5 wt% AC [102].

2.8.3 Results and Discussion

Figure 2.9a shows the SEM images of the coconut-shell-based activated carbon particles used in our study. **Figure 2.9b** and **c** show the Nafion/AC nanocomposites at different contents and magnifications. The particle average size is about 500 nm. The size and number of pores can influence the activated carbon water sorption capacity. The SEM images show uniform dispersion of the AC nanoparticles in the Nafion matrix. A good affinity between the matrix and filler appears to be present. Since the AC nanoparticle is electrically conductive [107] and higher contents can form physical networks, we focused on lower AC filler contents.

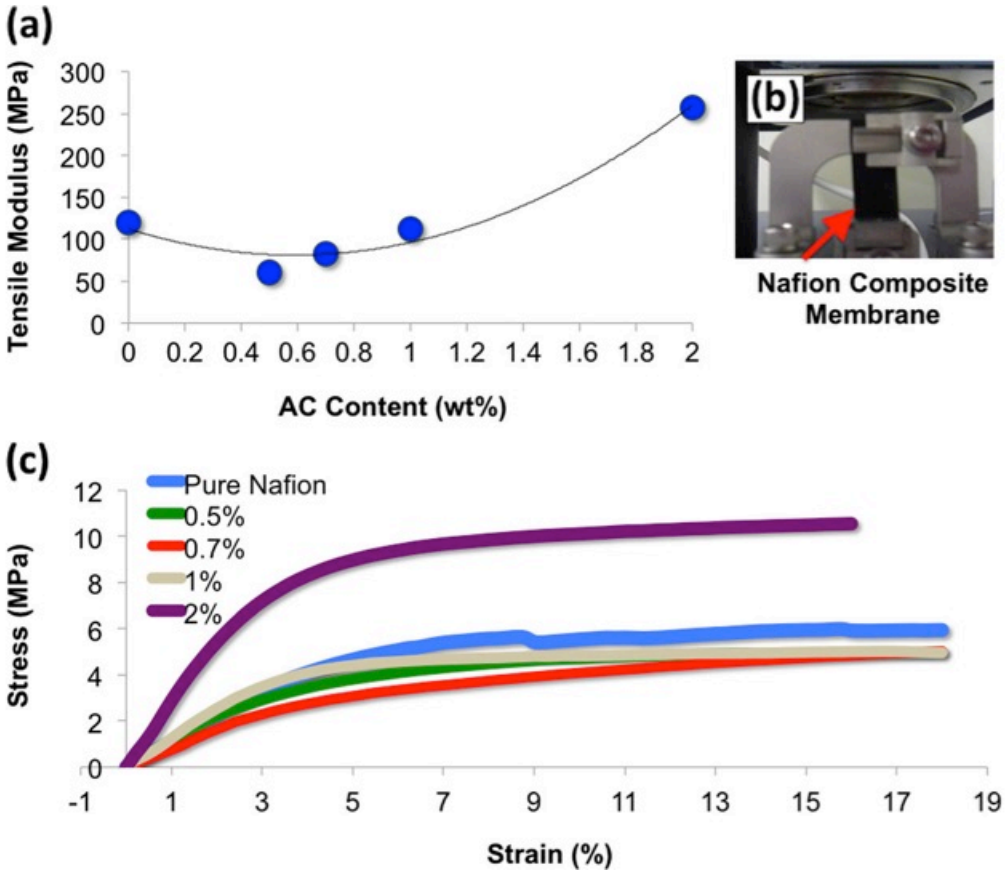

Figure 2-10: Mechanical properties of pure and composite Nafion membranes at

room temperature and 50 % RH: (a) tensile modulus, (b) Nafion/AC membrane under DMA tensile testing, and (c) stress– strain curves.

Figure 2.10 shows the mechanical properties of the Nafion nanocomposite. The mechanical properties of the pure Nafion and Nafion/AC nanocomposites are highly influenced by temperature, humidity, water content, polymer structure, molecular weight, chain branching, degree of cross-linking, chain orientation, crystal structure, and extent of crystallization [117].

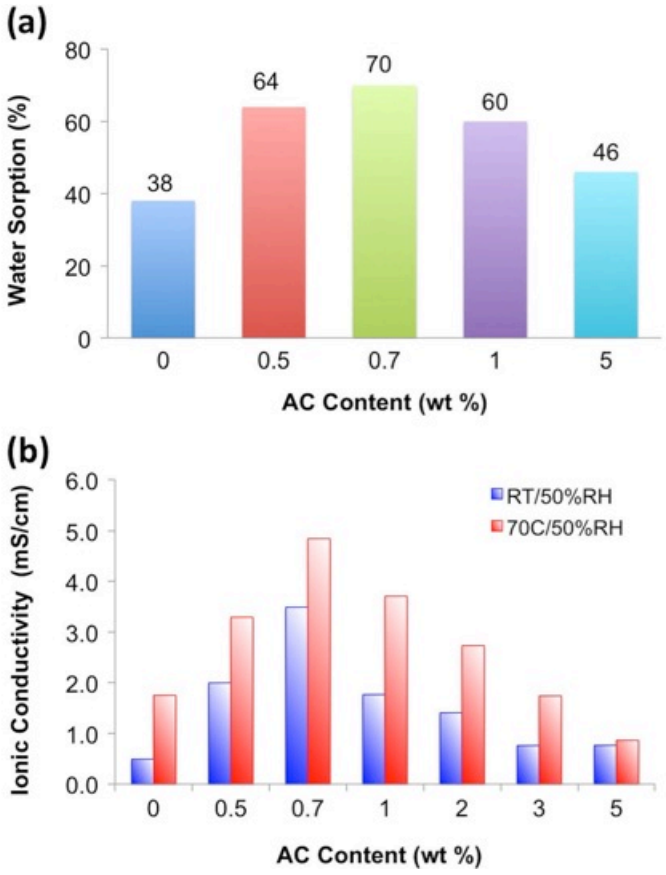

Figure 2-11: (a) Water sorption and (b) ion conductivity of pure and composite membranes [102].

Specifically, the elastic and plastic deformations of Nafion based materials can change with both the temperature and water content among others [118-120]. We tested

all the samples at the same conditions to isolate the effects of AC nanofillers.

We observe that the tensile modulus of the membrane initially declines upon the addition of AC fillers (0.5 %), but subsequently rises at higher AC contents. Furthermore, we observe that the composite membranes seem to exhibit less elongation than the pure Nafion especially at 2 wt.%. An optimum state of mechanical properties appears to be realized at about 0.7 to 1 wt.% where Young's modulus and percent elongation are relatively conserved. Poor interfacial bonding between AC filler and Nafion matrix can contribute to the internal stresses inside the structure, which may subsequently degrade the flexural properties of the Nafion/AC nanocomposite. Such changes in the bulk composite properties are more pronounced at higher AC contents where particle aggregation and inhomogeneity can occur. **Figure 2.11a** shows the effect of the AC particles on the water uptake of Nafion membrane. The water uptake of the membrane immersed in DI water was calculated as shown in **Equation. 2.2**:

$$\textbf{Water uptake } \% = \frac{W_{wet} - W_{dry}}{W_{dry}} \times 100 \, . \qquad (2.2)$$

The water uptake of the pure casted Nafion immersed in DI water at room temperature was measured to be about 38 wt.%. At 0.7 wt.% AC filler content, the water uptake of the composite membrane is substantially enhanced to 70 wt.%. The large increase of 32 wt.% in water uptake of composite membrane is attributed to two main enhancement effects: (a) the "connection" and "bridging" of isolated inactive Nafion pores by AC fillers and the "activation" of such pores in water sorption process and (b) direct increase in water adsorption of micro-/mesoporous AC/Nafion hybrid membrane compared to the pristine Nafion films. The effective "activation" of isolated inactive Nafion pores is postulated to be the main positive trigger mechanism for water sorption

increase. Since there are a finite and limited number of isolated pores in the Nafion membrane, the percentage of AC fillers required to "activate" such pores can be very low, and the experimental value of 0.7 wt.% AC content at maximum water uptake appears to fit this theory. The molecular simulation study of the hydrophilic and hydrophobic behavior of activated carbon surfaces by Müller and Gubbins [121] provides insights on the adsorption mechanism of activated carbon particles. The study suggests that water adsorption by AC particle occurs through the formation of three dimensional clusters centered on the active oxygenated sites on the AC pore surfaces. The activation of carbon essentially leads to the creation of these active sites on the pore surfaces and the subsequent transition from hydrophobic to hydrophilic carbon. Furthermore, the relative location of the active sites on the AC pore surfaces and the cooperative "bridging" between the sites associated with the pore size and site distribution can greatly affect the amount of water adsorbed.

At higher contents of AC fillers (>0.7 %), the water uptake declines which suggests that the adverse effects of AC filler are dominating. The decrease in water uptake can be attributed to (a) the aggregation of AC particles and the subsequent loss of specific surface area leading to the reduction of water adsorption capability, and (b) the physical constriction and stiffening of the Nafion nanochannels by AC particles and the subsequent reduction in channel water sorption and swelling.

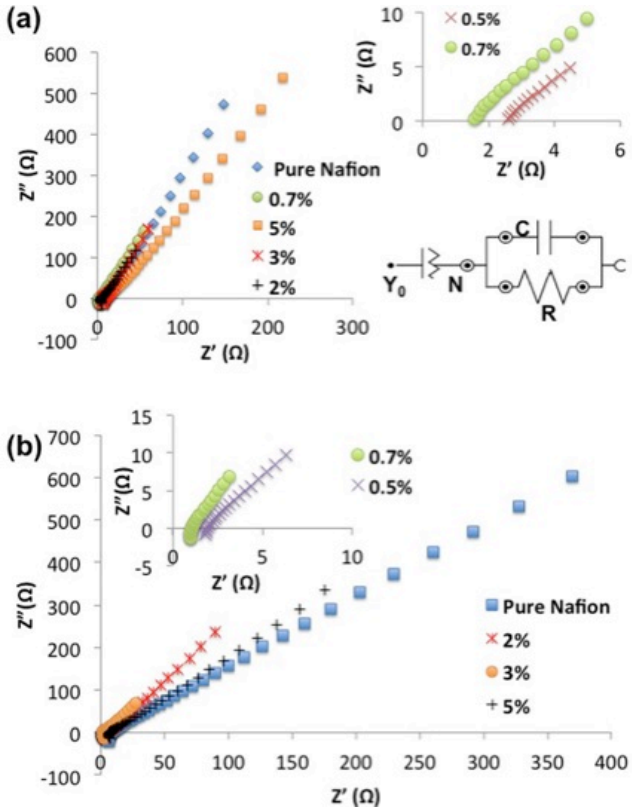

Figure 2-12: Nyquist plot for different contents of AC (0.5 and 0.7 wt.%, top inset) with the equivalent model circuit at (a) room temperature and (b) 70 °C [102].

Based on the comparison of selective studies presented in **Table 2.4**, the ionic conductivity of the Nafion membrane can vary widely from 10^{-5} to 0.1 S/cm and the water uptake can range from 20 to 140 % attributed to various factors, namely, the fabrication and pretreatment procedure of the membrane, morphological and dimensional properties, composition (filler, solvent, etc.), testing conditions (temperature, humidity, and water activity), and the measurement method.

Table 2-4. Comparison of selective studies on ion conductivity and water uptake of proton exchange membranes

Reference	Membrane/ Filler	Fabrication procedure	Solvent	Membranes Thick. (mm)	Conductivity (S cm^{-1}) at $25^{o}C$ /100 RH	Water content (wt%)
N.P Cele et al.[87]	Nafion	Solution casting	NA	0.2	$2.04*10^{-4}$	22
	Composite Nafion/(CNTs)		NA	0.15 - 0.3	$3.02*10^{-5}$-$2.45*10^{-4}$	6.5-9.5
T. Sakai et al.[122]	Nafion 117	Commercial	NA	0.22	NA	36
F.N. Buchi and G.G. Scherer [123]	Nafion 112	Commercial	NA	0.058-0.062	NA	34-36
	Nafion 115		NA	0.145-0.150	NA	34-36
	Nafion 117		NA	0.200-0.205	NA	34-38
S.J. Peighambardoust et al.[68]	Recasted Nafion	Recasted(fully hydrated state)	NA	0.12	0.018	50
	Nafion/Laponite (90/10,w/w)		NA	0.14	0.022	87
	Nafion/Grafted Laponite (90/10,w/w)		NA	0.14	0.03	70
C.H. Ma et al.[118]	Nafion	Solution casting	DMAc	0.172	$4.34*10^{-3}$	15.3
	Nafion		DMF	0.173	$1.81*10^{-3}$	15
	Nafion		NMF	0.171	$1.36*10^{-3}$	14.26
	Nafion		MeOH-H2O	0.174	$17.6*10^{-3}$	34.1
	Nafion		EtOH-H2O	0.175	$8.11*10^{-3}$	32.32
	Nafion		IPA-H2O	0.174	$7.01*10^{-3}$	32.71
H.L. Lin et al.[124]	Nafion-117	Commercial	NA	0.175	0.034 +/- 0.003	22.1 +/-1.1
	Nafion	Solution casting	DMAc	0.168	0.039 +/- 0.004	22.3 +/-1.3
H.C. Chien et al.[91]	Nafion 211 Pristine	Catalyst-coated membrane	H2O	0.025	0.00017 (50% RH)	35
	Composite Nafion/5%AC		H2O	NA	0.0013(50% RH)	80
	Composite Nafion/10%AC		H2O	NA	0.01 (50% RH)	140
N. Miyake et al.[125]	Nafion	Solution casting	MeOH-H2O	NA	0.11	32.4
	Composite Nafion/4-5 wt% Silica		MeOH-H2O	NA	0.13	38.9
	Composite Nafion/16-17 wt% Silica		MeOH-H2O	NA	0.079	35
	Composite Nafion/21-26 wt% Silica		MeOH-H2O	NA	0.069	34.4
R.F. Silva et al.[116]	Nafion 112	Commercial	NA	0.055	25	37
	Nafion 115	Commercial	NA	0.149	39	37
	Nafion	Solution-cast membrane	DMF	0.096	28	45
Y.F. Zhang et al.[71]	Nafion117	Commercial	NA	0.19	0.022(80C,10-70%RH)	27.97
	SPFEK	Solution-cast membrane	DMSO	0.19	0.023(80C,10-70%RH)	30.15
	SPFEK/SiO_2			0.19	0.023(80C,10-70%RH)	39.84
	SPFEK/SiO_2–HPMC			0.19	0.025(80C,10-70%RH)	48.51
Y. Zhai et al.[126]	Recast Nafion	Solution-cast membrane	DMF	0.052	NA	24.5
	Composite Nafion/10% ZrO_2		DMF	0.052	NA	27
R. Kumar et al.[127]	Recast Nafion	Solution-cast membrane	DMAc	0.05	0.04	21.2
	Composite Nafion/4%GO			0.05	0.08	37.2
	Nafion 212	Commercial	NA	0.05	0.07	22.1

Figure 2.11b shows the ion conductivity of Nafion/AC nanocomposites with respect to the AC content at two different temperatures, namely, room temperature (RT) and 70 °C both at 50 % relative humidity (RH). The increase in water uptake in the composite membrane shows to improve proton transport mainly due to the higher amount of hydroniums (H_3O^+) that can become available in the hydrophilic regions. The ion conductivities of the Nafion/AC composite membranes were evaluated from the impedance measurements of the membranes sandwiched between two stainless steel blocking electrodes, using the equivalent circuit model as shown in **Figure 2.12a**. The impedance of the polymer electrolyte film constitutes the bulk or total resistance, $\mathbf{R_b}$, in parallel with the bulk membrane capacitance, $\mathbf{C_b}$. and the dominant mechanism at the proton-conducting blocking electrode interface can be represented by the double layer capacitance of the Helmholtz layer. The AC/Nafion composite membranes were found to possess superior ion conductivity up to an order of magnitude improvement compared to that of pure Nafion membrane.

The Nyquist plots in **Figure 12a and b** show the proton conductivity characteristics of pure and composite Nafion membranes at room temperature and 70 °C, respectively. We identify a relatively straight line with an angle of 60– 80° to the real axis in the frequency range of 1 MHz to 100 Hz. A clear semi-circle intercept could not be observed on the real axis at high frequencies as also denoted in other studies of Nafion membranes [128, 129]. The ion conductivities are calculated using

$$\sigma = \frac{l}{RS}, \tag{2.3}$$

where **σ** is the conductivity, **l** is the thickness of the membrane, **R** is the resistance (calculated from real axis intercept of Nyquist plot), and **S** is the surface area of the

membrane.

The circuit model used includes a non-ideal capacitor (**Q**) in series with an ideal capacitor (**C**) and total membrane resistance (**R**) in parallel. The contact resistance of our electrode measurement setup was verified to be close to zero. The initial negative imaginary resistance at high frequency on the **–Z″** axis indicates slight inductance due to the electrode wire loops [128]. Our circuit model matched very well with our Nyquist plots and the associated total resistance values were collected from each model fitting (**Tables 2.2 and 2.3**) and converted to ion conductivity.

Figure 2.13 shows the schematics of Nafion filled with AC nanoparticles and the proposed mechanisms of ion conductivity enhancement. The AC nanoparticle can take a position between two or more neighboring hydrophilic nanochannels in the Nafion and provide cross-channel hydration and proton transport in the membrane. Few studies have investigated the mechanisms of proton conductivity in pure Nafion membrane. Matsuyama et al. [103] proposed an empirical expression for the ionic conductivity as a function of the water fraction for the pure Nafion. In this model, the ion conductivity obeys a simple power law as expressed in **Equation 2.4**:

$$\sigma = \sigma_0 (c - c_0)^n, \tag{2.4}$$

where the only variable is the volume fraction **c** of the aqueous phase in the polymer and $\mathbf{c_0}$, **n**, and $\boldsymbol{\sigma_0}$ are constants. The parameter $\mathbf{c_0}$ refers to the threshold value of **c** below which ionic flow is blocked. According to Matsuyama et al. [103], the value of $\mathbf{c_0}$ is dependent on the spatial dimensions of the system as well as the dispersion configuration of the components (water and polymer). The threshold value $\mathbf{c_0}$ tends to decrease if the components are well dispersed. The critical exponent **n** represents a universally known

constant that is applicable for any percolation system and depends on the spatial dimensions of the system ranging from 1.3 to 1.7.

The fitted pre-factor σ_0 represents the governing parameters of the conduction mechanism obtained empirically. The model represented by **Equation 2.4** has the advantage of separating two main aspects in the ion conductivity prediction: the dimensional and dispersal aspect of the system described by $(c - c_0)^n$ term and the intrinsic conduction properties of the system represented by σ_0.

In another study, Yu Li et al. and Zhen et al. [104, 105] derived an expression of the effective ionic conductivity using the nanostructure of the hydrated clusters in the Nafion membrane, and they verified the influence of water content on ion conductivity. Yang et al. [106] conducted a study on the composite Nafion using zirconium phosphate as filler at high temperatures and proposed an empirical model to fit the proton conductivity as function of the water activity. Recent work by Li et al. [107] elucidated the mechanisms of Li ion conductivity enhancement in polymer nanocomposite electrolytes.

Here, we propose a semi-empirical model of proton conductivity enhancement and degradation in the Nafion/AC composite by considering the characteristics of the AC fillers, Nafion membrane, and the interactions of the filler particle with the nanopores and nanochannels in the Nafion. We start with the basic mechanism that proton transport and conduction is strongly affected by the water content inside the polymer composite. We assume that the fillers at lower contents increase the water uptake inside the membrane. Since the activated carbon particles are porous and absorb water, this will lead to the creation of new spatial distribution of ion conducting proton exchange sites inside the filler pores and the subsequent enhancement of ionic conductivity in the composite.

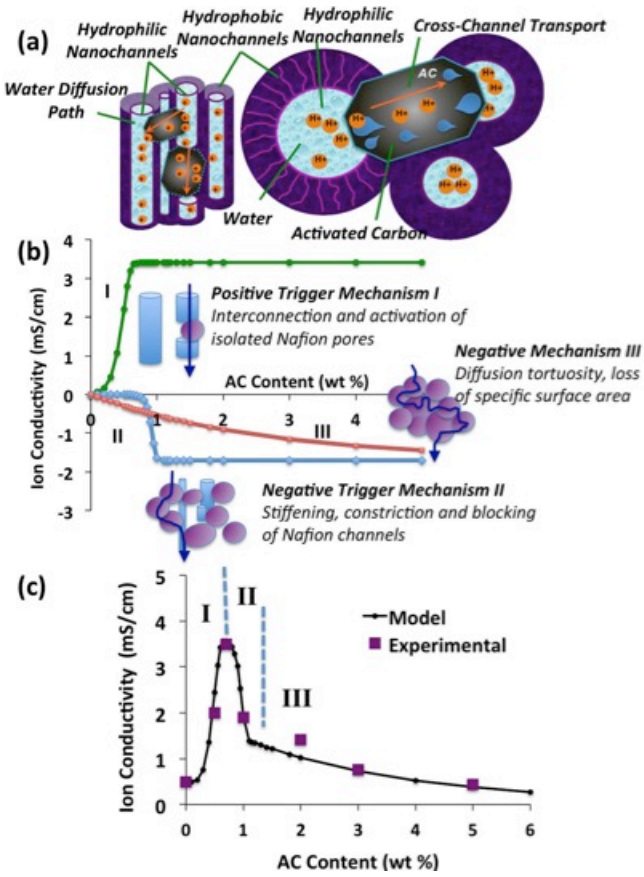

Figure 2-13: (a) Schematics of AC nanoparticles inside Nafion, (b) the proposed mechanisms of conductivity enhancement and adverse effects plotted separately, and (c) our model fitted to the experimental data [102].

In other words, the activation volume in the original proton-conducting membrane can be increased with the formation of new nanochannels inside the porous hydrated carbon filler. Moreover, the AC fillers can act as "connectors" and interconnect the isolated "inactive" nanopores or nanochannels in the Nafion to create continuous and extended proton conduction pathways as depicted in **Figure 2.13a**. Furthermore, we assume that the presence of fillers at low content does not significantly affect the size of the polymer nanochannels. At moderate to high contents, the adverse effects of fillers begin to dominate leading to decrease in proton conductivity as observed in our

experimental results.

The presence of fillers at higher contents can create internal stresses that can constrict, shrink, or block ion-conducting nanochannels in the polymer.

Therefore, based on our experimental data and considering the positive and negative effects of the AC fillers in Nafion, we propose a semi-empirical model of ion conductivity **σ** of polymer nanocomposite electrolyte as a function of filler w presented in **Equation 2.5**:

$$\sigma(w) = \sigma_0 + \sigma_E(w) - \sigma_A(w)\ , \tag{2.5}$$

where

$$\sigma_E(w) = A(1 - e^{-G(w)}), \tag{2.6}$$

$$\sigma_A(w) = B[\left(1 - e^{-H(w)}\right) + \left(1 - e^{-S(w)}\right)]\ \text{,and} \tag{2.7}$$

$$G(w) = qe^{pw}; H(w) = ne^{mw}; S(w) = tw. \tag{2.8}$$

A, B, q, p, n, m, and t are fitting constants. This semiempirical model consists of three main components: the initial conductivity of pure Nafion σ0, the enhancement in conductivity $\boldsymbol{\sigma_E}$, and the degradation component σA where the latter two terms are both functions of filler content w. The enhancement and degradation functions responsible for phase I, II, and III are plotted separately in **Figure 2.13b**. The degradation component of ion conductivity $\boldsymbol{\sigma_A}$ is separated into two terms, one representing a sudden drop in ion conductivity (phase II) and the other exhibiting a slower gradual decline (phase III).

The model is plotted in **Figure 2.13c** and fits well with the experimental results.

From **Figure 2.13c**, we notice a rapid rise in ion conductivity within 0 to 0.7 wt.% of AC content representative of phase I filler effect. The 0.7 wt.% filler content corresponds to maximum water uptake of 70 % (**Figure 2.11a**) where extended continuous proton

transport pathways are created without significant adverse effects. At this content, most likely all isolated "inactive" nanopores and nanochannels are interconnected and activated in proton conduction process. Beyond 0.7 wt.% AC content, a sharp decline in ion conductivity is observed (phase II) followed by a slow gradual decrease (phase III). The sharp decline in proton conductivity (II) observed is attributed to stiffening of polymer membrane as evident by mechanical testing results, and the constriction and blocking of Nafion nanochannels. The gradual decrease in proton conductivity (III) can be due to aggregation of fillers, loss of specific surface area, and transport tortuosity. The constants in **Equation 2.5**, namely, A, B, q, p, n, m, and t, can be associated with the filler properties including size, morphology, internal pore size and distribution, dispersion, specific surface area, and water sorption capability. Furthermore, the Nafion matrix properties including nanopore and nanochannel size and distribution can play a critical role in the extent of filler effects on proton conductivity. The relative contributions of these parameters on proton conductivity enhancement and degradation in Nafion composite should be investigated in future studies.

2.8.4 Conclusions

The effects of coconut shell activated carbon (AC) nanofillers on water sorption, and mechanical and ionic properties of Nafion membrane were analyzed. Our experimental results show that the presence of AC filler could significantly increase the water uptake of the membrane and consequently enhance proton conductivity by about one order of magnitude without a significant compromise in the mechanical properties.

We proposed a new semi-empirical model for the proton conductivity in Nafion/AC

composite considering both enhancement and adverse effects of AC fillers.

Chapter 3: Flexible Thin-film Battery Based on Graphene-Oxide Embedded in Solid Polymer Electrolyte

3.1 Introduction

The worldwide momentum towards flexible electronics, including the commonly used touch-screens and wearable sensors, has focused research efforts on flexible energy storage devices [21, 22]. Lithium-ion batteries (LIBs), based on their superior attributes including high energy density and efficiency, [22, 26, 33] are among the leading candidates to convert into flexible thin films and effectively integrate with flexible electronics and applications (e.g. can be embedded in textiles/fabrics or directly attached to the biological organs).

The critical challenge in this evolutionary phase of flexible LIBs is to obtain mechanical flexibility while maintaining the high electrochemical performance of conventional LIBs including high capacity and cycling stability. Flexible batteries must also yield to a rational assembly process that incorporates a reliable flexible seal [21]. Overall, the next generation LIBs are expected to be smaller, lighter, thinner, and flexible to better facilitate portability and usability. This should be contrasted with conventional batteries that are generally too thick, heavy, and rigid to meet the requirements of burgeoning flexible electronics market [22, 26, 33]. In this study, we develop and investigate flexible thin-film Li-ion batteries based on a relatively safer and more stable solid polymer nanocomposite electrolyte (**Figure 3.1**) that exhibit superior performance with respect to area capacity, energy density and cyclic bending behavior. It is important to note that over the past few years, many novel fabrication techniques and innovative

structural and material designs including nanoscale materials have been utilized to realize high performance flexible LIBs [21, 22, 130]. Nanoengineered and nano-sized materials including metal oxide nanowires [27, 28, 131], carbon nanotubes (CNTs) [25, 30-32, 34, 35, 132], carbon nanofibers and graphene [33-35] have been incorporated as electrodes and current collectors [36, 133-135] in flexible LIBs to improve the interfacial and mechanical properties required in flexible applications subjected to bending, twisting, or folding. For example, Cui's group [25] created a flexible LIB using highly conductive carbon nanotube current collector and a paper dipped in organic liquid as electrolyte/separator, exhibiting high energy density of 108 mW h g^{-1} and 50 bending cycles. Kwon et al. reported a novel design of flexible battery consisting of a spiral Ni–Sn anode with a multi-helix structure, $LiCoO_2$ cathode coated on aluminum wire and liquid organic electrolyte at the center of the structure [136, 137]. The cable battery demonstrated a stable reversible capacity of 1 mA h cm^{-1} with discharging rate of 0.1 C between 2.5 and 4.2 V and excellent mechanical flexibility. Several flexible LIBs reported have incorporated gel or solid polymer electrolytes [138-142]. Skorobogatiy and co-workers [138] fabricated flexible and stretchable batteries composed of $LiFePO_4$ and $Li_4Ti_5O_{12}$ as cathode and anode, respectively, and investigated various solid polymer electrolytes including PEO, formed directly on the surface of the electrode by polymer solution deposition. Lee et al. [139] reported a new concept of fabricating bendable and printable polymer electrolytes composed of ultraviolet cured ethoxylated trimethylolpropane triacrylate (ETPTA) polymer matrix, liquid organic electrolyte, and Al_2O_3 nanoparticles for flexible lithium-ion batteries. Wei et al. proposed a flexible all-solid-state battery with monolayer graphene anode, thin polyethylene glycol electrolyte,

and Li foil cathode that could bend to a 1 mm radius with capacity of 0.02 mA h cm^{-2} over 100 cycles [140]. Yang et al. [141] fabricated a transparent battery created on a flexible polydimethylsiloxane (PDMS) substrate based on a transparent gel electrolyte, exhibiting a capacity of 80 mA h g^{-1} after 15 cycles. Recently, Rogers and co-workers developed a stretchable Li ion battery by using segmented active materials composed of a gel electrolyte, $Li_4Ti_5O_{12}$ and $LiCoO_2$ electrodes and serpentine electrical interconnects with a capacity density of 1.1 mA h cm^{-2} at C/2 and 300% strain capability [142]. Flexible batteries with ceramic solid electrolytes have also been reported. [143, 144] Koo et al. created an all-solid-state flexible LIB with ceramic lithium phosphorus oxynitride electrolyte, $LiCoO_2$ and Li metal electrodes and PDMS encapsulation exhibiting a capacity of ~0.11 mA h cm^{-2}, an upper voltage of 4.2 V, and an energy density of 2.2 mW h cm^{-3} at a rate of 46.5 μA cm^{-2}. A key objective in the development of a solid state flexible LIB is the replacement of the traditional organic liquid electrolyte with high performance solid electrolyte. Ceramic and glass electrolytes such as $Li_{10}GeP_2S_{12}$ can exhibit very high ion conductivity, as high as 12 mS cm^{-1} at 300 K, [145] however, the electrode-electrolyte interfacial issues and mechanical brittleness of the electrolyte pose challenges [146, 147]. Development of high performance flexible solid polymer electrolytes (SPEs) for LIBs has been a major research focus over the past few decades. [11, 37-44, 146, 148] Polymer electrolytes offer many advantages including enhanced safety, flexibility, stretchability higher thermal and electrochemical stability, and thin film manufacturability [37]. The main challenge associated with SPEs is their poor ionic conductivity especially at room temperature (i.e., 10^{-7} to 10^{-8} S cm^{-1}) [40, 45]. Furthermore, non-ideal interfacial contact and high resistance can lead to low utilization

of the electrode materials. Nanoscale fillers have been shown to enhance the ion conductivity of SPEs without compromising the mechanical properties [149-154]. Among the filler types, graphene oxide nanosheets have recently been reported, including our previous work by Ardebili and co-workers [79], to significantly enhance the ion conductivity and thermo-mechanical properties of polymer electrolytes [79-81, 107, 155]. The electrically insulating properties of GO fillers in PEO have also been previously verified [79].

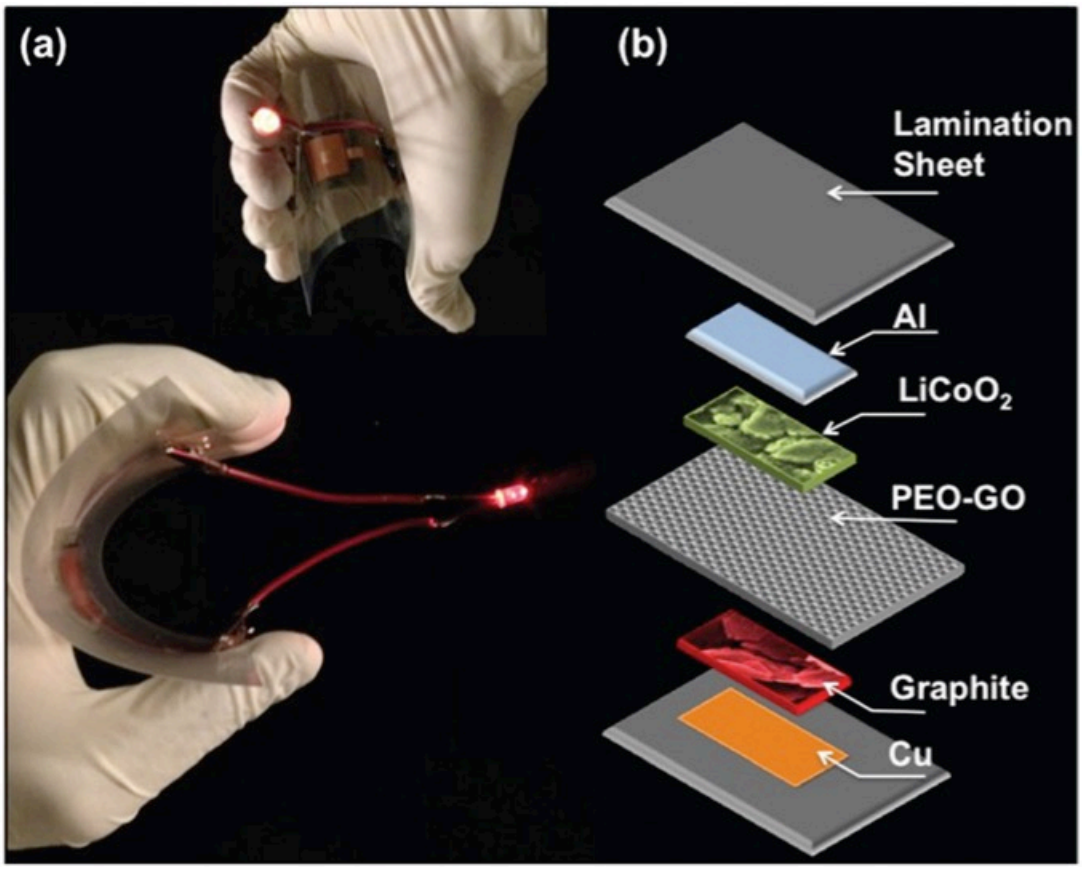

Figure 3-1: (a) Images of flexible Li ion battery based on solid PEO/1%GO electrolyte powering an LED, (b) schematics of the flexible LIB materials and configuration.

In this study, a high performance flexible Li ion battery (**Figure 3.1**) is developed based on a solid polymer nanocomposite electrolyte that exhibits a capacity of 0.13 mA h

cm−2 and good cycling stability over 100 charge/discharge cycles. The polymer nanocomposite electrolyte is composed of 1 wt% graphene oxide (GO) nanosheets embedded in solid polyethylene oxide (PEO) host. The flexible LIB shows a high cut-off voltage of 4.9 V and an energy density of 4.8 mW h cm^{-3} at room temperature, which is within the range of values reported for thin-film LIBs (1–10 mW h cm−3). The battery is encapsulated using a simple lamination process that is scalable and inexpensive. The flexible LIB exhibits robust mechanical flexibility over 6000 bending cycles and good electrochemical performance in both flat and curved positions.

3.2 Experimental Section

3.2.1 Flexible Battery Fabrication

All components of the flexible LIB were stacked onto two commercial plastic sheets with a simple lamination process inside the glove box. Aluminum foil coated with $LiCoO_2$ (cathode) and copper foil coated with graphite (anode) both with ~0.1 mm total thickness were purchased from MTI Corporation.

Lightweight copper tape thin films were used as current collector for both the anode and cathode and were bonded onto the battery electrode materials using the adhesive face of the copper. The area of the solid polymer electrolyte covered all electrode surfaces (area of 4 cm2). Few drops (5 to 7 wt%) of plasticizer (aqueous 1 M LiPF6 in ethylene carbonate and dimethyl carbonate (EC/DMC 1 : 1 vol/vol) were added to the polymer electrolyte surface to enhance interfacial contact and ionic conductivity. In the final packaging phase, the battery was laminated and encapsulated with Scotch thermal laminating polyester sheets (thickness of 3 mm) using Fellowes Saturn2 95 Laminator at 120 °C.

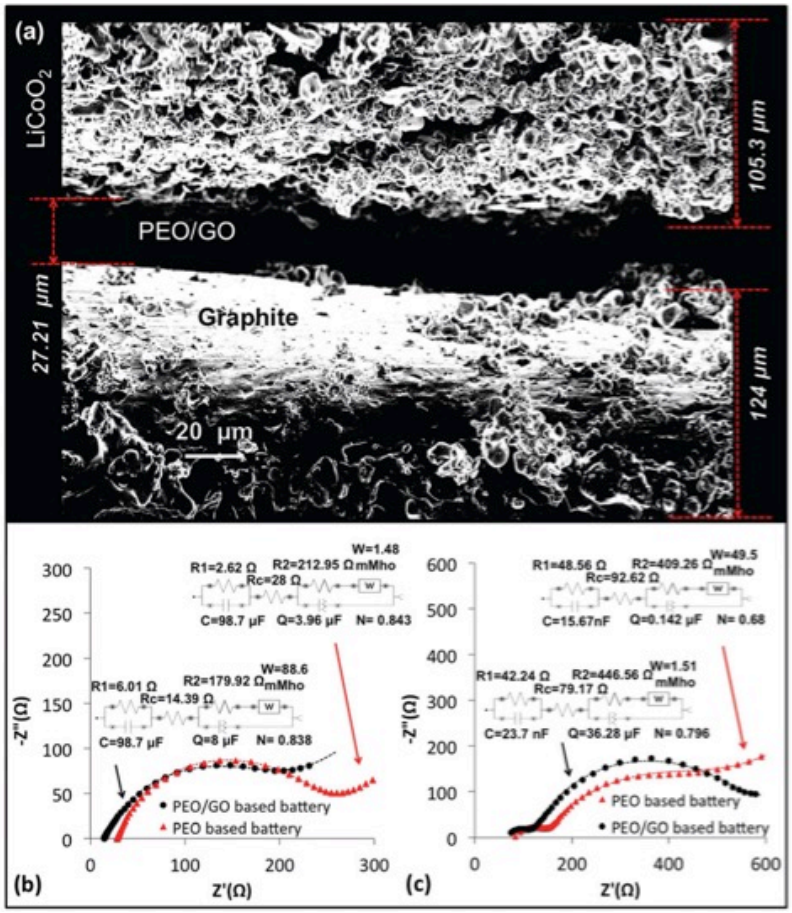

Figure 3-2: (a) SEM image of the cross-section of the flexible LIB, (b) impedance spectra of flexible LIB based on pure PEO and PEO/1 wt% GO, compared in the first charge/discharge cycle and (c) after 100 cycles.

3.2.2 Flexible Battery Electrochemical and Mechanical Testing

All batteries were tested at room temperature, using the multichannel Metrohom Autolab and Arbin BT2000 with direct charge–discharge chronopotentiometry procedure and by applying the adequate current rate with defined lower and higher cut-off voltage (2 to 4.9 V). The CV results were obtained from the cyclic voltammetry potentiostatic procedure using the Autolab by varying the voltage from 1.5 V to 5 V with a scan rate of 0.5 mV s−1. The mechanical bending of the flexible LIBs was conducted using a motorized mechanical testing stand Mark-10-ESM301L. Method of shear by tension

loading was used to evaluate comparative adhesion between the layers in the batteries using Mark-10-ESM301L at a tensile speed of 5 mm min−1 with maximum load capability of 10 N.

3.3 Results and Discussion

The scanning electron microscopy (SEM) image of the cross section of the thin-film flexible Li-ion battery is shown in **Figure 3.2a** revealing a good contact between the battery layers. **Figure 3.2b** and **c** (flat battery) and **Figure B.S2** (bent battery) in the **Appendix B** show the complex impedance spectra of the flexible Li ion batteries. The impedance spectra confirm that adding GO nanosheets reduce the internal and interfacial impedance in the battery. Adding a low content GO can disrupt the ordered packing of semi-crystalline PEO chains and reduce the polymer crystallinity, facilitate salt dissociation, and increase ion conductivity [64, 79, 81, 107, 155-158].

Figure 3.3 illustrates the characteristics of flexible Li-ion batteries based on PEO and PEO/1 wt% GO electrolyte, tested in flat and fixed bending positions (**Table B.S1, Appendix B**). Cyclic voltammetry (CV) measurements (**Figure 3.4**) indicate that the batteries have the same CV shape curve, where the redox peaks vary depending on the electrolyte type and the LIB bending position.

According to **Figure 3.4b**, the highest discharge capacity of 0.14 mA h cm^{-2} is recorded for the bent battery (at 18.9 mm radius) based on PEO + 1 wt% GO. The electrochemical measurements for 100 charge/discharge cycles of the four batteries are presented in **Figure 3.4c** where the voltage ranged between 2 V–4.9 V at a constant current of 1 mA (0.25 mA cm^{-2}). The bent battery with the nanocomposite SPE shows a higher average capacity (0.13 mA h cm^{-2}) compared to that of flat battery. Additional

plots of capacities averaged over 3 flexible battery units are also provided in **Appendix B** (**Figure B.S3–S5**). The bending-induced through-thickness compressive forces appear to further enhance the contact between the SPE and the electrodes, and consequently, decrease the contact resistance between the layers of the battery. The flat battery with pure PEO electrolyte exhibits the lowest capacity further confirming the respective higher internal impedance observed in **Figure 3.2b** and **c**.

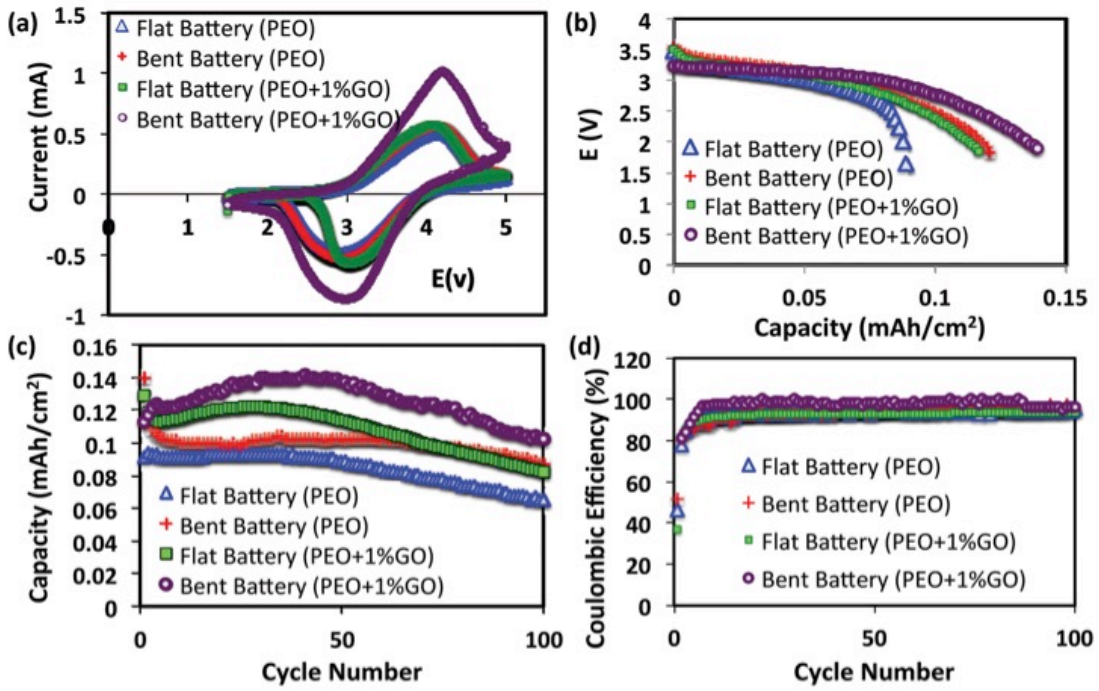

Figure 3-3: (a) Cyclic voltammetry of the flexible batteries, (b) voltage vs. capacity for each battery, (c) discharge capacity during 100 cycles, and (d) coulombic efficiencies of the flexible batteries, discharged at 1 mA (2C) at room condition.

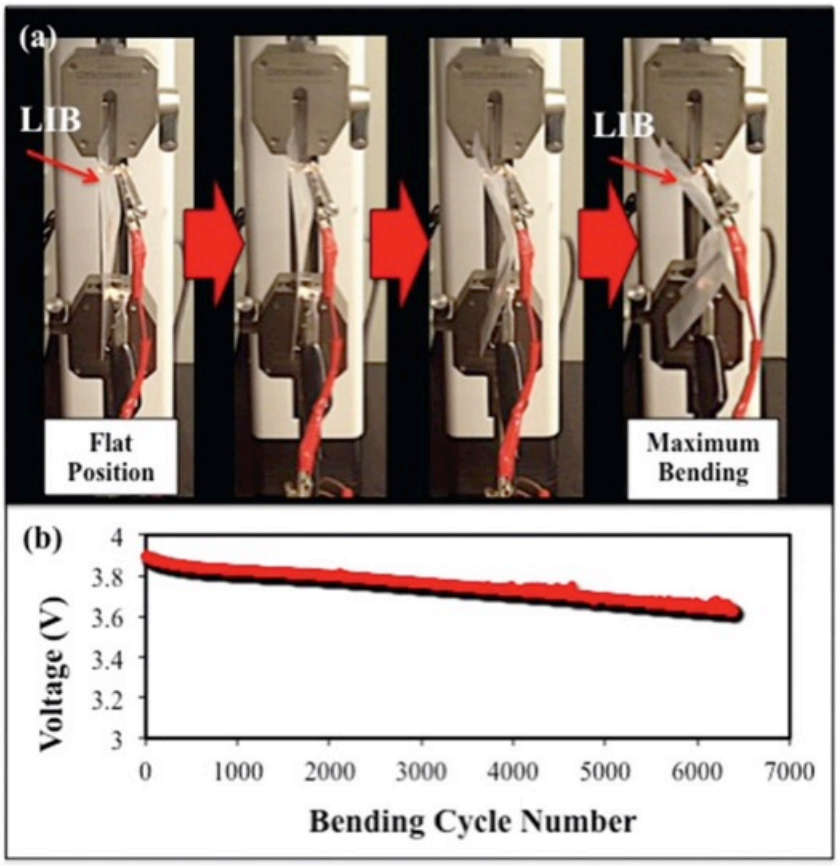

Figure 3-4: (a) Flexible LIB (based on PEO/1 wt% GO electrolyte) subjected to cyclic bending and in situ voltage measurements, and (b) voltage retention vs. bending cycle number at a speed of 8 mm s^{-1}**.**

The coloumbic efficiency of the flexible batteries is displayed in **Figure 3.4d**. All four flexible batteries demonstrate relatively high charge/discharge efficiencies ranging from 91% to 97%. The flexible batteries were also cycled at different current rates of 1 mA, 1.1 mA, 0.5 mA and 0.3 mA over 25 cycles for each rate (**Figure.B.S3 Appendix B**) where all batteries exhibit good cycling stability, especially at 1 mA (2C) and 0.5 mA (1C), maintaining a high capacity retention of more than 85%. Furthermore, a stable capacity between 0.083 and 0.097 mA h cm^{-2} was delivered by the batteries made with pure and nanocomposite polymer electrolytes at flat position when the rate was decreased back to 0.5 mA, suggesting good structural stability of the flexible battery and high

reversibility even after high rate of charge–discharge cycles. The characteristics of the charge and discharge cycling at the first and the 100th cycles are also provided in **Figure B.S4** and **Table B.S1** in **Appendix B.** The capacities of four batteries made with composite electrolyte with different percentages of GO filler under fixed bending radius are also shown in **Figure B.S5**.

Figure 3.5a shows the images of the flexible battery under cyclic bending test from flat to bent position (17 mm radius) with in situ voltage measurement. The results of the flexible

LIB bending test in **Figure 3.5b** show high voltage retention of 93% after 6000 bending cycles. Furthermore, the comparative adhesion of the layers in the flexible battery was evaluated using the method of shear by tension loading (**Figure B.S6 Appendix B**).

The results indicate that a relatively good adhesion is present between the polymer electrolyte and the adjacent electrodes. **Figure 3.5** illustrates the results of the finite element analysis (FEA) of the flexible LIB subjected to the lamination procedure followed by bending which was carried out by a research group member Sean Berg. The modeling details are discussed in the **Appendix B** and the material properties used in the finite element models are presented in **Table B.S2**. The FEA results indicate that the battery lamination/encapsulation phase produces initial compressive stresses in the battery layers. The compressive stresses displayed in **Figure 3.5a**, are found to be higher in PEO/GO composite-based battery compared to pure PEO based battery.

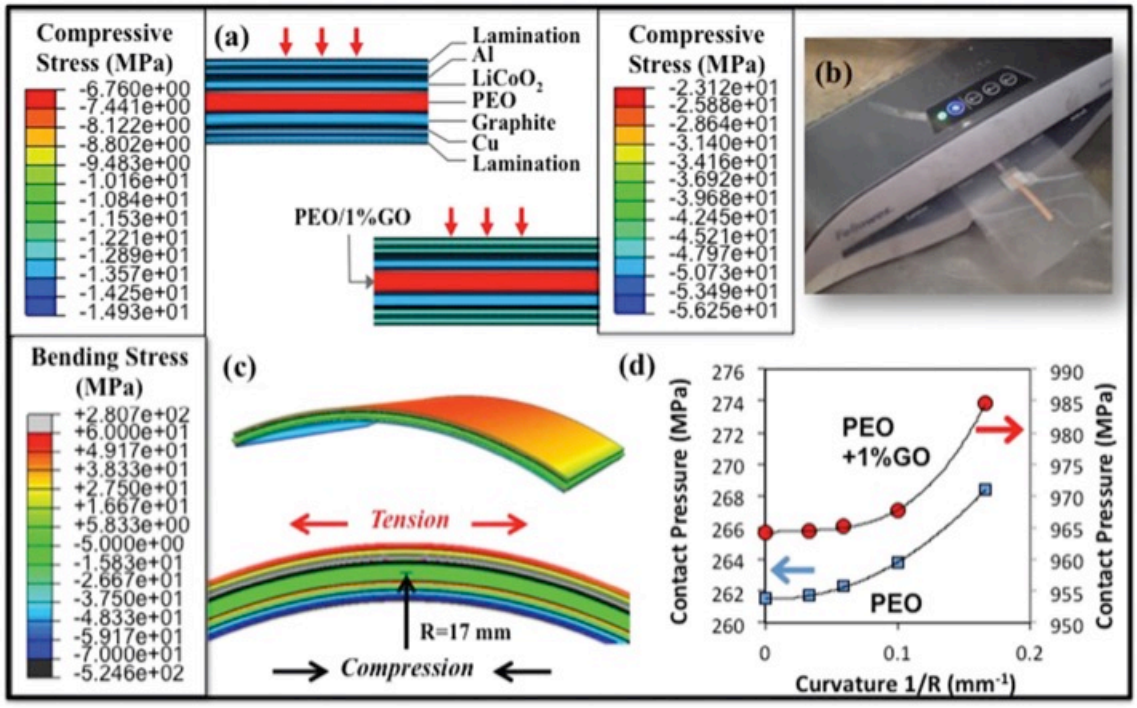

Figure 3-5: (a) Stresses in flexible LIB after the lamination process, (b) a flexible LIB being fed into the lamination machine, (c) bending stresses in flexible battery based on PEO/1 wt% GO electrolyte, and (d) Contact pressure vs. bending curvature in LIBs [159].

Figure 3.5b displays a photo image of a flexible LIB fed into the lamination machine. **Figure 3.5c** shows the FEA results of the battery under bending after the lamination procedure. In the same manner as the experiment, bending was applied as a "column" load that was applied axially to the battery and parallel to the orientation of the layers, to cause the battery to deform in buckling/bending mode. The column load in the FE model was selected to cause a bending radius of 17 mm at the center of the battery at the neutral axis of the electrolyte. The FEA predicts that the contact pressure increases as bending is applied to both types of flexible batteries (**Figure 3.5d**) based on PEO and PEO/1 wt% GO electrolytes.

Overall, the capacities obtained in the present study are observed to be higher than

that reported for ceramic electrolyte based flexible battery [143] and show lower values compared to gel electrolyte based flexible batteries [141, 142]. Furthermore, the polymer nanocomposite electrolyte (PEO/GO) offers improved safety and mechanical stability compared to gel electrolytes [141, 142], mainly attributed to the presence of graphene oxide fillers, and a much lower weight percentage of liquid plasticizer used (i.e., 5–7% in this study) relative to other gel based thin-film batteries (e.g., ~90% 25). Higher cut-off voltage (4.9 V) and good voltage retention over 6000 bending cycles are also promising attributes of PEO/GO based flexible battery. A special advantage of the laminated PEO/GO based flexible battery is the more cost effective, and scalable fabrication procedure compared to other fabrication methods reported [143]. Regarding the electrochemical stability during charge and discharge cycling, ceramic electrolyte based battery reported by Koo et al. [143] displays the highest capacity retention among the reported thin-film flexible batteries. Future studies should focus on improving the encapsulation of the flexible batteries to further lower the capacity fading. The electrochemical performances of previously reported flexible thin film batteries are also summarized in **Table B.S1** in the **Appendix B**.

3.4 Conclusions

In summary, flexible and relatively safer lithium-ion batteries were fabricated based on pure and nanocomposite solid polymer electrolytes (SPEs). Flexible batteries with 1% graphene oxide embedded in polyethylene oxide polymer host showed enhanced performance. Considerably high charge–discharge capacities with relatively low fading rates over 100 cycles were observed while the cyclic mechanical bending test of the

flexible batteries reveal high voltage retention. The battery is encapsulated using a simple lamination procedure that is scalable and cost effective. The laminated flexible LIB provides good electrochemical performance and can function over large ranges of mechanical deformation. Finite element analysis shows the formation of initial compressive stresses during the lamination process and increased contact pressure during bending. The nanocomposite SPE based flexible Li ion batteries pave the way for novel types of safer and more economical energy storage devices that would adapt to stringent space and form requirements of modern flexible applications.

Chapter 4: Stretchable Spiral Thin-Film Battery Capable of Out-of-Plane Deformation

4.1 Introduction

Over the recent years, there has been an increasing demand for deformable energy storage devices including flexible lithium-ion batteries (LIBs) with diverse shapes, sizes, and mechanical properties to integrate with bendable, wearable, and implantable devices and applications [21-23, 160]. The development of flexible and stretchable batteries mainly involves the design and fabrication of reliable and mechanically compliant active and passive materials through a rational assembly process [161]. The main challenge in the fabrication of the stretchable LIBs is to obtain mechanical deformation while maintaining the high electrochemical performance of conventional LIBs including high capacity and cycling stability [6].

In conventional spiral-wound electrode batteries [162-165], the electrode area is usually aligned parallel to the z-axis of the battery, leading to an efficient increase of the active surface area within a limited size rigid battery case. These rigid batteries typically utilize organic liquid or gel electrolytes. Conventional batteries composed of flammable organic liquid electrolytes are generally incompatible with flexible applications due to their rigid packaging, susceptibility to leakage and safety hazards that can lead to fires and explosions. The safety issue in conventional batteries can be addressed through the replacement of the liquid with solid electrolyte made of glass/ceramic or solid polymer. Nevertheless, the application of glass/ceramic electrolytes in flexible and stretchable batteries is limited due to their mechanical stiffness, therefore, deeming polymer-based

electrolytes as the most suitable candidates for stretchable energy storage devices [6, 159, 160, 166].

Numerous thin-film designs [23, 25, 79, 133, 137, 141-143, 167-170] and novel materials.[6, 34, 139, 140, 166, 171, 172] have been developed to achieve deformability and flexibility in energy storage devices. A review of the literature on flexible and stretchable batteries has been broadly provided in previous work [23, 159]. Rogers and co-workers [142] reported a stretchable Li ion battery comprised of segmented active materials connected through stretchable serpentine electrical interconnects. The battery is made of $Li_4Ti_5O_{12}$ and $LiCoO_2$ electrodes and liquid/gel electrolyte, and exhibits an areal capacity of 1.1 mAh cm^{-2} at C/2 and 300% strain capability. Another study by Kwon *et al.* [137] reported the design of a flexible cable-type Li-ion battery based on a hollow multi-helix Ni–Sn anode, a modified polyethylene terephthalate separator, and a $LiCoO_2$ cathode coated onto an aluminum wire. The electrolyte used in this battery was a liquid organic electrolyte injected at the center of the electrode assembly. The cable battery exhibited a stable reversible capacity of 1 mAh cm^{-2} with discharging rate of 0.1C between 2.5 and 4.2V until 10 cycles, and demonstrated high mechanical flexibility and strength under severe bending and twisting conditions.

In the present work, a spiral design is proposed for a stretchable thin-film Li-ion battery (< 1 mm thick) that is capable of large out-of-plane deformation of 1300 % while simultaneously offering electrochemical functionality (**Figure 4.1**). The stretchable spiral battery is made with based on solid polymer nanocomposite electrolyte composed of polyethylene oxide (PEO) and 1 wt.% graphene oxide (GO) and is encapsulated with plastic lamination sheet. The solid PEO/GO electrolyte provides higher ionic

conductivity and transference number relative to the pure polymer electrolyte. Cyclic voltammetry of the spiral battery confirms that the PEO/GO electrolyte is compatible with the conventional battery electrodes (i.e., lithium cobalt oxide and graphite) and no side reactions are observed during the polarization. The spiral Li-ion battery displays robust mechanical stretchability over 9000 stretching cycles and an energy density of 4.862 mWh/cm^3 at 650% out-of-plane deformation and provides an average capacity above 0.1 mAh/cm^2 in different stretching configurations. The finite element analysis of the spiral battery provides insights on the torsional stresses and displacements in the battery during stretching. Spiral batteries based on solid polymer electrolyte provide improved safety and can be employed in a wide range of applications, including deformable or irregularly shaped medical implants, piezoelectric technologies, robotic applications and textile industries.

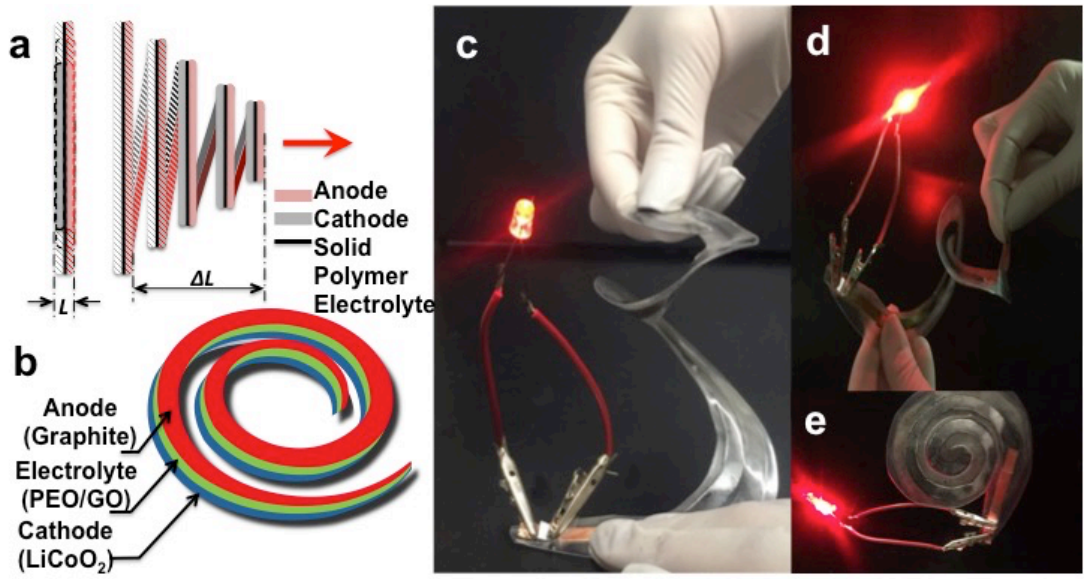

Figure 4-1: (a)-(b) The schematics of the spiral Li-ion battery, (c)-(d) photo image of the fabricated spiral battery in stretched positions lighting a red LED, (e) spiral battery in flat position [173].

4.2 Experimental

The cyclic voltammetry tests of the same spiral battery in both positions flat and stretched were obtained from the potentiostic procedure using the Autolab by varying the voltage from 0 V to 5 V with a scan rate of 0.5 mV s^{-1}.

4.2.1 Stretchable Spiral Battery Fabrication

The spiral thin-film lithium-ion battery is composed of $LiCoO_2$/Al as cathode/current collector, graphite/Cu as anode/current collector, both purchased from the MTI Corp., and the solid polymer nanocomposite electrolyte, placed between the electrodes. Few drops (5 - 7 wt%) of non-aqueous 1 M $LiPF_6$ in ethylene carbonate and dimethyl carbonate (EC/DMC 1:1 vol/vol) is used as plasticizer to enhance the ionic conductivity of the solid polymer electrolyte. Furthermore, the 5 - 7 wt% liquid electrolyte can aid with the adhesion between the electrode/electrolyte surfaces to enhance both the electrochemical and mechanical performance of the battery. A special glue (Bondic) as a liquid plastic welder is used to enhance the sealing of the spiral battery. The battery is assembled through laminating multiple layers of the battery into two commercial sheets of plastic lamination paper, using a simple office-type lamination machine, inside the argon filled dry glove box. The thickness of the final fabricated spiral battery is about 0.75 mm and its area is about 9 cm^2 in unstretched (flat) position.

4.2.2 Electrochemical and Mechanical Testing of Spiral Batteries

The electrochemical performance of the spiral batteries was measured at room temperature, using the multichannel Metrohom Autolab and Arbin BT2000 with direct

charge-discharge chronopotentiometry procedure and by applying an adequate current rate (1mA) with defined lower and higher cut-off voltage (2.8 to 4.5 V).

Complex impedance spectra were obtained using Metrohm Autolab Frequency Response Analysis (FRA 2) with frequency range capability from 10 μHz to 10 MHz. All the batteries were tested by setting up the equipment in the frequency range between 10 Hz and 1 MHz with the amplitude of ± 10 mV.

The mechanical tensile test of the spiral LIBs was conducted using a motorized mechanical testing stand Mark-10-ESM301L at a stretching speed of 1000 mm/min while measuring the voltage drop of the spiral battery with the Metrohom Autolab.

4.3 Results and Discussion

Figures 4.1a and **4.1b** show the schematics of the thin-film Li ion battery in spiral configuration consisting of graphite as anode, solid polymer nanocomposite electrolyte, and lithium cobalt oxide as cathode. Based on the spiral design of the electrode and electrolyte materials, the battery can be stretched from the base plane (flat configuration) to extended spiral battery in out-of-plane direction. **Figures 4.1c-1e** show the fabricated spiral battery in various configurations lighting the red light-emitting diode (LED). This fabricated spiral battery is about 0.75 mm thick, and can stretch as high as 15000 % to about 120 mm in height and light an LED, as demonstrated in **Figure 4.1c**.

Polyethylene oxide (PEO) polymer matrix with 1 wt% GO has been found previously to show enhanced ion conductivity and mechanical properties compared to pure PEO [79]. The electrically insulating properties of PEO/1 wt% GO have also been previously verified and PEO/1%GO was determined to be a suitable electrolyte for a Li ion battery[79].

To investigate the compatibility of the solid nanocomposite polymer with the battery electrodes, cyclic voltammetry (CV) test was performed as displayed in **Figure 4. 2**. For the same spiral battery under different configurations (flat and stretched) similar CV shapes with small variation of the redox peaks are observed.

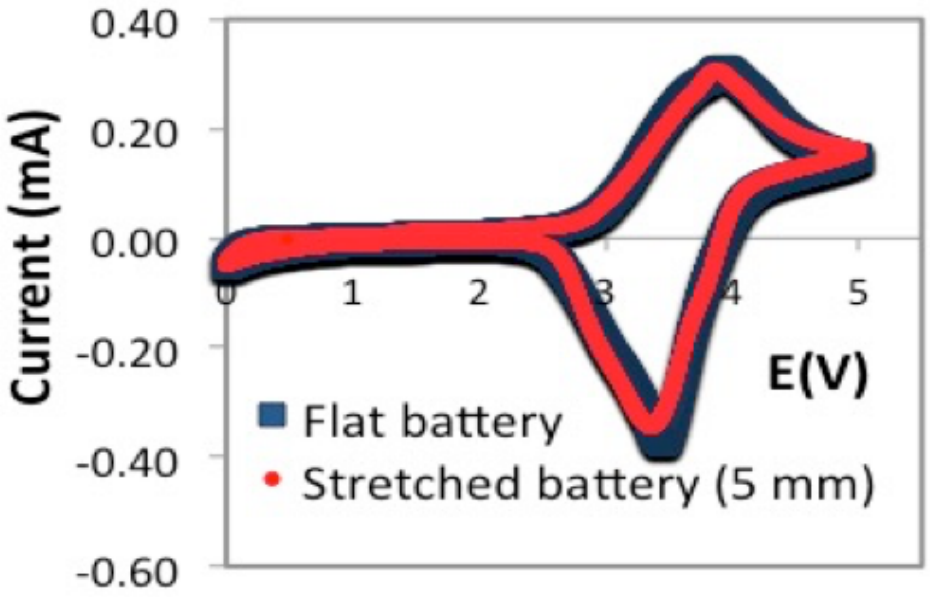

Figure 4-2: Cyclic voltammetry of the spiral battery under flat and stretched conditions [173].

The electrochemical performance of the spiral batteries was investigated under different configurations. **Figure 4. 3a** shows the charge-discharge capacities of the spiral batteries in flat (unstretched) and stretched (5mm) configurations measured between 2.8 V and 4.5 V, at a constant current of 1 mA. Charge and discharge cycling test was carried out at room temperature conditions and the device showed a good performance over 100 cycles. A large capacity (≈ 0.14 mAh/cm^2) is observed during the first cycle, and further charge and discharge cycles resulted in an average capacity of 0.1 mAh/cm^2. The highest discharge capacity of 0.14 mAh/cm^2 is recorded for the battery in flat position. The spiral

LIBs exhibits a relatively high maximum operating voltage of 4.5 V. The calculated energy density was 5.52 mWh/cm^3 for the battery in flat position and 4.862 mWh/cm^3 for the battery stretched at 5 mm (650 % extension). The properties of the spiral batteries are also listed in **Table S1** in **Appendix C**.

Figure 4.3a reveals that upon stretching the spiral battery to 5 mm (650%), the battery experiences an initial capacity drop, however a steady cyclic capacity fading is maintained similar to that of the unstretched spiral battery. The capacity fading over 100 cycles is mainly attributed to the external environmental effects directly related to the encapsulation of the thin-film battery. Further improvement in encapsulation can enhance the cyclic capacity fading. **Figure 4.3b** shows the coulombic efficiencies of stretched and unstretched spiral batteries maintained above 90% over 100 charge/discharge cycles. The first cycle is characterized by a very low coulombic efficiency due to the irreversible loss of the Li from cathode in the permeable SEI layer formed on the anode. The capacity of a spiral battery upon stretching to 10 mm (1300 % extension) appears to drop further as shown in **Figure 4.3c**. To investigate the effect of stretching on the internal impedance of the battery, electrochemical impedance spectroscopy (EIS) of the fresh and cycled spiral batteries in both flat and stretched configurations were performed, and the results are shown in **Figure 4.3d,e**. The impedance spectra confirm that the internal impedance including the contact resistance between the battery layers are increased as the spiral battery is stretched by 650%. This increase in impedance can be related to the tensile and torsional stresses and strains produced in the layers of the spiral battery during stretching. After 5 charge/discharge cycles, the impedance of the spiral battery is observed to increase compared to that of the fresh battery in the flat (unstretched) position which can

be attributed to the formation of solid electrolyte interphase (SEI) layer. Furthermore, the impedance of the stretched battery after 5 cycles appears to be unchanged compared to that of the fresh stretched battery, which indicates that the stretching stresses and strains have a more dominant effect on the battery impedance compared to the SEI layer.

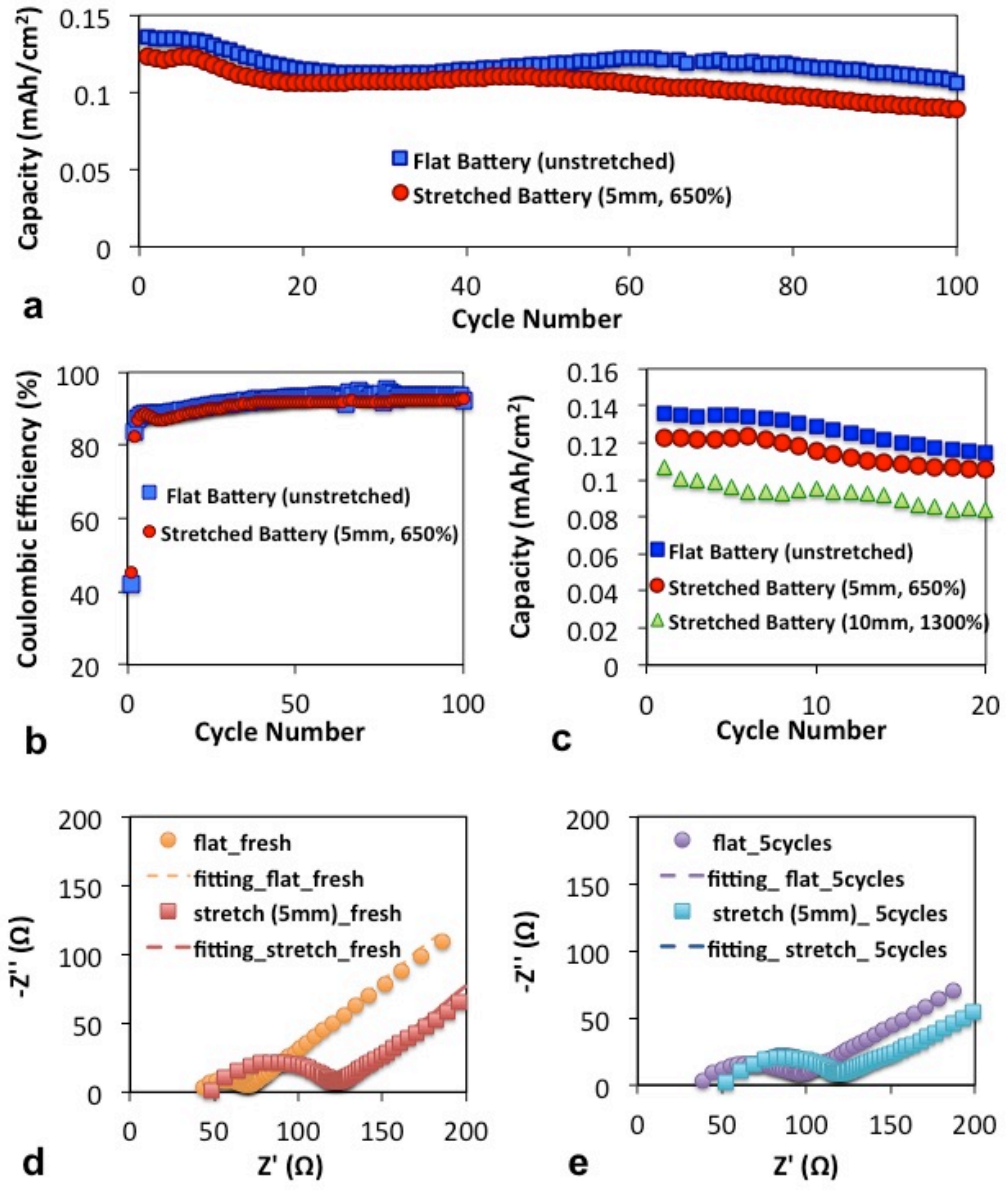

Figure 4-3: (a) Discharge capacity during 100 cycles, (b) coulombic efficiencies of the spiral batteries, (c) capacity vs. stretching distances, (d) impedance spectra for unstretched (flat) and stretched batteries (d) in fresh condition

The effect of stretching cycles on the spiral battery performance was also investigated. **Figures 4.4a and 4b** show the results of stretching cycling test of a spiral LIB and an image of the spiral battery under cyclic stretching test with simultaneous *in situ* electrochemical testing, respectively. The spiral LIB undergoes maximum stretching length of 5 mm with a stretching speed of 1000 mm/min. The battery shows a voltage drop of only 12% after 9000 stretching cycles.

and (e) after 5 cycles [173].

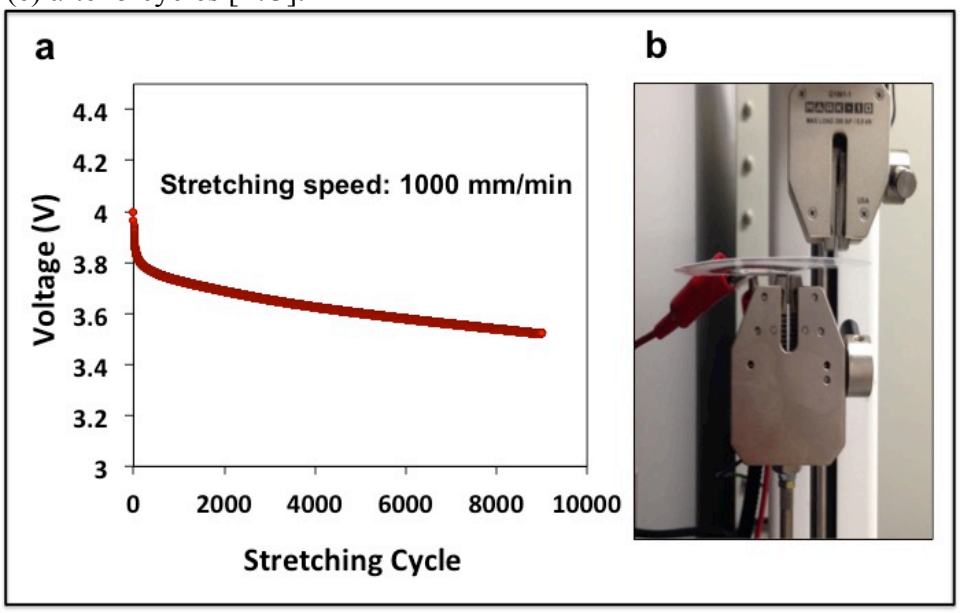

Figure 4-4: (a) The voltage retention vs. stretching cycle number of spiral LIB at a speed of 1000 mm/min, (b) image of the spiral LIB subjected to cyclic bending and in-situ voltage measurements [173].

A numerical analysis using the finite element method was carried out by a group member (Sean Berg) to better understand the mechanical response and the state of loading and stress within the spiral battery in the stretched state. The spiral pattern geometry was generated based on the flexible battery design and the layers were stacked in the same configuration as in the experiment, as shown in **Figure 4.5a**. An elastic stress material model was assumed and the material properties were defined as per the lab

flexible battery materials including the laminate, electrodes, current collectors, and polymer electrolyte (**Table C.S2 Appendix C**). Further discussion of the modeling approach is provided in **Appendix C**. In order to properly simulate the response due to extension under loading, one end of the battery was fixed while the other end had a displacement load applied to it in the axial direction.

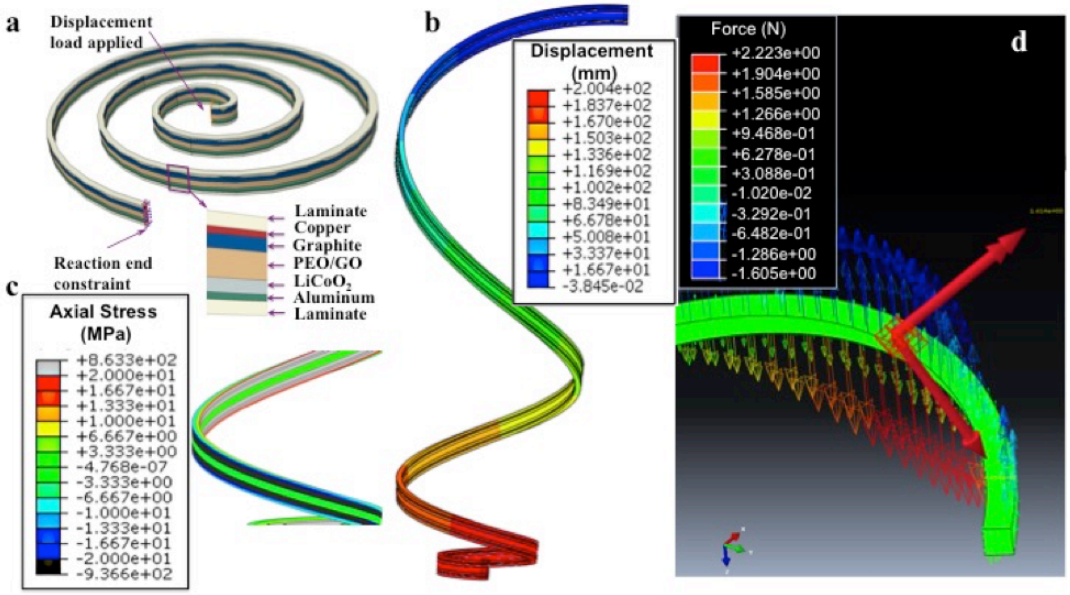

Figure 4-5: (a) Finite element model of spiral battery (b) strain variation in stretched spiral battery (c) stress variation in spiral battery, (d) cross-sectional force variation indicating the state of torsion in the spiral battery [173].

Figures 4.5b and 4.5c show the axial displacement gradient and state of stress during the extension process, respectively. **Figure 4.5d** shows a plot of the force variation across the spiral cross-section corresponding to the torsional direction, indicating a resulting torsional moment. The extension results in a normal bending moment in addition to the torsional moment, both of which increase with increasing spiral radius, which is expected since the moment arm from the center increases. This is further demonstrated in **Figure 4.5c**, which shows a stress variation, from tensile to compressive, through the cross-

section. The extension of the battery results in the displacement gradient shown in **Figure 4.5b**, with increased displacement/extension as the spiral radius increases from the center. While the torque, moment and displacements increase along the axial direction of the battery and with increasing spiral radius, the stress appears evenly distributed throughout the battery length at the equilibrium state. The numerical analysis confirms that a robust lamination, encapsulation and packaging of the battery are crucial to maintain the electrochemical performance of the spiral battery at higher stretching due to the increased mechanical torsion and displacements [173].

4.4 Conclusion

In summary, the design, fabrication, and packaging of stretchable spiral thin-film lithium-ion battery was demonstrated that is capable of simultaneous electrochemical and mechanical functions. The configuration of the spiral LIB can be used in a wide range of applications including wearable and implantable devices. The spiral batteries provide large (i.e., 1300%) out-of-plane deformation and good voltage retention after 9000 stretching cycles. The robust spiral thin-film structure based on solid polyethylene oxide and 1% graphene oxide offers improved safety, good electrochemical performance, and the ability to function over large ranges of mechanical deformation.

Chapter 5: Temperature Effects in Nanocomposite Polymer Based Lithium-Ion Batteries

5.1 Introduction

Lithium-based batteries are particularly attractive due to their high energy densities and high capacities. The enhanced safety and stability of solid-state, secondary batteries make them suitable for a wide range of diverse applications, compared to conventional, liquid electrolyte based batteries. Solid electrolytes provide the ability to prevent lithium dendrite growth, making solid-state batteries inherently safer. Both solid polymers and ceramics are suitable alternatives to liquid electrolyte, but solid polymer electrolytes offer the specific advantage of high flexibility and stretchability that ceramics cannot provide. Poly(ethylene oxide) (PEO) based electrolytes are commonly used for PEO's ability to effectively solvate large quantities of lithium salts, which are necessary for lithium-ion conduction.

Although PEO is a good lithium-ion conductor compared to many other polymer-based electrolytes, higher conductivities are needed for battery applications. The superior ionic conductivity of PEO is due to fast ionic transport occurring in amorphous regions of the semi-crystalline polymer. This would suggest that conductivity decreases with the increase of crystallinity degree. Introducing GO nanofillers into polymer structure is one approach used to enhance ion conductivity of polymer electrolytes, as presented in Chapter 2. Alternatively, operation at elevated temperatures is another approach to achieve increased ion conductivity.

Different electro-thermal models of LIB have been introduced in literature [46-48,

174-176]. For example, Newman and Doyle presented an isothermal and adiabatic discharge model of LIB behavior [46, 174] in which the discharge performance was determined by including an energy balance equation into an existing two-dimensional porous electrode model of lithium-ion intercalation [162, 175, 176]. Various mathematical models have been developed to predict the transient electrochemical and thermal behavior of Li-ion batteries by incorporating separate heat source terms and adding temperature dependent parameters (i.e., diffusivity, conductivity, etc.) [47, 48, 162, 175].

In contrast, the thermo-mechanical effects on LIB performance have not been fully investigated. Possible thermo-mechanical effects that impact battery discharge behavior include microcracks, structural disintegration, and delamination, all of which could lead to poor contact along the electrode/electrolyte interface, capacity degradation, or battery failure [177-179].

In this chapter, temperature effects on solid polymer electrolyte based coin cell batteries are investigated. The electrochemical performance of the batteries demonstrates that the 1%wt. GO nanofiller has a favorable effect on the performance of batteries operating at high temperatures

Moreover, a single particle model for the LIB was developed to predict the first discharge cycle of coin cell batteries at different temperatures based on the 1D model formulation presented in the references [48, 175]. The calculations of the model were performed using COMSOL MULTIPHYSICS®(Version 5.0).

Finally, examination of the model's conformity to the experimental charge and discharge data provides insight into the impact of different parameters (i.e.,

thermodynamic, kinetic, and design) on the battery performance. This investigation benefits LIB engineers and scientists by providing additional and predictive information on LIB performance, as well as design guidance, that can reduce the costs and efforts of experimentation.

5.2 Experiments

5.2.1 Coin Cell Battery Fabrication

All components of the coin cell LIB were stacked inside CR2032 Coin Cell Cases (20d x 3.2t mm) with O-rings and assembled inside the glove box. The battery cathode and anode, consisting of $LiCoO_2$ on aluminum foil and graphite on copper foil, respectively, both with a ~0.1 mm total thickness, were purchased from MTI Corporation. The solid polymer electrolyte (area of 1.73 cm^2) was cut to ensure complete coverage of the electrode areas to prevent internal shorting. The battery also contained a 7 wt% content of plasticizer (aqueous 1 M $LiPF_6$ in 1:1 vol/vol of ethylene carbonate (EC) and dimethyl carbonate (DMC)) added to the polymer electrolyte surface to enhance the electrode/electrolyte interfacial contact and, ultimately, ionic conductivity.

5.2.2 LIB Electrochemical and High Temperature Testing

All batteries underwent chronopotentiometry (Arbin BT2000) in a RH chamber (BTL 433). The batteries were charged-discharged at a constant 0.1 mA current between 2.8V to 4.2V.

5.3 1D Isothermal Model

5.3.1 Nomenclature

c_s Concentration of lithium in the solid particles

D_s	Solid phase diffusion coefficient
r_p	Radius of the electrode particle
$R_{Li\Theta}$	Molar flux of lithium caused by the electrochemical reactions at the particle surface
$i_{applied}$	Applied current density
ε_s	Volume fraction of the solid phase active material in the electrode
L	Thickness of the electrode
S	Area of the electrode
F	Faraday constant
k_b	Boltzmann Constant
i_{loc}	Exchange current density
SOC	State of charge
$c_{s,surf}$	Surface concentration
$c_{s,max}$	Maximum concentration
E_{eq}	Equilibrium potential
ϕ_s	Potential of the solid phase
ϕ_l	Potential of the solution phase
η	Overpotential
i_0	Initial Exchange current density
κ	Reaction rate constant
cl	Solution phase concentration
cl,ref	Reference solution phase concentration (taken to be equal to 1 mol/m^3)
R	Gas Constant
$R_{electrolyte}$	Electrolyte Resistivity
Cp	Heat capacity at Constant pressure
ρ	Density
Ea,j	Activation energy for solid phase diffusion coefficient of electrodes
h	Heat transfer coefficient lumped factor
α	Correction factor of the temperature
Ecell	Cell potential

5.3.2 Model assumptions

The developed electro-thermal model presented in this chapter is based on the single particle models of Guo and Ye [48, 175]. The model assumes the following:

1) The active materials of the solid electrodes are homogenous and the intercalation particles in the porous electrodes are assumed to be spherical and identical size;

(2) There are no side reactions; In the real LIB system, side reactions may occur due

to the solid electrolyte interface (SEI), electrolyte decomposition, and solvent reduction reaction. These side reactions will lead to irreversible capacity loss. The incorporation of the SEI growth and electrolyte decomposition can be further investigated for future work to predict the cycle life to the LIB.

(3) The current collectors have a negligible impact on lithium-ion transfer and heat transfer; It is well known that the most common utilized current collector in the battery system such as the copper and aluminum are very good thermal conductor and this can impact the battery performance. However, this assumption is reasonable for low applied current densities and small sample dimensions.

(4) Diffusion of ions into active materials is assumed to be Fickian. In fact, non-fickian transport may occur due to several effects like the effect of structural changes, relaxation, swelling, internal stresses caused by the temperature variation, age and pre-history of the device, and sample dimensions. All these factors are neglected in this work based on the first assumption.

5.3.3 Governing Equations

5.3.3.1 Ion Diffusion

In this model, the diffusion of lithium-ions into the active material particles, of both the positive and negative electrodes, is assumed to be Fickian and therefore, described using Fick's second law[46, 175],

$$\frac{\partial c_{s,j}}{\partial t} = \nabla.\left(D_{s,j}\nabla c_{s,j}\right), \tag{5.1}$$

(j =pos, neg)

where $\mathbf{c_s}$ is the concentration of lithium in the solid particles and $\mathbf{D_s}$ is the solid phase diffusion coefficient.

The above diffusion equation is solved for both the positive and negative electrode particle. The equation is written in polar coordinates to facilitate its implementation using the General Form PDE interface: [174]

$$\frac{\partial c_{s,j}}{\partial t} = D_{s,j}\frac{\partial^2 c_{s,j}}{\partial r^2} + 2\frac{D_{s,j}}{r}\frac{\partial c_{s,j}}{\partial r}\,. \tag{5.1}$$

The diffusion coefficient is considered to be a temperature dependent parameter. According to the Arrhenius equation, the diffusion coefficient in a solid at different temperatures is

$$D_{s,j} = D^0{}_{s,j}e^{-\frac{E_a}{R}\left(\frac{1}{T_{ini}}-\frac{1}{T}\right)}, \tag{5.3}$$

where $\mathbf{D^0_s}$ is the diffusion coefficient (m^2/s) at the initial temperature, $\boldsymbol{E_a}$ is the activation energy for diffusion (J/atom), **T** is the temperature (K), and **R** is the ideal constant (8.314 J/mol.K). The exponential form of this relation means that diffusion coefficients in the solid phase can grow quickly with temperature.

The boundary conditions at the center and surface of the particle are defined respectively as: [175]

$$\frac{\partial c_{s,j}}{\partial t} = 0\Big|_{r=0} \; and \tag{5.4}$$

$$-D_{s,j}\frac{\partial c_{s,j}}{\partial t} = R_{Li\theta,j}\Big|_{r=rp,j}, \tag{5.5}$$

where r_p is the radius of the electrode particle and $R_{Li\Theta}$ indicates the molar flux of lithium caused by the electrochemical reactions at the particle surface. The molar flux of lithium is related to the applied cell current [175] and is defined as

$$R_{Li\theta,j} = \frac{i_{loc,j}}{F} = \frac{\mp i_{applied}}{F(3r_{p,j}\varepsilon_{s,j}L)}, \tag{5.6}$$

where $i_{applied}$ is the applied current density, ε_s is the volume fraction of the solid phase active material in the electrode, and L is the thickness of the electrode.

5.3.3.2 Intercalation Reaction Kinetics

The intercalation reaction kinetics is expressed using the following Butler-Volmer expression, [46, 174]

$$i_{loc,j} = i_{0,j}(\exp\left(\frac{0.5F\eta_{,j}}{RT}\right) - \exp\left(-\frac{0.5F\eta_{,j}}{RT}\right)), \tag{5.7}$$

where the overpotential $\boldsymbol{\eta}$ depends on $\boldsymbol{\phi_s}$ the potential of the solid, $\boldsymbol{\phi_l}$ the potential of the solution phase and the equilibrium potential of each electrode [46, 174] and it is expressed as:

$$\eta_j = \Phi_{s,j} + \Phi_{l,j} + E_{eq,j}\ . \tag{5.8}$$

The equilibrium potentials of the graphite and $LiCoO_2$ were defined from the literature [4, 174]. **Figure 5.1** shows that the equilibrium potential parameter Eeq for the negative and positive electrodes is a function of the battery's state of charge (SOC),

$$SOC = \frac{c_{s,j}^{surf}}{c_{s,j}^{max}}, \tag{5.9}$$

where c_s^{surf} and c_s^{max} are the surface and maximum concentration of lithium-ions in the electrode particles, respectively.

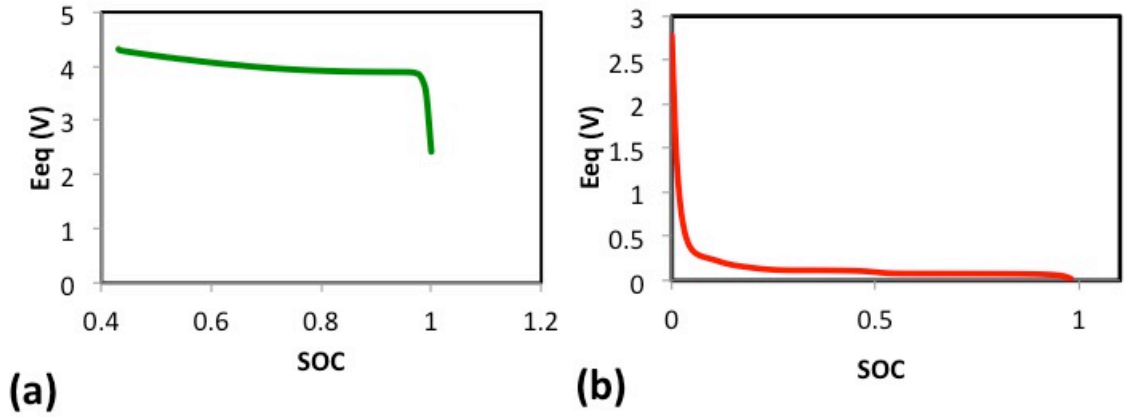

Figure 5-1: Equilibrium potential vs SOC for (a) $LiCoO_2$ and (b) graphite.

The Butler-Volmer kinetic expression is re-written in terms of the inverse hyperbolic function in order to improve computational efficiency. An expression for the solid phase potential for each electrode can be obtained as

$$\Phi_s = \Phi_l + E_{eq} + \frac{RT}{0.5F}\text{asinh}\left(\frac{i_{loc}}{2i_0}\right), \tag{5.10}$$

where the exchange current density i_0 is defined as

$$i_{0,\text{j}} = F\kappa_j\sqrt{(c_{s,j}^{max} - c_{s,j})c_{s,j}(c_{l,j}/c_{l,j}^{ref})}, \tag{5.11}$$

where κ is the reaction rate coefficient inside the electrode, c_l is the solution phase concentration which is taken to be equal to a constant value in the single particle model [175], and $c_{l,\text{ref}}$ is the reference solution phase concentration.

The potential drop in the electrolyte between the positive and negative electrodes is taken as

$$\Phi_{l,pos} - \Phi_{l,neg} = -i_{applied}R_{electrolyte}, \tag{5.12}$$

where $R_{\text{electrolyte}}$ is the electrolyte resistance, which is actually determined based on the experimental data. In this model the $R_{\text{electrolyte}}$ is an adjustable parameter, which could depend on cell temperature and the type of the used electrolyte.

$$R_{electrolyte} = R^0{}_{electrolyte}(1 + \alpha(T_{init} - T)), \tag{5.13}$$

where T is the temperature and α is a correction factor for the actual resistance of the electrolyte .

The cell potential is determined as follows:

$$E_{cell} = \Phi_{s,pos} - \Phi_{s,neg}. \tag{5.14}$$

5.3.3.3 Energy Balance

Generally, heat generation within lithium-ion battery can be classified into three types:

- irreversible heat due to the electrochemical reaction polarization between active material particle surface and the electrolyte;
- irreversible ohmic heat due to the ohmic potential drop;
- reversible heat caused by the reaction entropy change during charge and discharge.

In this work, we neglect the heat exchanged between the cell and the surroundings.

The following equation governs energy balance in lithium-ion battery. There are three parts of heat sources during charge and discharge processes, including reaction heat Q_{rea}, ohmic heat Q_{ohm} and active polarization heat $Q_{act.}$

$$\rho C_p \frac{\partial T}{\partial t} = Q_{rea} + Q_{act} + Q_{ohm}, \tag{5.15}$$

where T is the cell temperature , Cp is the heat capacity (J (kg K)−1), ρ is the density (kg m^{-3})

The reaction heat is defined as

$$Q_{rea} = I_{applied} T \left(\frac{\partial \mathrm{E}^{*}_{eq,pos}}{\partial T} - \frac{\partial \mathrm{E}^{*}_{eq,neg}}{\partial T}\right), \tag{5.16}$$

where

$$\mathrm{E}^{*}_{eq,j} = \mathrm{E}_{eq,j} + (T - T_{init}) \frac{dEeq_{,j}}{dT}, \tag{5.17}$$

and the active polarization heat is

$$Q_{act} = I_{applied} \left(\eta_{pos} - \eta_{neg}\right). \tag{5.18}$$

The ohmic heat is defined as

$$Q_{ohm} = I_{applied}^2 R_{electrolyte} . \quad (5.19)$$

According to Newton's cooling law, the boundary condition for energy balance is expressed as

$$-\lambda \frac{\partial T}{\partial x}\Big|_{x=0;x=ln+lelectrole+lp} = \mathrm{h}(T_{inits} - T), \quad (5.20)$$

where h is lumped heat transfer coefficient and Tamb is the ambient temperature.

The anode, cathode, and electrolyte parameters used in this model are listed in **Table 5.1**.

Table 5-1. Model parameter values for the coin cell battery based on nanocomposite electrolyte

Symbol/unit	Anode: Graphite	Electrolyte: PEO+1%wt. GO	Cathode: $LiCoO_2$
$c_{s,}^{max}$[mol/m^3]	26390		22860
cl, [mol/m^3]	14870		12300
D^0_s [m^2/s]	5.5*10^{-14}		4.2*10^{-14}
r_p[μm]	97		78
ε_s	0.428		0.411
ρ [kg/m^3]	2270		4678
C_p [J /kg K]	881		700
E_a [kJ/mol]	48		35
κ [m/s]	2*10^{-11}		2*10^{-11}
α [K^{-1}]		0.01	
$R^0_{electrolyte}$ [Ω.m^2]		0.32 at 25C	
cl,ref [mol/m^3]		1000	
S[cm^2]		1.73	
$I_{applied}$ [A/m^2]		0.58	
T_init [K]		298.15	
F[C/mol]		96,487	
R[J/K.mol]		8.314	
h [W/m^2.K]		4	

5.4 Results and Discussion

The temperature of operation is a key parameter in determining the performance and durability of solid polymer electrolyte for battery application. Controlling the temperature of the polymer electrolyte and its associated dynamic response is crucial for effective

design and better operations under different conditions. There are many factors that affect performance, ranging from fundamental thermodynamic properties; electronic, ionic, and mass transport mechanisms; heat transfer and electro-kinetics. Due to the complexity of the PEO/Lithium salt/GO semi crystalline system, a semi-empirical model is needed to predict the temperature dependencies on the battery performance. The temperature in this model affects mainly the Ohmic potential drop between the electrodes due to the change in the diffusivity and the resistivity of the electrolyte.

Raising the temperature of the PEO electrolyte with 1 wt% GO energizes the lithium-ions, causing them to move faster, and ultimately, increasing the ionic conductivity of the electrolyte. This relationship between temperature and ionic conductivity of PEO with 1 wt% GO is depicted in **Figure 5.2** and can be used to determine the electrolyte resistance at elevated temperatures in the mathematical model.

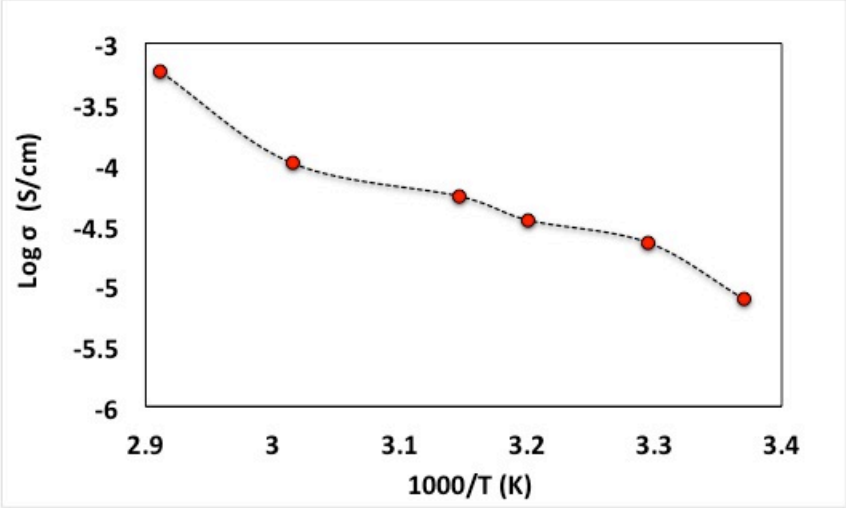

Figure 5-2: Temperature dependence of ion conductivity (1 wt% GO content)[79]

In addition to ionic conductivity, temperature has a profound effect on the capacity and the life of a lithium-ion battery. The effects of temperature in flexible lithium-ion

batteries made by two different solid polymer electrolytes have been investigated in the **Appendix D Figure 1.D**. The first type of the electrolyte is the pure poly (ethylene oxide) and second type is the nanocomposite polymer (PEO+ 1 wt %GO). It was previously discussed that the addition of 1 wt.% GO had a positive effect on the ionic conductivity of the polymer at room temperature and that enhancement is more relevant in the performance of the battery at high temperature. **Figure 5.3** plots the capacity vs. cycle for batteries operating at 25°C, 40°C, and 50°C. Although the cells at 50°C achieve much higher capacities than the batteries operating at 25°C and 40°C, peaking just over 1 mAh/cm^2, the elevated temperature is detrimental to battery life as the cells exhibit sever capacity fading. **Figure 5.3** also indicates that 40°C is an optimal operating temperature, with the batteries exhibiting stable performance through 50 cycles and achieving more than twice the capacity of the cells operating at 25°C. High temperatures yield higher capacities, but adversely affect the life of a battery while colder operating temperatures have the inverse effect of extending battery life, but also lowering the capacity of the LIB cells. Elevated temperature typically shortens the battery lifetime by increasing the rate of the degrading processes. In addition, large temperature gradients within the cell can lead to non-uniform current density and non-uniform aging phenomena.

The simulated versus experimental discharge curves with estimated parameters **α** and **h** are presented in **Figure 5.4**. This model defines end-of-discharge when the cell voltage drops below 2.8V. **Figure 5.4** demonstrates the good agreement between the predicted voltage vs. capacity using the theoretical model and the experimental results. At 50°C the maximum discharge capacity of 0.28 mAh/cm^2 is obtained for the current density of $0.057mA/cm^2$.

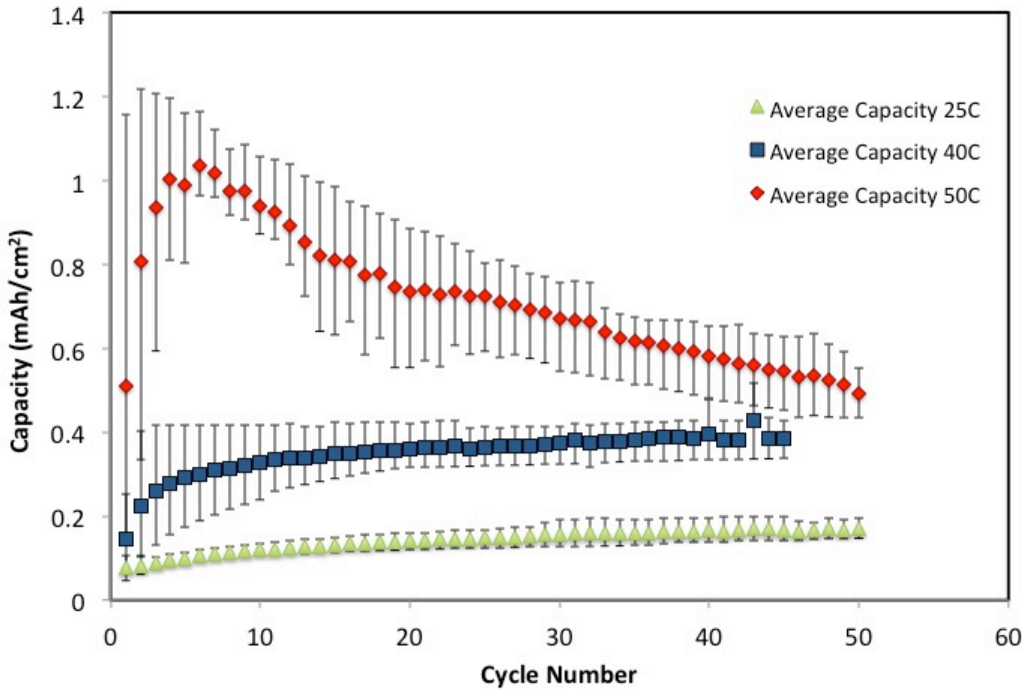

Figure 5-3: High Temperature cycling profile of the battery based on nanocomposite electrolyte (PEO+1 wt% GO) with plasticizer.

This agreement suggests that this model can be used to accurately determine the discharge capacity of the cell based on the solid polymer nanocomposite electrolyte at different temperatures and charging rates. As an example, the simulation can predict the first cycle discharge of a coin cell battery at T=30 °C (green). This model is general enough to include a wide range of polymeric electrolytes based on PEO/lithium salt and nanofiller. The potential drop between the electrodes is determined by varying the electrolyte resistance according to the Ohm's law, which greatly simplifies the numerical calculations. In addition, varying the physical properties of the electrolyte is permitted in this model. In fact, the value of the parameter $R_{electrolyte,}$ which is determined experimentally, is assumed to depend on the cell temperature and the electrolyte type.

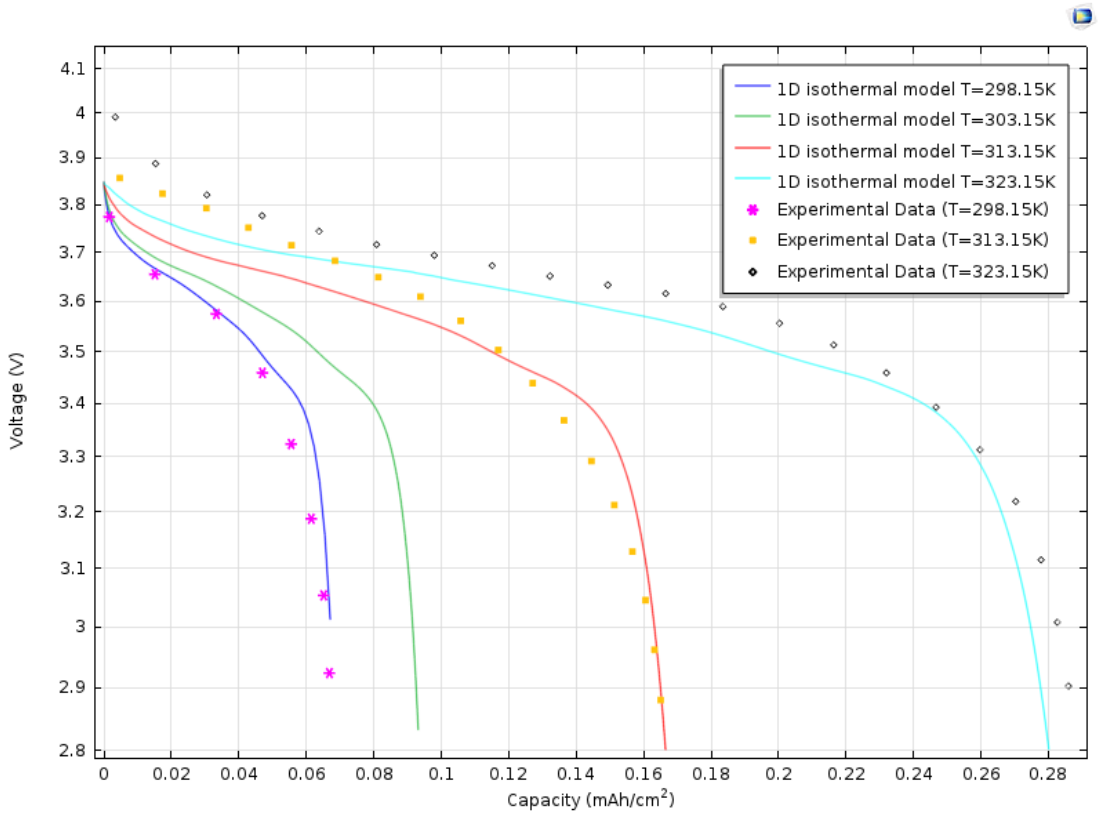

Figure 5-4: Comparison of the simulated results of the battery based on the nanocomposite electrolyte with the experimental data at different temperatures.

The mathematical model determines the first discharge behavior of the coin cell LIB for a given set of electrode materials and based on solid polymer nanocomposite electrolyte. Battery researchers can use the model to investigate the influence of various design parameters such as the choice of materials, dimensions, and the particle size of the active materials, in this case carbon on the negative electrode and $LiCoO_2$ on the positive electrode. Moreover, this model takes into consideration the effect of electrolyte resistance and dimensions on the battery performance. Another advantage of this simulation model is the benefit to predict battery performance under different operating conditions (i.e., external temperature and charging rate) to reduce the experimental work and cost.

However, the model presented in this work needs further improvements to simulate the cycling conditions for a full cell battery. Also, many of the model parameters have been experimentally determined or taken from the literature and some of the parameters have been estimated. Reducing the uncertainty in the estimated parameters will inevitably enhance the model's reliability and precision.

5.5 Conclusions

A mathematical model coupling heat transfer and battery discharge capacity was developed for a lithium-ion battery, based on the nanocomposite electrolyte. Batteries underwent 50 charge-discharge cycles at various operating temperatures (25°C, 40°C, 50°C) and showed that operating temperature significantly affects battery capacity. The batteries at high temperatures achieve higher capacities, but pronounced and rapid capacity fading while the batteries at low temperatures have low, but stable, capacities. These experimental results were used to validate the mathematical model.

The model presented in this work can only predict the capacity of the first cycle at different temperatures. However, the capacity fading of lithium-ion battery during high temperature operation after several cycles should be investigated and the model needs to be updated in future work.

Chapter 6: Conclusions and Future Work

6.1 Conclusions

6.1.1 Polymer Nanocomposite Electrolytes for Battery and Fuel Cell Applications

In this thesis, two types of polymer nanocomposite electrolytes were investigated for battery and fuel cell applications and discussed in Chapters 2. Specifically, we sought to improve upon the existing electrolyte technology for fuel cells by taking the novel approach of using a biomaterial nanofiller, specifically coconut shell activated carbon (AC), to improve fuel cell performance. Nafion composite electrolyte membranes were prepared using an evaporation-casting technique. The effect of varying filler content on the ionic conductivity and microstructure of the Nafion composite membranes was investigated via complex impedance spectroscopy and electron microscopy, respectively. Our experimental results show that the presence of AC filler increases water uptake of the membrane up to ~80 wt.% and, consequently, enhances proton conductivity by one order of magnitude without significantly compromising the mechanical properties of Nafion. Moreover, this study proposes a semi-empirical model of proton conductivity enhancement and degradation in the Nafion composite that includes the characteristics of the AC fillers. Ultimately, this model offers insight into the fundamental mechanisms of ion conductivity in the polymer-filler system and can be used to improve the design of Nafion PEMs.

A suitable solid polymer nanocomposite electrolyte for Li-ion batteries was also investigated. Graphene oxide based solid polymer nanocomposite electrolyte was

investigated for lithium-ion battery. Electrochemical, and thermal measurements were used to study this novel solid polymer electrolyte and compare it to the pure polymer.

The following conclusion statements can be made regarding the nanocomposite polymer:

- Adding a low content of GO can disrupt the ordered packing of semi-crystalline PEO chains and reduce the polymer crystallinity according to Morphological characterization of the pure PEO and PEO/1 wt% GO.
- Thermogravimetric analysis and flammability tests show that the prepared SPEs are thermally stable and they are revealing a nonflammable behavior compared to the commercial electrolyte (LiPF6-EC/DEC, 1:1 in volume).
- The composite electrolyte has a stable electrochemical window that extends the overall operating voltage of the cell to 4.2V.
- The ionic calculation at room temperature shows nearly one order of magnitude enhancement in ion conductivity (10^{-7} S/cm) compared to that of pure polymer electrolyte (10^{-8} S/cm).
- The PEO/GO polymer electrolyte shows a higher transference number compared to the pure PEO electrolyte

Based on these findings, nanocomposite SPEs pave the way for new forms of safer and more cost-effective energy storage devices capable of adapting to the stringent shape and space requirements of modern flexible and stretchable applications.

6.1.2 Polymer Based Flexible Battery

After demonstrating the enhanced properties of the nanocomposite PEO electrolyte, the effect of GO nanofillers, in the PEO polymer matrix, on the mechanical and

electrochemical performance of flexible lithium ion batteries was investigated and discussed in Chapter 3. The nanocomposite electrolyte batteries showed enhanced charge-discharge capacities and less capacity fading when compared to the batteries with pure PEO electrolytes. Furthermore, mechanical bending tests of the flexible batteries revealed that the nanocomposite electrolyte battery systems exhibited higher voltage retention under cyclic loading conditions. Finally, a finite element analysis of the flexible battery under an applied bending load revealed that a the enhanced electrochemical performance of the robust, laminated, thin-film, flexible battery is a result of the combination of the compressive stresses during lamination and increased electrode-electrolyte contact during bending.

6.1.3 Polymer based Spiral Stretchable Battery

The nanocomposite PEO electrolyte was also implemented into a spiral-shaped battery and presented in Chapter 4. The spring-like design of this battery is capable of large out-of-plane deformation of 1300 % while exhibiting simultaneous electrochemical functionality. The experimental results show the acceptable electrochemical performance of the spiral battery and its ability to function over large deformation distances. The spiral lithium ion battery exhibits robust mechanical stretchability over 9000 stretching cycles and an energy density of 4.862 mWh/cm^3 at ~ 650 % out-of-plane deformation. Finite element analysis of the spiral battery offers insights about the nature of stresses and strains during battery stretching.

6.1.4 Modeling and Simulations

A single-particle mathematical model was developed to include the effect of the

external temperature on the capacity of the nanocomposite electrolyte based battery. The temperature effect was accounted for in the ohmic potential drop within the electrode due to the change in the diffusivity and the resistivity of the electrolyte.

The model shows good agreement with the experimental data at constant charging/discharging rates and at different temperatures and can be adopted to predict the electrochemical performance of various electrolyte material LIB systems. For instance, the maximum discharge capacity of 0.28 mAh/cm^2 is achieved at 50ºC, which is 3 times higher than the discharge capacity at 25ºC (0.07 mAh/cm^2) at the same current density of 0.057mA/cm^2. Finally, the simulation was used to predict the first discharge cycle with a capacity of 0.095 mAh/cm^2 for a coin cell battery based on solid polymer nanocomposite electrolyte at T=30°C.

6.2 Future Work

6.2.1 Enhancement of the Ionic Conductivity Model for the Nafion/AC Electrolyte

The derived model in Chapter 2 provides insight into the effects of AC nanofillers on ionic conductivity. The model shows a good fit to experimental data and sheds light onto the characteristics, load, and structure of the filler particles that impacts the ionic conduction and water sorption of the proton exchange membrane. However, this is a descriptive model and requires more information to further understand the mechanism of the nanofiller-induced enhancement of ionic conductivity.

6.2.2 Enhancement of the Properties for the Solid Polymer Electrolyte and the Performance of the Flexible and Spiral LIBs

Although the GO nanofillers showed improved performance of PEO electrolytes, further work is needed to address some of the adverse effects that GO can have polymer electrolyte performance, namely the aggregation of the graphene oxide sheets. Previous studies have shown that a high concentration of graphene oxide inhibits ion transport through the polymer matrix due to the aggregation of fillers. An alternative fabrication process of the polymer membrane is needed to better disperse the filler and minimize aggregation.

Moreover, an improved and well-controlled polymer electrolyte fabrication method, possibly requiring more sophisticated equipment, is needed to create freestanding membranes with a uniform thickness. This will minimize variation in the experimental results of the polymer electrolyte and bring about enhanced and repeatable performance of flexible and spiral LIBs.

Further improvement of the solid-state flexible and spiral LIBs lies in complete removal of liquid electrolyte needed to enhance the electrode-electrolyte interface resistance. Adding liquid to the polymer electrolyte based batteries brings up issues of SEI formation and capacity fading.

However, for solid polymer electrolytes, low ionic conductivity is still an enormous barrier to overcome to be compatible with high-energy battery applications. Alternative electrolyte options, such as gel polymers and ceramics, with enhanced mechanical

properties need to be explored.

The fabrication process for developing flexible and spiral batteries needs to be improved to achieve a reliable and flexible seal. A hermetic seal is necessary to protect the batteries from the external environment, moisture penetration, and oxidation of the battery components, which directly affects the capacity and life of the LIB.

Finally, another approach can be employed to improve the mechanical flexibility of spiral and flexible LIBs. It is the investigation of new designs and materials for the electrodes to make them more stretchable, flexible and compatible with solid electrolytes.

6.2.3 Improvement of the Simulation Model

The model presented in this work needs further improvements to simulate the cycling conditions for a full cell battery. Furthermore, the estimated and corrected variables used in the mathematical model need to be experimentally verified in future studies. This will inevitably affect the fit of the model to the experimental data and model alterations may be required. Ultimately, an accurate model will reduce experimental costs and efforts, aid in the intelligent design of batteries to be suitable for their specific applications, and provide a deeper understanding of the battery behavior.

References

[1] U. S. E. I. Administration. "International Energy Statistics," http://www.eia.gov/.

[2] J. Hansen, and M. Sato, "Greenhouse Gas Growth Rates," *PNAS* vol. 101, pp. 16109–16114, 2004.

[3] D. Pimentel, M. Herz, M. Glickstein, M. Zimmerman, R. Allen, K. Becker, J. Evans, B. Hussain, R. Sarsfeld, A. Grosfeld, and T. Seidel, "Renewable Energy: Current and Potential Issues," *BioScience,* vol. 52, pp. 1111-1120, 2002.

[4] J. B. Goodenough, and Y. Kim, "Challenges for Rechargeable Li Batteries," *Chemistry of Materials,* vol. 22, no. 3, pp. 587-603, 2010.

[5] J. B. Goodenough, "Rechargeable Batteries: Challenges Old and New," *Journal of Solid State Electrochemistry,* vol. 16, no. 6, pp. 2019-2029, 2012.

[6] J.-M. Tarascon, and M. Armadi, "Issue and Challenges Facing Rechargeable Lithium Batteries," *Nature,* vol. 414, pp. 359-367, 2001.

[7] B. E. Conway, *Electrochemical Supercapacitors: Scientific Fundamentals and Technological Applications* New York, 1999.

[8] P. Simon, and Y. Gogotsi, "Materials for Electrochemical Capacitors," *Nature materials* vol. 7, pp. 845-854, 2008.

[9] M. Winter, and R. J. Brodd, "What Are Batteries, Fuel Cells, and Supercapacitors?," *Chem. Rev.,* vol. 104, pp. 4245–4269, 2004.

[10] M. C. Rao, "Cathode Materials for Solid State Microbatteries-A Case Study," *Research Journal of Chemical Sciences,* vol. 2(3), pp. 74-79, 2012.

[11] B. Scrosati, "Recent Advances in Lithium Ion Battery Materials,"

Electrochimica Acta vol. 45, pp. 2461–2466, 2000.

[12] N. Nitta, F. Wu, J. T. Lee, and G. Yushin, "Li-Ion Battery Materials: Present and Future," *Materials Today,* vol. 18, no. 5, pp. 252-264, 2015.

[13] P. Arora, and Z. J. Zhang, "Battery Separators," *Chem. Rev.,* vol. 104, pp. 4419-4462, 2004.

[14] M. Yang, and J. Hou, "Membranes in Lithium Ion Batteries," *Membranes (Basel),* vol. 2, no. 3, pp. 367-83, Jul 04, 2012.

[15] M.Winter, and R. J. Brodd, "What Are Batteries, Fuel Cells, and Supercapacitors?," *Chem. Rev.,* vol. 104, pp. 4245–4269, 2004.

[16] J.-I. Yamaki, S.-I. Tobishima, K. Hayashi, K. Saito, Y. Nemoto, and M. Arakawa, "A Consideration of the Morphology of Electrochemically Deposited Lithium in an Organic Electrolyte," *Journal of Power Sources* vol. 74, pp. 219–227, 1998.

[17] M. M. Thackeray, W. I. F. David, P. G. Bruce, and J. B. Goodenough, "Lithium Inserstion Into Manganese Spinels," *Mat. Res. Bull,* vol. 18, pp. 461-472, 1983.

[18] K. C. Kam, and M. M. Doeff, "Electrode Materials for Lithium Ion Batteries," *Material Matters,* vol. 7, pp. 56-60, 2012.

[19] Q. Li, J. Chen, L. Fan, X. Kong, and Y. Lu, "Progress in Electrolytes for Rechargeable Li-Based Batteries and Beyond," *Green Energy & Environment,* vol. 1, no. 1, pp. 18-42, 2016.

[20] J. A. Rogers, T. Someya, and Y. Huang, "Materials and Mechanics for Stretchable Electronics," *Science,* vol. 327, no. 5973, pp. 1603-7, Mar 26, 2010.

[21] L. Li, Z. Wu, S. Yuan, and X. B. Zhang, "Advances and Challenges for Flexible Energy Storage and Conversion Devices And Systems," *Energy & Environmental Science,* vol. 7, no. 7, pp. 2101, 2014.

[22] G. Zhou, F. Li, and H.-M. Cheng, "Progress in Flexible Lithium Batteries and Future Prospects," *Energy Environ. Sci.,* vol. 7, no. 4, pp. 1307-1338, 2014.

[23] K. Xie, and B. Wei, "Materials and Structures for Stretchable Energy Storage and Conversion Devices," *Adv Mater,* vol. 26, no. 22, pp. 3592-617, Jun 11, 2014.

[24] L. Hu, H. Wu, F. L. Mantia, Y. Yang, and Y. Cui, "Thin, Flexible Secondary Li-Ion Paper Batteries," *ACS Nano,* vol. 4, pp. 5843–5848, 2010.

[25] L. Hu, M. Pasta, F. L. Mantia, L. Cui, S. Jeong, H. D. Deshazer, J. W. Choi, S. M. Han, and Y. Cui, "Stretchable, Porous, and Conductive Energy Textiles," *Nano Lett,* vol. 10, no. 2, pp. 708-14, Feb 10, 2010.

[26] J. F. M. Oudenhoven, L. Baggetto, and P. H. L. Notten, "All-Solid-State Lithium-Ion Microbatteries: A Review of Various Three-Dimensional Concepts," *Advanced Energy Materials,* vol. 1, no. 1, pp. 10-33, 2011.

[27] C. K. Chan, H. Peng, G. Liu, K. McIlwrath, X. F. Zhang, R. A. Huggins, and Y. Cui, "High-Performance Lithium Battery Anodes using Silicon Nanowires," *Nat Nanotechnol,* vol. 3, no. 1, pp. 31-36, Jan, 2008.

[28] D. Wang, R. Kou, D. Choi, Z. Yang, Z. Nie, J. Li, L. V. Saraf, D. Hu, J. Zhang, G. L. Graff, J. Liu, M. A. Pope, and I. A. Aksay, "Ternary Self-Assembly of Ordered Metal Oxide-Graphene Nanocomposites for Electrochemical Energy Storage," *Acs Nano,* vol. 4, pp. 1587–1595 2010.

[29] L. Fu, K. Tang, C.-C. Chen, L. Liu, X. Guo, Y. Yu, and J. Maier, "Free-Standing Ag/C Coaxial Hybrid Electrodes as Anodes for Li-Ion Batteries," *Nanoscale,* vol. 5, no. 23, pp. 11568-11571, Dec 7, 2013.

[30] R. S. Morris, B. G. Dixon, T. Gennett, R. Raffaelle, and M. J. Heben, "High-Energy, Rechargeable Li-Ion Battery Based on Carbon Nanotube Technology," *Journal of Power Sources,* vol. 138, no. 1-2, pp. 277-280, 2004.

[31] B. J. Landi, M. J. Ganter, C. M. Schauerman, C. D. Cress, and R. P. Raffaelle, "Lithium Ion Capacity of Single Wall Carbon Nanotube Paper Electrodes," *J. Phys. Chem.C,* vol. 112, pp. 7509-7515, 2008.

[32] S. H. Ng, J. Wang, Z. P. Guo, J. Chen, G. X. Wang, and H. K. Liu, "Single Wall Carbon Nanotube Paper as Anode for Lithium-Ion Battery," *Electrochimica Acta,* vol. 51, no. 1, pp. 23-28, 2005.

[33] N. Mahmood, C. Zhang, H. Yin, and Y. Hou, "Graphene-Based Nanocomposites for Energy Storage and Conversion in Lithium Batteries, Supercapacitors and Fuel Cells," *Journal of Materials Chemistry A,* vol. 2, no. 1, pp. 15-32, 2014.

[34] S. Li, Y. Luo, W. Lv, W. Yu, S. Wu, P. Hou, Q. Yang, Q. Meng, C. Liu, and H. M. Cheng, "Vertically Aligned Carbon Nanotubes Grown on Graphene Paper as Electrodes in Lithium-Ion Batteries and Dye-Sensitized Solar Cells," *Advanced Energy Materials,* vol. 1, no. 4, pp. 486-490, 2011.

[35] M. Zhou, F. .Pu, Z. Wang, T. Cai, H. Chen, H. Zhang, and S. .Guan, "Facile Synthesis of Novel Si Nanoparticles-Graphene Composites as High-Performance Anode Materials for Li-Ion Batteries," *Phys Chem Chem Phys,* vol. 15, no. 27, pp. 11394-11401, Jul 21, 2013.

[36] K. Wang, S. Luo, Y. Wu, X. He, F. Zhao, J. Wang, K. Jiang, and S. Fan, "Super-Aligned Carbon Nanotube Films as Current Collectors for Lightweight and Flexible Lithium Ion Batteries," *Advanced Functional Materials,* vol. 23, no. 7, pp. 846-853, 2013.

[37] F. B. Dias, L. Plomp, and J. B. J. Veldhuis, "Trends in Polymer Electrolytes for Secondary Lithium Batteries," *Journal of Power Sources,* vol. 88, pp. 169–191, 2000.

[38] R. C. Agrawal, and G. P. Pandey, "Solid Polymer Electrolytes: Materials Designing and All-Solid-State Battery Applications: An Overview," *Journal of Physics D: Applied Physics,* vol. 41, no. 22, pp. 223001-223019, 2008.

[39] C. A. Nguyen, S. Xiong, J. Ma, X. Lu, and P. S. Lee, "High Ionic Conductivity P(Vdf-Trfe)/Peo Blended Polymer Electrolytes for Solid Electrochromic Devices," *Phys Chem Chem Phys,* vol. 13, no. 29, pp. 13319-13345, Aug 7, 2011.

[40] F. Croce, G. B. Appetecchi, L. Persi, and B. Scrosati, "Nanocomposite Polymer Electrolytes for Lithium Batteries," *Nature,* vol. 394, pp. 456-458, 1998.

[41] L. Y. Yang, D. X. Wei, M. Xu, Y. F. Yao, and Q. Chen, "Transferring Lithium Ions In Nanochannels: A PEO/Li(+) Solid Polymer Electrolyte Design," *Angew Chem Int Ed Engl,* vol. 53, no. 14, pp. 3705-3709, Apr 1, 2014.

[42] M. S. Michael, M. M. E. Jacob, S. R. S. Prabaharan, and S. Radhakrishna, "Enhanced Lithium Ion Transport in Peo-Based Solid Polymer Electrolytes Employing a Novel Class Of Plasticizers," *Solid State Ionics,* vol. 98, pp. 167–174, 1997.

[43] N. Karan, D. Pradhan, R. Thomas, B. Natesan, and R. Katiyar, "Solid Polymer Electrolytes Based on Polyethylene Oxide and Lithium Trifluoro- Methane Sulfonate (Peo–Licf3So3): Ionic Conductivity and Dielectric Relaxation," *Solid State Ionics,* vol. 179, no. 19-20, pp. 689-696, 2008.

[44] S. K. Fullerton-Shirey, and J. K. Maranas, "Effect of LiClO4 on the Structure and Mobility of PEO-Based Solid Polymer Electrolytes," *Macromolecules,* vol. 42, pp. 2142-2156, 2009.

[45] E. Quartarone, and P. Mustarelli, "Electrolytes for Solid-State Lithium Rechargeable Batteries: Recent Advances and Perspectives," *Chem Soc Rev,* vol. 40, no. 5, pp. 2525-40, May, 2011.

[46] M. Doyle, T. F. Fuller, and J. Newman, "Modeling of Galvanostatic Charge and Discharge of the Lithium/Polymer/Insertion Cell," *J. Electrochem. Soc.,* vol. 140, pp. 1526-1533, 1993.

[47] L. Cai, and R. E. White, "Mathematical Modeling of a Lithium Ion Battery with Thermal Effects in Comsol Inc. Multiphysics (MP) Software," *Journal of Power Sources,* vol. 196, no. 14, pp. 5985-5989, 2011.

[48] Y. Ye, Y. Shi, N. Cai, J. Lee, and X. He, "Electro-Thermal Modeling and Experimental Validation for Lithium Ion Battery," *Journal of Power Sources,* vol. 199, pp. 227-238, 2012.

[49] V. Ramadesigan, P. W. C. Northrop, S. De, S. Santhanagopalan, R. D. Braatz, and V. R. Subramanian, "Modeling and Simulation of Lithium-Ion Batteries from a Systems Engineering Perspective," *Journal of the Electrochemical Society,* vol. 159, no. 3, pp. R31-R45, 2012.

[50] P. G. Bruce, J. Evans, and C. A. Vincent, "Conductivity and Transference Number Measurements on Polymer Electrolytes," *Solid State Ionics,* vol. 28, pp. 918-922, 1988.

[51] K. Karuppasamy, R. Antony, S. Alwin, S. Balakumar, and X. S. Shajan, "A Review on PEO Based Solid Polymer Electrolytes (SPEs) Complexed with LiX (X=Tf, BOB) for Rechargeable Lithium Ion Batteries," *Materials Science Forum,* vol. 807, pp. 41-63, 2014.

[52] D. E. Fenton, J. M. Parker, and P. V. Wright, "Complexes of Alkali Metal Ions with Poly(Ethylene Oxide) " *Polymer,* vol. 14, pp. 589-589, 1973.

[53] P. Vashishta, J. N. Mundy, and G. K. Shenoy, *Fast Ion Transport in Solids: Electrodes, and Electrolytes*, Lake Geneva, Wisconsin, U.S.A: North Holland, 1979.

[54] Y. Yamada, and A. Yamada, "Review—Superconcentrated Electrolytes for Lithium Batteries," *Journal of The Electrochemical Society,* vol. 162, no. 14, pp. A2406-A2423, 2015.

[55] D. T. Hallinan, and N. P. Balsara, "Polymer Electrolytes," *Annual Review of Materials Research,* vol. 43, no. 1, pp. 503-525, 2013.

[56] S. Stramare, V. Thangadurai, and W. Weppner, "Lithium Lanthanum Titanates: A Review," *Chem. Mater.,* vol. 15, pp. 3974-3990, 2003.

[57] J. M. Zielinski, and J. L. Duda, "Predicting Polymer/Solvent Diffusion Coefficients using Free-Volume Theory," *AIChE,* vol. 38, pp. 405-4015, 1992.

[58] M. H. Cohen, and D. Turnbull, "Molecular Transport in Liquids and Glasses," *The Journal of Chemical Physics,* vol. 31, no. 5, pp. 1164-1169, 1959.

[59] D. Golodnitsky, E. Strauss, E. Peled, and S. Greenbaum, "Review—On Order and Disorder in Polymer Electrolytes," *Journal of The Electrochemical Society,* vol. 162, no. 14, pp. A2551-A2566, 2015.

[60] X. Q. Yang, H. S. .Lee, L. Hanson, J. McBreen, and Y. Okamoto, "Development of a New Plasticizer for Poly(Ethylene Oxide)-Based Polymer Electrolyte and the Investigation of their Ion-Pair Dissociation Effect," *Journal of Power Sources,* vol. 54, pp. 198--204, 1995.

[61] Y. Kumar, S. A. Hashmi, and G. P. Pandey, "Lithium Ion Transport and Ion–Polymer Interaction in Peo Based Polymer Electrolyte Plasticized with Ionic Liquid," *Solid State Ionics,* vol. 201, no. 1, pp. 73-80, 2011.

[62] A. M. Stephan, and K. S. Nahm, "Review on Composite Polymer Electrolytes for Lithium Batteries," *Polymer,* vol. 47, no. 16, pp. 5952-5964, 2006.

[63] Z. Jia, W. Yuan, H. Zhao, H. Hu, and G. L. Baker, "Composite Electrolytes Comprised of Poly(Ethylene Oxide) and Silica Nanoparticles with Grafted Poly(Ethylene Oxide)-Containing Polymers," *RSC Adv.,* vol. 4, no. 77, pp. 41087-41098, 2014.

[64] F. Croce, F. Bonino, S. Panero, and B. Scrosati, "Properties of Mixed Polymer and Crystalline Ionic Conductors," *Philosophical Magazine B-Physics of Condensed Matter Statistical Mechanics Electronic Optical and Magnetic Properties,* vol. 59, pp. 161-168, 1989.

[65] G. B. Appetecchi, F. Croce, J. Hassoun, B. Scrosati, M. Salomon, and F. Cassel, "Hot-Pressed, Dry, Composite, Peo-Based Electrolyte Membranes," *Journal of Power Sources,* vol. 114, no. 1, pp. 105-112, 2003.

[66] F. Capuano, F. Croce, and B. Scrosati, "Composite Polymer Electrolytes," *J. Electrochem. Soc.,* vol. 138, no. 1918-1922, 1991.

[67] B. Scrosati, F. Croce, and L. Persi, "Impedance Spectroscopy Study of PEO-Based Nanocomposite Polymer Electrolytes," *Journal of The Electrochemical Society,* vol. 147 (5) pp. 1718-1721 2000.

[68] S. J. Peighambardoust, S. Rowshanzamir, and M. Amjadi, "Review of the Proton Exchange Membranes for Fuel Cell Applications," *international journal of hydrogen energy* vol. 35, pp. 9349-9384, 2010.

[69] K. A. Mauritz, and R. B. Moore, "State of Understanding of Nafion," *Chem. Rev,* vol. 104, pp. 4535–4585, 2004.

[70] G. Gebel, "Structural Evolution of Water Swollen Perfluorosulfonated Ionomers from Dry Membrane To Solution," *Polymer,* vol. 41, pp. 5829–5838, 2000.

[71] Y. F. Zhang, S. J. Wang, M. Xiao, S. G.Bian, and Y. Z. Meng, "The Silica-Doped Sulfonated Poly(Fluorenyl Ether Ketone)s Membrane using Hydroxypropyl Methyl Cellulose as Dispersant for High Temperature Proton Exchange Membrane Fuel Cells," *international journal of hydrogen energy,* vol. 34, pp. 4379–4386, 2009.

[72] M. A. Navarra, F. Croce, and B. Scrosati, "New, High Temperature Superacid Zirconia-Doped Nafion™ Composite Membranes," *Journal of Materials Chemistry,* vol. 17, no. 30, pp. 3210, 2007.

[73] A. S. Aricò, P. Bruce, B. Scrosati, J.-M. Tarascon, and W. V. Schalkwijk, "Nanostructured Materials For Advanced Energy Conversion And Storage

Devices," *Nature Materials,* vol. 4, pp. 366-377, 2005.

[74] C. H. Rhee, H. K. Kim, H. Chang, and J. S. Lee, "Nafion/Sulfonated Montmorillonite Composite: A New Concept Electrolyte Membrane for Direct Methanol Fuel Cells," *Chem. Mater.,* vol. 17, pp. 1691-1697, 2005.

[75] G. Alberti, and M. Casciola, "Compositemembranes Formedium-Temperaturepem Fuelcells," *Annual Review of Materials Research,* vol. 33, no. 1, pp. 129-154, 2003.

[76] Z. Chen, B. Holmberg, W. Li, X. Wang, W. Deng, R. Munoz, and Y. Yan, "Nafion/Zeolite Nanocomposite Membrane by in Situ Crystallization for a Direct Methanol Fuel Cell," *Chem. Mater.,* vol. 18, pp. 5669-5675, 2006.

[77] V. Tricoli, and F. Nannetti, "Zeolite–Nafion Composites as Ion Conducting Membrane Materials," *Electrochimica Acta,* vol. 48, no. 18, pp. 2625-2633, 2003.

[78] R. Devanathan, "Recent Developments in Proton Exchange Membranes for Fuel Cells," *Energy & Environmental Science,* vol. 1, no. 1, pp. 101, 2008.

[79] M. Yuan, J. Erdman, C. Tang, and H. Ardebili, "High Performance Solid Polymer Electrolyte with Graphene Oxide Nanosheets," *RSC Adv.,* vol. 4, no. 103, pp. 59637-59642, 2014.

[80] J. Shim, D.-G. Kim, H. J. Kim, J. H. Lee, J.-H. Baika, and J.-C. Lee, "Novel Composite Polymer Electrolytes Containing Poly(Ethylene Glycol)-Grafted Graphene Oxide for All-Solid-State Lithium-Ion Battery Applications," *J. Mater. Chem. A,* vol. 2, pp. 13873-13883, 2014.

[81] S. Gao, J. Zhong, G. Xue, and B. Wang, "Ion Conductivity Improved

Polyethylene Oxide/Lithium Perchlorate Electrolyte Membranes Modified By Graphene Oxide," *Journal of Membrane Science,* vol. 470, pp. 316-322, 2014.

[82] M. S. Akhtar, S. Kwon, F. J. Stadler, and O. B. Yang, "High Efficiency Solid State Dye Sensitized Solar Cells with Graphene-Polyethylene Oxide Composite Electrolytes," *Nanoscale,* vol. 5, no. 12, pp. 5403-5414, Jun 21, 2013.

[83] R. Yang, S. Zhang, L. Zhang, and W. Liu, "Electrical Properties of Composite Polymer Electrolytes Based on Peo-Sn-Licf3So3.," *Int. J. Electrochem. Sci.,* vol. 8, pp. 10163-10169, 2013.

[84] X.-W. Zhang, C. Wanga, A. J. Applebya, and F. E. Little, "Characteristics of Lithium-Ion-Conducting Composite Polymer-Glass Secondary Cell Electrolytes," *Journal of Power Sources* vol. 112, pp. 209–215, 2002.

[85] A. M. Herring, "Inorganic–Polymer Composite Membranes for Proton Exchange Membrane Fuel Cells," *Journal of Macromolecular Science, Part C: Polymer Reviews,* vol. 46, no. 3, pp. 245-296, 2006.

[86] J. Rozière, and D. J. Jones, "Non-Fluorinatedpolymermaterials For Proton Exchange Membrane Fuel Cells," *Annual Review of Materials Research,* vol. 33, no. 1, pp. 503-555, 2003.

[87] N. P. Cele, S. S. Ray, S. K. Pillai, M. Ndwandwe, S. Nonjola, L. Sikhwivhilu, and M. K. Mathe, "Carbon Nanotubes Based Nafion Composite Membranes for Fuel Cell Applications," *Fuel Cells,* vol. 0, pp. 1–8, 2009.

[88] H. Teng, "Overview of the Development Of The Fluoropolymer Industry," *Applied Sciences,* vol. 2, no. 4, pp. 496-512, 2012.

[89] C. Sanchez, B. Julián, P. Belleville, and M. Popall, "Applications of Hybrid

Organic–Inorganic Nanocomposites," *Journal of Materials Chemistry,* vol. 15, no. 35-36, pp. 3559, 2005.

[90] P. Y. Chen, C. P. Chiu, and C. W. Hong, "Molecular Structure and Transport Dynamics in Nafion and Sulfonated Poly(Ether Ether Ketone Ketone) Membranes," *Journal of Power Sources,* vol. 194, no. 2, pp. 746-752, 2009.

[91] H.-C. Chien, L.-D. Tsai, C.-M. Lai, J.-N. Lin, C.-Y. Zhu, and F.-C. Chang, "Characteristics of High-Water-Uptake Activated Carbon/Nafion Hybrid Membranes for Proton Exchange Membrane Fuel Cells," *Journal of Power Sources,* vol. 226, pp. 87-93, 2013.

[92] P. W. Majsztrik, M. B. Satterfield, A. B. Bocarsly, and J. B. Benziger, "Water Sorption, Desorption and Transport in Nafion Membranes," *Journal of Membrane Science,* vol. 301, no. 1-2, pp. 93-106, 2007.

[93] J. Lee, C.-W. Yi, and K. Kim, "The Electrochemical Properties of the Porous Nafion Membrane for Proton Exchange Membrane Fuel Cells (PEMFCs)," *Bulletin of the Korean Chemical Society,* vol. 33, no. 5, pp. 1788-1790, 2012.

[94] F. Liu, B. Yi, D. Xing, J. Yu, and H. Zhang, "Nafion/Ptfe Composite Membranes for Fuel Cell Applications," *Journal of Membrane Science,* vol. 212, pp. 213–223, 2003.

[95] T. A. Zawodzinski, J. C. Derouin, S. Radzinski, R. J. Sherman, V. T. Smith, T. E. Springer, and S. Gottesfeld, "Water Uptake by and Transport Through Nation 117 Membranes," *J. Electrochem. Soc.,* vol. 140, pp. 1041-1047, 1993.

[96] A. G. Kannan, N. R. Choudhury, and N. K. Dutta, "In Situ Modification Of Nafion® Membranes With Phospho-Silicate For Improved Water Retention

And Proton Conduction," *Journal of Membrane Science,* vol. 333, no. 1-2, pp. 50-58, 2009.

[97] A. K. Sahu, A. Jalajakshi, S. Pitchumani, P. Sridhar, and A. K. Shukla, "Endurance Of Nafion-Composite Membranes In Pefcs Operating At Elevated Temperature Under Low Relative-Humidity," *J. Chem. Sci.,* vol. 124, pp. 529–536., 2012.

[98] I. Cabasso, and Z.-Z. Liu, "The Permselectivity of Ion-Exchange Membranes for Non-Electrolyte Liquid Mixtures I. Separation of Alcohol/Water Mixtures with Nafion Hollow Fibers," *Journal of Membrane Science,* vol. 24, pp. 101-119, 1985.

[99] V. Ijeri, C. Lucandrea, S. Bianco, M. Tortello, P. Spinelli, and E. Tresso, "Nafion and Carbon Nanotube Nanocomposites for Mixed Proton and Electron Conduction," *Journal of Membrane Science,* vol. 363, no. 1-2, pp. 265-270, 2010.

[100] A. Saccà, A. Carbone, R. Pedicini, G. Portale, L. D'Ilario, A. Longo, A. Martorana, and E. Passalacqua, "Structural And Electrochemical Investigation On Re-Cast Nafion Membranes For Polymer Electrolyte Fuel Cells (Pefcs) Application," *Journal of Membrane Science,* vol. 278, no. 1-2, pp. 105-113, 2006.

[101] J.-M. Thomassin, J. Kollar, C. Giuseppe, A. Germain, R. Jérôme, and C. Detrembleur, "Beneficial Effect of Carbon Nanotubes on the Performances of Nafion Membranes in Fuel Cell Applications," *Journal of Membrane Science,* vol. 303, no. 1-2, pp. 252-257, 2007.

[102] M. Kammoun, L. Lundquist, and H. Ardebili, "High Proton Conductivity

Membrane with Coconut Shell Activated Carbon," *Ionics,* vol. 21, no. 6, pp. 1665-1674, 2014.

[103] M. Matsuyama, E. Kokufuta, T. Kusumi, and K. Harada, "Ion Percolation and Insulator-to-Conductor Transition in Nafion' Perfluorosulfonic Acid Membranes," *Macromolecules,* vol. 13, pp. 198-200, 1980.

[104] Y. Zhen, P. Xiaofeng, W. Buxuan, L. Duujong, and D. Yuanyuan, "Modeling of Ion Conductivity in Nafion Membranes," *Frontiers of Energy and Power Engineering in China,* vol. 1, no. 1, pp. 58-66, 2007.

[105] J. Y. Li, and S. N. Nasser, "Micromechanical Analysis of Ionic Clustering in Nafion Per¯Uorinated Membrane," *Mechanics of Materials,* vol. 32, pp. 303-314, 2000.

[106] C. Yang, S. Srinivasan, A. B. Bocarsly, S. Tulyani, and J. B. Benziger, "A Comparison of Physical Properties and Fuel Cell Performance of Nafion and Zirconium Phosphate/Nafion Composite Membranes," *Journal of Membrane Science,* vol. 237, no. 1-2, pp. 145-161, 2004.

[107] Q. Li, E. Wood, and H. Ardebili, "Elucidating the Mechanisms of Ion Conductivity Enhancement in Polymer Nanocomposite Electrolytes for Lithium Ion Batteries," *Applied Physics Letters,* vol. 102, no. 24, pp. 243903, 2013.

[108] R. B. Lartey, F. Acquah, and K. S. Nketia, "Developing National Capability for Manufacture of Activated Carbon from Agricultural Wastes," *The Ghana Engineer*, 1999.

[109] C. C. Incorporated, *Activated Carbon Manufacture, Structure & Properties*,

2006.

[110] J. K. Brennan, K. T. Thomson, and K. E. Gubbins, “Adsorption of Water in Activated Carbons: Effects of Pore Blocking and Connectivity,” *Langmuir,* vol. 18, pp. 5438-5447, 2002.

[111] I. U. R. Nanomaterials, "Inc. US Research Nanomaterials. ," US Research Nanomaterials, Inc.

[112] H.-L. Lin, T. L. Yu, C.-H. Huang, and T.-L. Lin, “Morphology Study of Nafion Membranes Prepared by Solutions Casting,” *Journal of Polymer Science Part B: Polymer Physics,* vol. 43, no. 21, pp. 3044-3057, 2005.

[113] P. M. Gomadam, and J. W. Weidner, “Analysis of Electrochemical Impedance Spectroscopy in Proton Exchange Membrane Fuel Cells,” *International Journal of Energy Research,* vol. 29, no. 12, pp. 1133-1151, 2005.

[114] Y. F. Huang, L. C. Chuang, A. M. Kannan, and C. W. Lin, “Proton-Conducting Membranes with High Selectivity from Cross-Linked Poly(Vinyl Alcohol) and Poly(Vinyl Pyrrolidone) for Direct Methanol Fuel Cell Applications,” *Journal of Power Sources,* vol. 186, no. 1, pp. 22-28, 2009.

[115] S. Hink, N. Wagner, W. G. Bessler, and E. Roduner, “Impedance Spectroscopic Investigation of Proton Conductivity in Nafion Using Transient Electrochemical Atomic Force Microscopy (AFM),” *Membranes (Basel),* vol. 2, no. 2, pp. 237-52, 2012.

[116] R. F. Silva, M. D. Francesco, and A. Pozio, “Solution-Cast Nafion® Ionomer Membranes: Preparation and Characterization,” *Electrochimica Acta,* vol. 49, pp. 3211–3219, 2004.

[117] Y. Kawano, Y. Wang, R. A. Palmer, and S. R. Aubuchon, “Stress-Strain Curves of Nafion Membranes in Acid and Salt Forms,” *Ciência e Tecnologia,* vol. 12, pp. 96-101, 2002.

[118] C.-H. Ma, T. L. Yu, H. L. Lin, Y.-T. Huang, Y.-L. Chen, U.-S.Jeng, Y.-H. Lai, and Y.-S. Sun, “Morphology and Properties of Nafion Membranes Prepared by Solution Casting,” *Polymer* vol. 50, pp. 1764–1777, 2009.

[119] S. Kundu, L. C. Simon, M. Fowler, and S. Grot, “Mechanical Properties Of Nafion™ Electrolyte Membranes under Hydrated Conditions,” *Polymer,* vol. 46, no. 25, pp. 11707-11715, 2005.

[120] D. F. Cells, "DuPont Nafion® PFSA Membranes," D. Pont, ed., 2009.

[121] E. A. Muller, and K. E. Gubbins, “Molecular Simulation Study of Hydrophilic and Hydrophobic Behavior of Activated Carbon Surfaces,” *Carbon* vol. 36, pp. 1433–1438, 1998.

[122] T. Sakai, H. Takenako, N. Wakabayashi, Y. Kawami, and E. Torikai, “Gas Permeation Properties of Solid PolymerElectrolyte(SPE) Membranes,” *J. Electrochem. Soc.,* vol. 132, pp. 1328-1332, 1985.

[123] F. N. Buchi, and G. G. Schere, “Investigation of the Transversal Water Profile in Nafion Membranes in Polymer Electrolyte Fuel Cells,” *Journal of The Electrochemical Society,* vol. 148, pp. A183-A188, 2001.

[124] H.-L. Lin, T. L. Yu, and F.-H. Han, “A Method for Improving Ionic Conductivity of Nafion Membranes and its Application to PEMFC,” *Journal of Polymer Research,* vol. 13, pp. 379–385, 2006.

[125] N. Miyake, J. S. Wainright, and R. F. Savinell, “Evaluation of a Sol-Gel Derived

Nafion Silica Hybrid Membrane for Proton Electrolyte Membrane Fuel Cell Applications," *Journal of The Electrochemical Society,* vol. 148, pp. A898-A904, 2001.

[126] Y. Zhai, H. Zhang, J. Hu, and B. Yi, "Preparation and Characterization of Sulfated Zirconia (So42−/Zro2)/Nafion Composite Membranes For PEMFC Operation at High Temperature/Low Humidity," *Journal of Membrane Science,* vol. 280, pp. 148–155, 2006.

[127] R. Kumar, C. Xu, and K. Scott, "Graphite Oxide/Nafion Composite Membranes for Polymer Electrolyte Fuel Cells," *RSC Advances,* vol. 2, pp. 8777–8782, 2012.

[128] T. Soboleva, Z. Xie, Z. Shi, E. Tsang, T. Navessin, and S. Holdcroft, "Investigation of The Through-Plane Impedance Technique for Evaluation of Anisotropy of Proton Conducting Polymer Membranes," *Journal of Electroanalytical Chemistry,* vol. 622, no. 2, pp. 145-152, 2008.

[129] M. G.-. Cuenca, W. Zipprich, B. A. Boukamp, G. Pudmich, and F. Tietz, "Impedance Studies on Chromite-Titanate Porous Electrodes under Reducing Conditions," *Fuel Cells,* vol. 1, pp. 256-264, 2001.

[130] R. Carta, P. Jourand, B. Hermans, J. Thoné, D. Brosteaux, T. Vervust, F. Bossuyt, F. Axisa, J. Vanfleteren, and R. Puers, "Design and Implementation of Advanced Systems in a Flexible-Stretchable Technology for Biomedical Applications," *Sensors and Actuators A: Physical,* vol. 156, no. 1, pp. 79-87, 2009.

[131] S. Liu, Z. Wang, C. Yu, H. B. Wu, G. Wang, Q. Dong, J. Qiu, A. Eychmuller, and X.

W. D. Lou, “A Flexible Tio(2)(B)-Based Battery Electrode with Superior Power Rate and Ultralong Cycle Life,” *Adv Mater,* vol. 25, no. 25, pp. 3462-3467, Jul 5, 2013.

[132] J. Chen, Y. Liu, A. I. Minett, C. Lynam, J. Wang, and G. G. Wallace, “Flexible, Aligned Carbon Nanotube/Conducting Polymer Electrodes for a Lithium-Ion Battery,” *Chem. Mater,* vol. 19, pp. 3595-3597, 2007.

[133] M. H. Park, M. Noh, S. Lee, M. Ko, S. Chae, S. Sim, S. Choi, H. Kim, H. Nam, S. Park, and J. Cho, “Flexible High-Energy Li-Ion Batteries With Fast-Charging Capability,” *Nano Lett,* vol. 14, no. 7, pp. 4083-4089, Jul 9, 2014.

[134] J. Y. Choi, D. J. Lee, Y. M. Lee, Y. G. Lee, K. M. Kim, J. K. Park, and K. Y. Cho, “Silicon Nanofibrils on a Flexible Current Collector for Bendable Lithium-Ion Battery Anodes,” *Advanced Functional Materials,* vol. 23, no. 17, pp. 2108-2114, 2013.

[135] J. Liu, K. Song, P. A. V. Aken, J. Maier, and Y. Yu, “Self-Supported Li4Ti5O12-C Nanotube Arrays as High-Rate and Long-Life Anode Materials for Flexible Li-Ion Batteries,” *Nano Lett,* vol. 14, no. 5, pp. 2597-2603, May 14, 2014.

[136] S. Y. Lee, K. H. Choi, W. S. Choi, Y. H. Kwon, H. R. Jung, H. C. Shin, and J. Y. Kim, “Progress in Flexible Energy Storage and Conversion Systems, with a Focus on Cable-Type Lithium-Ion Batteries,” *Energy & Environmental Science,* vol. 6, no. 8, pp. 2414-2423, 2013.

[137] Y. H. Kwon, S.-W. Woo, H.-R. Jung, H. K. Yu, K. Kim, B. H. Oh, S. Ahn, S.-Y. Lee, S.-W. Song, J. Cho, H.-C. Shin, and J. Y. Kim, “Cable-Type Flexible Lithium Ion Battery Based on Hollow Multi-Helix Electrodes,” *Adv. Mater,* vol. 24, pp.

5192–5197, 2012.

[138] Y. Liu, S. Gorgutsa, C. Santato, and M. Skorobogatiy, “Flexible, Solid Electrolyte-Based Lithium Battery Composed of LiFePO4 Cathode and Li4Ti5O12 Anode for Applications in Smart Textiles,” *Journal of The Electrochemical Society,* vol. 159, no. 4, pp. A349-A356, 2012.

[139] E. H. Kil, K. H. Choi, H. J. Ha, S. Xu, J. A. Rogers, M. R. Kim, Y. G. Lee, K. M. Kim, K. Y. Cho, and S. Y. Lee, “Imprintable, Bendable, and Shape-Conformable Polymer Electrolytes for Versatile-Shaped Lithium-Ion Batteries,” *Adv Mater,* vol. 25, no. 10, pp. 1395-1400, Mar 13, 2013.

[140] D. Wei, S. Haque, P. Andrew, J. Kivioja, T. Ryhänen, A. Pesquera, A. Centeno, B. Alonso, A. Chuvilin, and A. Zurutuza, “Ultrathin Rechargeable All-Solid-State Batteries Based on Monolayer Graphene,” *Journal of Materials Chemistry A,* vol. 1, no. 9, pp. 3177, 2013.

[141] Y. Yang, S. Jeong, L. Hu, H. Wu, S. W. Lee, and Y. Cui, “Transparent Lithium-Ion Batteries,” *Proc Natl Acad Sci U S A,* vol. 108, no. 32, pp. 13013-8, Aug 9, 2011.

[142] S. Xu, Y. Zhang, J. Cho, J. Lee, X. Huang, L. Jia, J. A. Fan, Y. Su, J. Su, H. Zhang, H.Cheng, B. Lu, C.Yu, C. Chuang, T. I. Kim, T. Song, K. Shigeta, S. Kang, C. Dagdeviren, I. Petrov, P. V. Braun, Y. Huang, U. Paik, and J. A. Rogers, “Stretchable Batteries with Self-Similar Serpentine Interconnects and Integrated Wireless Recharging Systems,” *Nat Commun,* vol. 4, pp. 1543-1551, 2013.

[143] M. Koo, K. I. Park, S. H. Lee, M. Suh, D. Y. Jeon, J. W. Choi, K. Kang, and K. J. Lee, “Bendable Inorganic Thin-Film Battery for Fully Flexible Electronic Systems,”

Nano Lett, vol. 12, no. 9, pp. 4810-6, Sep 12, 2012.

[144] T. Pereira, R. Scaffaro, S. Nieh, J. Arias, Z. Guo, and H. T. Hahn, "The Performance of Thin-Film Li-Ion Batteries under Flexural Deflection," *J. Micromech. Microeng,* vol. 16, pp. 2714–2721, 2006.

[145] N. Kamaya, K. Homma, Y. Yamakawa, M. Hirayama, R. Kanno, M. Yonemura, T. Kamiyama, Y. Kato, S. Hama, K. Kawamoto, and A. Mitsui, "A Lithium Superionic Conductor," *Nat Mater,* vol. 10, no. 9, pp. 682-6, Sep, 2011.

[146] M. Nagao, A. Hayashi, M. Tatsumisago, T. Kanetsuku, T. Tsuda, and S. Kuwabata, "In Situ Sem Study of a Lithium Deposition and Dissolution Mechanism in a Bulk-Type Solid-State Cell With a Li2S-P2S5 Solid Electrolyte," *Phys Chem Chem Phys,* vol. 15, no. 42, pp. 18600-18606, Nov 14, 2013.

[147] H. Kitaura, A. Hayashi, K. Tadanaga, and M. Tatsumisago, "High-Rate Performance of All-Solid-State Lithium Secondary Batteries using Li4Ti5O12 Electrode," *Journal of Power Sources* vol. 189, no. 2009, pp. 145–148, 2009.

[148] K. Murata, S. Izuchi, and Y. Yoshihisa, "An Overview of the Research and Development of Solid Polymer Electrolyte Batteries," *Electrochimica Acta,* vol. 45, pp. 1501–1508, 2000.

[149] G. Jiang, S. Maeda, Y. Saito, S. Tanase, and T. Sakai, "Ceramic-Polymer Electrolytes for All-Solid-State Lithium Rechargeable Batteries," *Journal of The Electrochemical Society,* vol. 152, pp. A767-A773, 2005.

[150] J. H. Ahn, G. X. Wang, H. K. Liub, and S. X. Doub, "Nanoparticle-dispersed PEO polymer electrolytes for Li batteries," *Journal of Power Sources* vol. 119–121,

pp. 422–426, 2003.

[151] P. P. Prosini, S. Passerini, R. Vellone, and W. H. Smyrl, "V 2O 5 Xerogel Lithium–Polymer Electrolyte Batteries," *Journal of Power Sources,* vol. 75(1), pp. 73-83, 1998.

[152] F. Croce, and B. Scrosati, "Interfacial Phenomena in Polymer-Electrolyte Cells: Lithium Passivation and Cycleability," *Journal of Power Sources. ,* vol. 43, pp. 9-19, 1993.

[153] H. Y. Sun, H. J. Sohn, O. Yamamoto, Y. Takeda, and N. Imanishi, "Enhanced Lithium-Ion Transport in PEO-Based Composite Polymer Electrolytes with Ferroelectric BaTiO," *Journal of The Electrochemical Society,* vol. 146, pp. 1672-1676, 1999.

[154] K. S. Ji, H. S. Moon, J. W. Kim, and J. W. Park, "Role of Functional Nano-Sized Inorganic Fillers in Poly(Ethylene) Oxide-Based Polymer Electrolytes," *J Power Sources,* vol. 117, pp. 124–130, 2003.

[155] Q. Li, and H. Ardebili, "Atomistic Investigation of the Nanoparticle Size and Shape Effects on Ionic Conductivity of Solid Polymer Electrolytes," *Solid State Ionics,* vol. 268, pp. 156–161, 2014.

[156] B. Kumar, and L. G. Scanlon, "Polymer-Ceramic Composite Electrolytes," *Journal of Power Sources,* vol. 52, pp. 261-268, 1994.

[157] J. J. Xu, K. Wang, S.-Z. Zu, B.-H. Han, and Z. Wei, "Hierarchical Nanocomposites of Polyaniline Nanowire Arrays on Graphene Oxide Sheets with Synergistic Effect for Energy Storage," *Acs Nano,* vol. 4, pp. 5019-5026, 2010.

[158] C. Tang, K. Hackenberg, Q. Fu, P. M. Ajayan, and H. Ardebili, "High Ion

Conducting Polymer Nanocomposite Electrolytes Using Hybrid Nanofillers," *Nano Letters* vol. 12 (3), pp. 1152–1156, 2012.

[159] M. Kammoun, S. Berg, and H. Ardebili, "Flexible Thin-Film Battery Based on Graphene-Oxide Embedded in Solid Polymer Electrolyte," *Nanoscale,* vol. 7, pp. 17516–17522, 2015.

[160] B. Sun, Y.-Z. Long, Z.-J. Chen, S.-L. Liu, H.-D. Zhang, J.-C. Zhang, and W.-P. Han, "Recent Advances in Flexible And Stretchable Electronic Devices Via Electrospinning," *Journal of Materials Chemistry C,* vol. 2, no. 7, pp. 1209-1219, 2014.

[161] C. Yan, and P. S. Lee, "Stretchable Energy Storage and Conversion Devices," *Small*, pp. 1-17, 2014.

[162] K. Somasundaram, E. Birgersson, and A. S. Mujumdar, "Thermal–Electrochemical Model for Passive Thermal Management of a Spiral-Wound Lithium-Ion Battery," *Journal of Power Sources,* vol. 203, pp. 84-96, 2012.

[163] Y.-E. Hyung, S.-I. Moon, D.-H. Yum, and S.-K. Yun, "Fabrication and Evaluation of 100 Ah Cylindrical Lithium Ion Battery for Electric Vehicle Applications," *Journal of Power Sources,* vol. 81–82, pp. 842–846, 1999.

[164] C. A. Vincent, "Lithium batteries: a 50-year perspective, 1959–2009," *Solid State Ionics,* vol. 134, pp. 159–167, 2000.

[165] J. Wang, H. K. Liu, S. X. Dou, S. Zhong, Y. Zhu, and C. Fub, "Enhanced Performance of VRLA Batteries with a Novel Spirally-Wound Electrode Design," *Journal of Power Sources,* vol. 113, pp. 241–244, 2003.

[166] S. Han, K. S. Hwang, Y. K. Yoo, S.-M. Lee, and J. H. Lee, "Flexible and

Stretchable Energy Harvesting Device Using Three-Dimensional Poly(Dimethylsiloxane)," *Japanese Journal of Applied Physics,* vol. 53, no. 8S3, pp. 08NC01-1-4, 2014.

[167] G. Kettlgruber, M. Kaltenbrunner, C. M. Siket, R. Moser, I. M. Graz, R. Schwödiauer, and S. Bauer, "Intrinsically Stretchable and Rechargeable Batteries for Self-Powered Stretchable Electronics," *Journal of Materials Chemistry A,* vol. 1, no. 18, pp. 5505-5508, 2013.

[168] Z. Song, T. Ma, R. Tang, Q. Cheng, X. Wang, D. Krishnaraju, R. Panat, C. K. Chan, H. Yu, and H. Jiang, "Origami Lithium-Ion Batteries," *Nat Commun,* vol. 5, pp. 3140-3146, 2014.

[169] A. M. Gaikwad, A. M. Zamarayeva, J. Rousseau, H. Chu, I. Derin, and D. A. Steingart, "Highly Stretchable Alkaline Batteries Based on an Embedded Conductive Fabric," *Adv Mater,* vol. 24, no. 37, pp. 5071-5077, Sep 25, 2012.

[170] Y. Zhang, W. Bai, J. Ren, W. Weng, H. Lin, Z. Zhang, and H. Peng, "Super-Stretchy Lithium-Ion Battery Based on Carbon Nanotube Fiber," *Journal of Materials Chemistry A,* vol. 2, no. 29, pp. 11054-11059, 2014.

[171] C. Wang, W. Zheng, Z. Yue, C. O. Too, and G. G. Wallace, "Buckled, Stretchable Polypyrrole Electrodes for Battery Applications," *Adv Mater,* vol. 23, no. 31, pp. 3580-3584, Aug 16, 2011.

[172] H. L. Filiatrault, G. C. Porteous, R. S. Carmichael, G. J. Davidson, and T. B. Carmichael, "Stretchable Light-Emitting Electrochemical Cells using an Elastomeric Emissive Material," *Adv Mater,* vol. 24, no. 20, pp. 2673-2681, May 22, 2012.

[173] M. Kammoun, S. Berg, and H. Ardebili, “Stretchable Spiral Thin-Film Battery Capable of Out-Of-Plane Deformation,” *Journal of Power Sources,* vol. 332, pp. 406-412, 2016.

[174] J. Newman, and W. Tiedemann, “Potential and Current Distribution in Electrochemical Cells Interpretation of the Half-Cell Voltage Measurements as a Function of Reference-Electrode Location,” *J. Electrochem. Soc.,* vol. 140, pp. 1962-1968, 1993.

[175] M. Guo, G. Sikha, and R. E. White, “Single-Particle Model for a Lithium-Ion Cell: Thermal Behavior,” *Journal of The Electrochemical Society,* vol. 158, no. 2, pp. A122-132, 2011.

[176] D. Danilov, R. A. H.Niessen, and P. H. L. Notten, “Modeling All-Solid-State Li-Ion Batteries,” *Journal of The Electrochemical Society,* vol. 158, no. 3, pp. A215-A222, 2011.

[177] A. G. Evans, and J. W. Hutchinson, “A Critical Assessment of Theories of Strain Gradient Plasticity,” *Acta Materialia,* vol. 57, no. 5, pp. 1675-1688, 2009.

[178] A. Barré, B. Deguilhem, S. Grolleau, M. Gérard, F. Suard, and D. Riu, “A Review On Lithium-Ion Battery Ageing Mechanisms and Estimations for Automotive Applications,” *Journal of Power Sources,* vol. 241, pp. 680-689, 2013.

[179] J. Vetter, P. Novák, M. R. Wagner, C. Veit, K. C. Möller, J. O. Besenhard, M. Winter, M. Wohlfahrt-Mehrens, C. Vogler, and A. Hammouche, “Ageing Mechanisms in Lithium-Ion Batteries,” *Journal of Power Sources,* vol. 147, no. 1-2, pp. 269-281, 2005.

[180] G. supermaket, "Graphene Oxide," G. Laboratories, ed., 2016.

[181] Lenntech. "Adsorption / Active Carbon,"

http://www.lenntech.com/library/adsorption/adsorption.htm.

[182] Inc.Atmospure. "What is Activated Carbon?,"

http://www.atmospure.com/CaseStudies/ActivatedCarbonAbsorption.html.

Appendix A

Calculation of the Lithium salt ($LiClO_4$) weight

Li : EO =1:16

Mw($LiClO_4$)=106.5 g/mol

Mw(PEO)=100,000g/mol

Mw(EO)=44 g/mol

$$m(LiClO_4) = \frac{m(PEO)}{Mw(PEO)} * \frac{Mw(PEO)}{Mw(LiClO_4) * Mw(EO)} * Mw(LiClO_4)$$

for m(PEO)= 2g we have m(LiClO4) =0.3 g

Filler weight calculation For the Solid polymer electrolyte

$$\frac{\mathrm{m(filler)}}{\mathrm{m(PEO) + m(LiClO4) + m(filler)}} = 1\%\ or\ 2\%\ etc.$$

m(filler) is the weight of filler.

Production of Graphene Oxide

The graphene oxide (GO) nanoscale powder was purchased from the Graphene Supermarket. According to the company's technical sheet, the GO powder was synthesized using the Hummers method. [180] The Hummers approach consists of producing the oxidized form of the graphite with a mixture of sulfuric acid, sodium nitrate, and potassium permanganate to obtain graphene oxide.

Structurally, GO has oxygen-containing groups and due to the high affinity to water molecules of these groups, GO is hydrophilic and can be dissolved in water. The

solubility in water and other solvents facilitates the deposition of the thin films containing the GO. Graphene oxide is a poor electrical conductor, and is thus, suitable as a filler material in the polymer electrolyte.

Table A.S1: Fitting parameters of the equivalent circuit for the ionic conductivity calculation

			Circuit components				Thickness	Area	σavg (S/cm)
		N	R1(Ohm)	R2(Ohm)	C(F)	W(Mho)	(mm)	(mm2)	
PEO	Sample 1	1	1113.90	188080.00	4.852*10-11	2.00*10-07			
		2	1100.10	162390.00	4.848*10-11	2.11*10-07	0.307		
		3	1085.60	43430.00	4.852*10-11	2.23*10-07			
	Sample 2	1	1133.00	60640.00	4.590*10-11	1.38*10-07			
		2	1148.70	193860.00	4.604*10-11	1.26*10-07	0.293		5.62*10-08
		3	1109.30	133500.00	4.583*10-11	1.52*10-07			
	Sample 3	1	8127.00	163740.00	1.209*10-10	2.23*10-07	0.144		
		2	691.07	2849.00	8.678*10-11	2.52*10-07			
		3	669.62	69689.00	8.679*10-11	2.72*10-07			
PEO+1%GO	Sample1	1	350.18	7498.60	1.528*10-10	1.18*10-06			
		2	329.88	5766.60	1.567*10-10	1.33*10-06			
		3	312.15	4834.00	1.589*10-10	1.50*10-06	0.126		
		4	295.38	4000.30	1.613*10-10	1.71*10-06		283.385	
	Sample2	1	5171.90	116800.00	1.052*10-10	4.56*10-07			
		2	5171.90	116800.00	1.052*10-10	4.56*10-07			
		3	778.23	87773.00	8.297*10-11	4.59*10-07			
		4	741.22	67511.00	8.195*10-11	5.16*10-07	0.146		
		5	700.67	51123.00	8.132*10-11	6.06*10-07			
		6	675.23	41707.00	8.122*10-11	6.93*10-07			4.20*10-07
		7	652.67	34902.00	8.145*10-11	7.84*10-07			
		8	634.23	29743.00	8.181*10-11	8.70*10-07			
	Sample3	1	1115.20	102010.00	3.204*10-11	6.84*10-07			
		2	1086.40	71746.00	3.192*10-11	7.50*10-07			
		3	1012.20	55328.00	3.196*10-11	8.34*10-07	0.3221		
		4	941.01	45960.00	3.209*10-11	9.28*10-07			
		5	925.27	40055.00	3.228*10-11	1.00*10-06			
		6	884.98	34393.00	3.253*10-11	1.11*10-06			
		7	872.91	1524.00	3.272*10-11	1.17*10-06			

Characteristics of the Activated Carbon

The activated carbon nano-powder features a high specific surface area of SSA>1300m^2/g with high activation and dispersion and iodine adsorption capability >1250mg/g. [111, 181, 182]

Filler Weight Calculation

The weight of the filler X_f is measured according to the following equation:

$$\frac{X_f}{X_f + W_{pure\ Nafion}} = \text{Spf\%},$$

where

Spf% is the specific filler percentage

X_f is the weight of the filler (g)

$W_{\text{pure Nafion}}$ is the weight of the pure Nafion membrane (g)

The total weight of the pure Nafion membrane or $W_{\text{pure Nafion}}$ is 1.1312 g and the experimental loadings of the AC filler are 0.0053 g, 0.0079 g, 0.0115 g, 0.0241 g, 0.0349 g and 0.0610 g, corresponding to the following filler percentages 0.5%, 0.7%, 1%, 2%, 3%, 5%, respectively.

Table A.S2. Fitting parameters of the ionic conductivity model

σ_0 (mS/cm)	A (mS/cm)	q	p	B (mS/cm)	n	m	t
0.4933	3.5	0.007	1000	2	6.0 $\times 10^{-8}$	1700	33

Appendix B

Flexible Thin-Film Battery based on Graphene-Oxide Embedded in Solid Polymer Electrolyte

Table B.S1: Material properties and performance of flexible LIB

	Battery 1	Battery 2	Battery 3	Battery 4
Electrode (Anode/ Cathode*)	Graphite/ $LiCoO_2$			
Current Collector (Thickness)	Cu(9 μm)/Al Foil (15 μm)			
Electrolyte	PEO	PEO	PEO+1 wt% GO	PEO+1 wt% GO
Weight (g)	0.2997	0.2816	0.2913	0.2973
Plasticizer Weight (%)**	0.0211g (7%)	0.0158g (6%)	0.0132g (5%)	0.0171g (6%)
Seal Type	Plastic Seal Lamination			
Battery Dimension (L×W×T) (mm)	20.47×20.53×0.742	20.54×20.18×0.732	21.25×21.24×0.722	20.65×20.76×0.778
Battery Weight (g)	1.125	1.132	1.418	1.045
Capacity (mAh/cm^2)	0.084	0.099	0.093	0.129
Capacity Fading (%)	31%	25%	51%	12%
Output Voltage (V)	2.787	2.800	2.910	2.870
Energy Density (mWh/cm^3)	3.173	3.821	3.742	4.757
(Wh/kg)	0.837	0.988	0.762	1.417
Power Density (mW/cm^3)	9.391	9.563	10.076	9.222
(W/kg)	2.477	2.473	2.053	2.748
Bending Radius (mm)	Flat	18.9	Flat	18.9

*$LiCoO_2$: Density (200-225 g/m^2)
Graphite: Density (80 g/m^2)
**$LiPF_6$: Density (1.22 g/ml at 25°C)

Finite Element Analysis

Finite element analysis (FEA) was conducted to model the bending of the battery using Abaqus 6.13-5 software. This software package offers extensive element, material modeling and contact formulation options. The layers of the battery were stacked initially in contact and modeled as a 20x20 mm^2 area section. The thicknesses of each battery layer and the materials were modeled based on the experiment, and a linear elastic material model was created. Two different solid polymer electrolytes were modeled numerically: PEO and PEO/1 wt% GO. The finite element analysis was performed for the lamination/encapsulation followed by bending.

All layers besides the electrolyte were modeled with CPS4I elements. These elements contain additional shape functions that allow the bending curvature and strain field of each element to accurately model the deflection. Mesh refinement was completed to ensure that the bending for the modeled radius was accurate. The electrolyte was modeled using CPS8 elements, which are quadratic full integration elements capable of properly modeling bending, and are not susceptible to locking like first order elements during the high deflection experienced from the lamination step due to the low stiffness of the electrolyte material. The interactions between each layer, with the exception of the electrolyte contact, were modeled with bonded contact to simulate adhesion between the layers. The electrolyte contact was modeled as frictionless, between the electrolyte/anode and electrolyte/cathode layers, in order to minimize the addition of shear stress between the layers and any axial stress from lateral expansion during compression. This expansion was thought to be significant since the electrolyte material is much less stiff than the other materials.

The lamination/encapsulation of the battery produces initial compressive stresses in the battery layers. The final thickness of the battery with each type of electrolyte is 0.75mm. The battery is compressed in the initial steps of the analysis using a combination of displacement, followed by surface pressure to maintain the thickness in the battery of 0.75mm. It is noted that the contact pressure between the layers is greater in the battery with the composite electrolyte, compared to that of pure PEO based battery. The lamination process results in a final measured battery thickness of 0.75mm in both batteries after lamination. Since the composite electrolyte is initially thicker than the PEO electrolyte, more compression is required to produce the final 0.75mm thickness for the composite electrolyte, which causes increased contact pressure. Furthermore, since the composite material is stiffer and has a higher elastic modulus than the PEO electrolyte, it is less compliant and requires greater force to compress the composite electrolyte battery to the final lamination thickness, which is accompanied by a further increase in the contact pressures after lamination.

The finite element analysis of the LIB bending was carried out after the encapsulation process, in order to account for the real effects associated with the lamination compression. No delamination is predicted to occur for a bending radius of 17 mm, verified through experiment. The FEA results show that the contact pressure increases as the bending is applied to the flexible battery.

Table B.S2: Materials Properties used in FEA

Materials	E (MPa)	ν
Aluminum	68947.6	0.334
Copper	117210.9	0.355
Laminate	4895.3	0.38
$LiCoO_2$	135800	0.306
Graphite	14665	0.2355
PEO	10.82	0.3
PEO/1 wt% GO	33.45	0.3

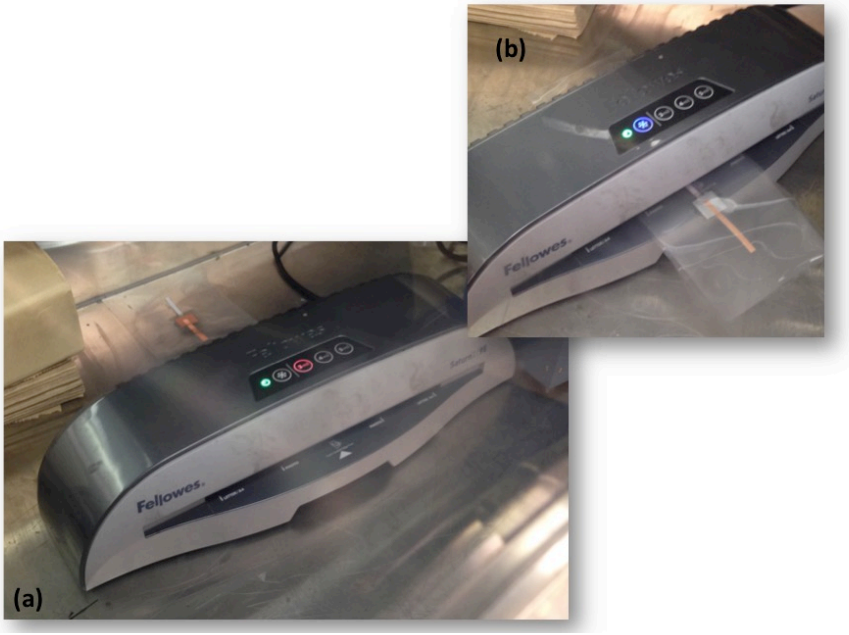

Figure B. S1: Lamination process: **(a)** first layer and **(b)** second layer lamination.

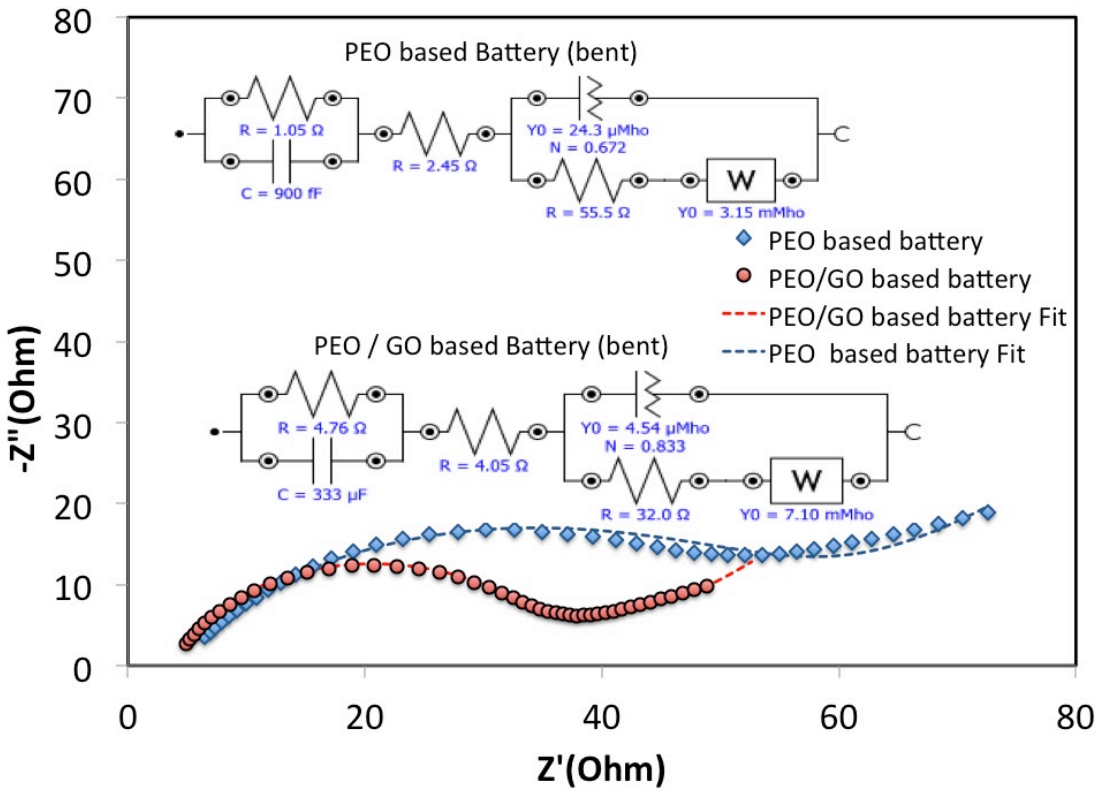

Figure B.S2: (a) Impedance spectra of bent flexible LIB based on pure PEO and PEO/1 wt% GO, under fixed bending radius of 18.9 mm in fresh condition.

The capacity retention of the flexible LIB at different current rates is displayed in **Figure B.S3**. The electrochemical performance of the LIBs can be attributed to the structural and electrochemical stability of the polymer-based electrolyte. Even at the current rate of 1.1mA, the flexible battery based on the polymer nanocomposite electrolyte in bending position can deliver high discharge capacity of 0.122 mAh cm^{-2} after 50 cycles. This is far superior to the battery based on pure PEO, which exhibits a capacity of 0.059 mAh cm^{-2} after 50 cycles.

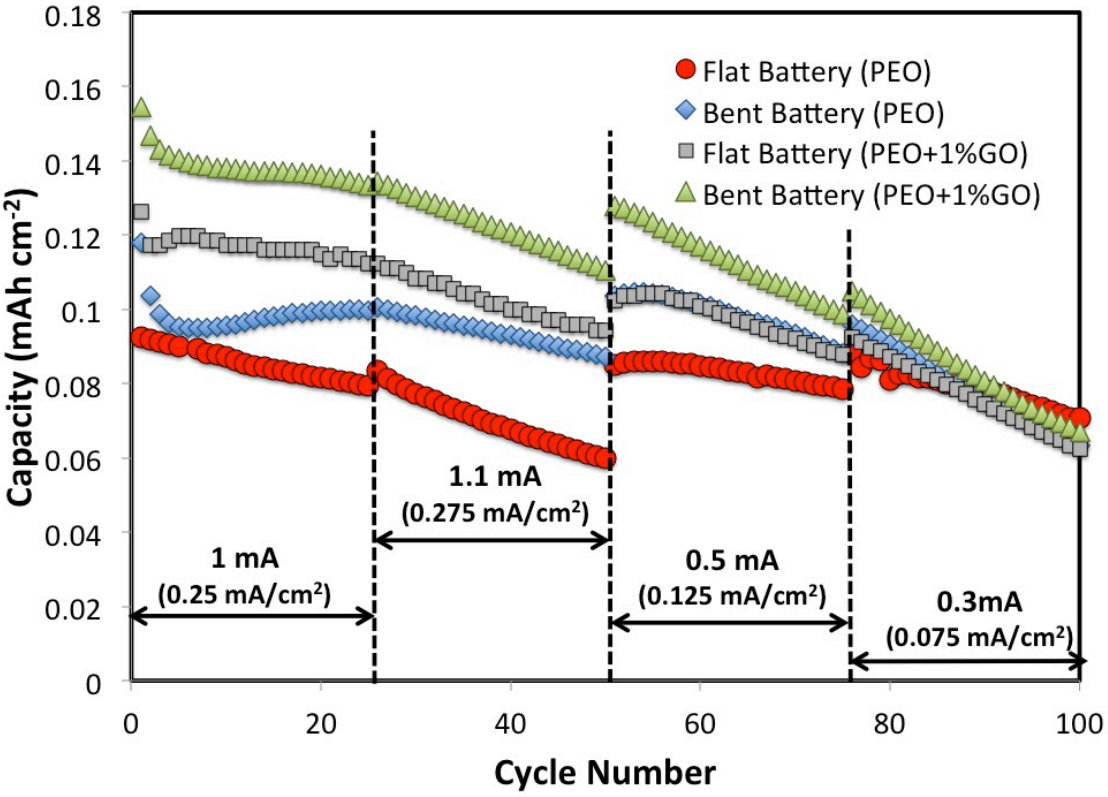

Figure B.S3: Capacity retention of the flexible LIB in flat and bending configurations at different current rates (25 cycles per rate)

The behavior of the charge and discharge cycling for the four different batteries is presented in **Figure B. S4**. The plot shows that the capacities for all batteries decrease but at different rates of fading. For example, the capacity varies from 0.091 mAh cm^{-2} for the flat battery based on the pure PEO film to 0.141 mAh cm^{-2} for battery using the same electrolyte but in bending position during the first cycle. Further charge -discharge cycles resulted in capacities of 0.065 mAh cm^{-2} and 0.087 mAh cm^{-2} with 31% and 25% capacity fading between the first and the last cycles for flat battery and bent battery with pure electrolyte, respectively. The capacity fading in Li ion batteries is generally caused by the loss of primary active material (Li^{+}) and it can be attributed to lithium metal

deposition, electrolyte decomposition, active material dissolution, phase transition of electrode materials, and passive layer formation on the electrode and current collectors. From **Table B.S1**, the highest values of capacity fading are associated with the batteries made with pure polymer electrolyte. This suggests that the GO fillers may increase the electrolyte stability and improve the battery cyclability.

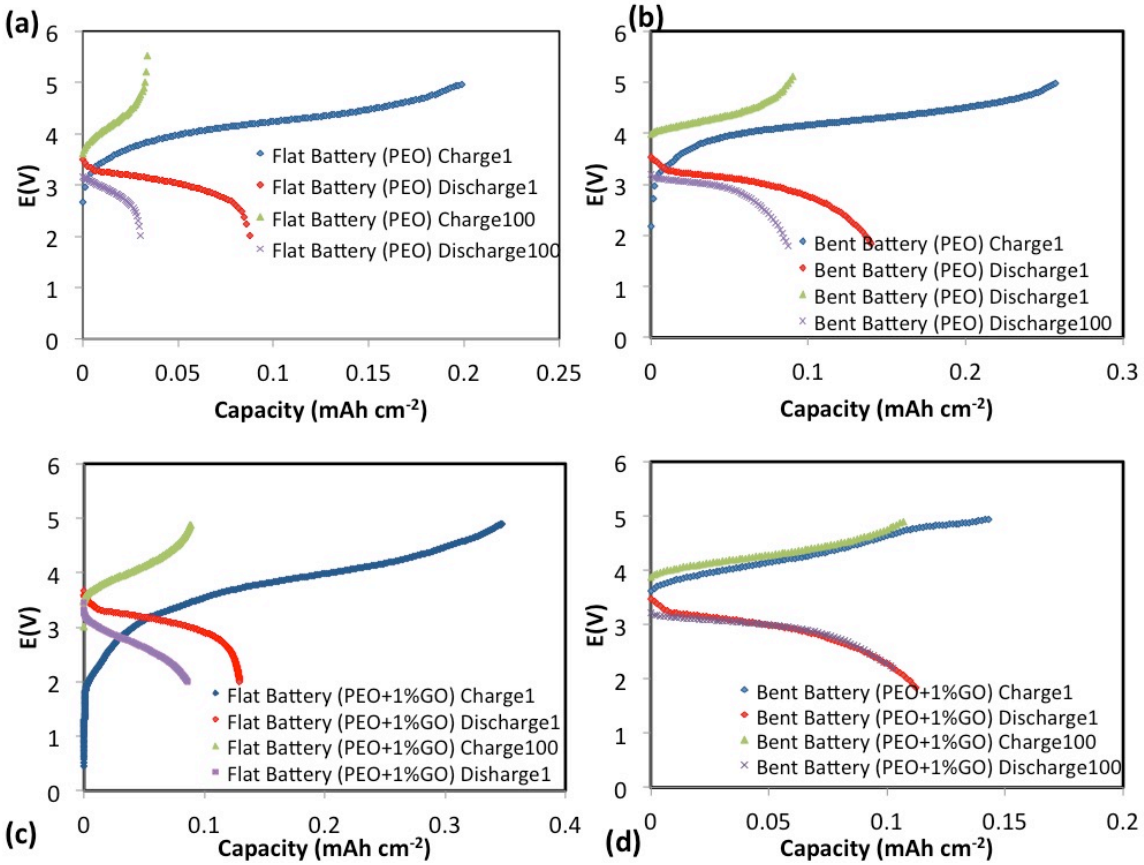

Figure B. S4: Charge and discharge behavior of thin-film LIBs at the 1st and 100th cycle for (a) flat battery (PEO), (b) bent battery (PEO), (c) flat battery (PEO/1 wt% GO), and (d) bent battery (PEO/1 wt% GO).

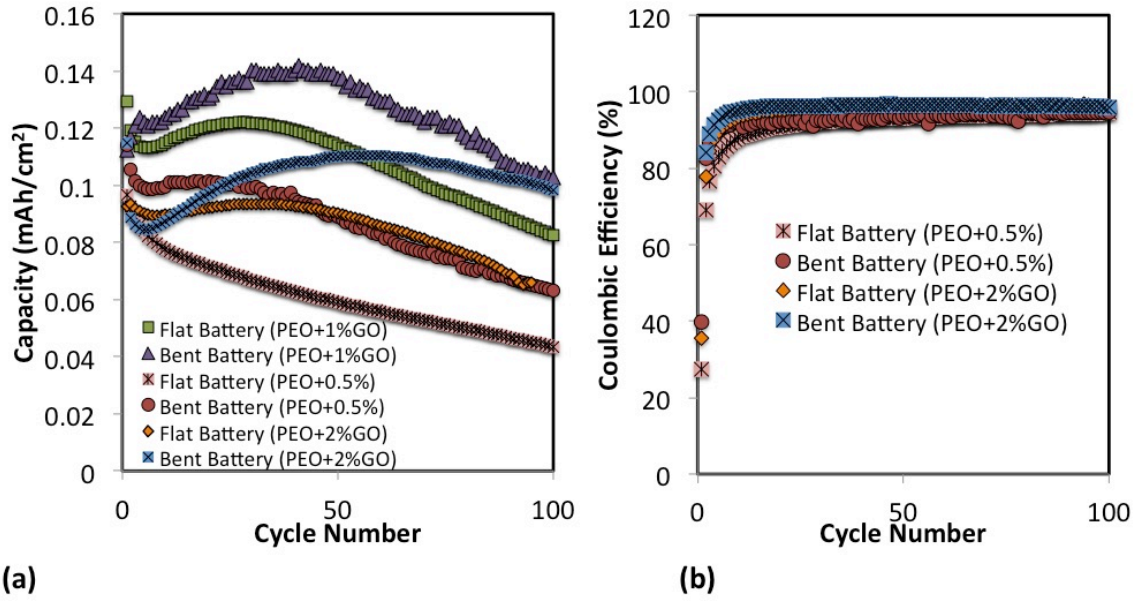

Figure B.S5: **(a)** Discharge capacity retention as a function of bending state and electrolyte type at a constant current rate of 1 mA during 100 cycles, and **(b)** coulombic efficiencies of the flexible batteries.

The capacities of four batteries made with composite electrolyte with different percentages of GO filler under fixed bending radius are shown in **Figure B.S5**. **Figure B.S5.a** indicates that the highest capacities were recorded for the batteries made of electrolyte with 1 wt% GO. All batteries that are in bending position show higher average capacities compared to the flat batteries based on the same electrolyte. The flat battery using the electrolyte with minimum filler percentage (0.5 wt% GO) exhibits the lowest capacity and it shows similar behavior to the battery made with pure electrolyte. The batteries made with 1 wt% GO composite electrolyte exhibit the highest capacity compared to the other composite electrolyte under the same testing conditions. Adding GO particles to the polymer electrolyte can enhance the bulk conductivity, which can affect the capacity of the flexible battery. GO particles reduce the crystallinity of PEO, and the highly amorphous structures can better facilitate ion transport in polymer

electrolytes. Adding high percentage of nanofiller may decrease the ionic conductivity of polymer electrolyte due to adverse effects like aggregation, blocking and ion trapping. Therefore, relatively low filler content (i.e., 1 wt% GO) can ensure optimal ion conductivity. **Figure B.S5.b** presents the coloumbic efficiency of the four flexible batteries. All flexible batteries demonstrate highly stable efficiencies (higher than 91% after stabilization) under the same testing conditions.

The comparative adhesion between the different layers of the thin film battery was investigated through the method of shear by tensile loading. After disassembling the battery, high strength bonding tape (3M VHB Tape) was used to fix the two layers in question to the self-tightening wedge grips of a motorized mechanical testing stand Mark-10-ESM301L. The results of the test (at peeling speed of 1 mm/minute) are presented in **Figure B.S6**. According to **Figure B.S6 a and b,** the highest maximum load applied before sliding/shear was recorded between the electrode layer ($LiCoO_2$) and the current collector (Al) and the lowest load was noted between the two encapsulant layers. A good adhesion between the electrolyte and the electrodes layer was verified. In the case of the interfaces between the electrode layer ($LiCoO_2$)/the current collector (Al) and electrode layer (Graphite)/the current collector (Cu), no shear/sliding could be observed at the maximum tension load applied by the machine (marked by ***** in **Figure B. S6a**).

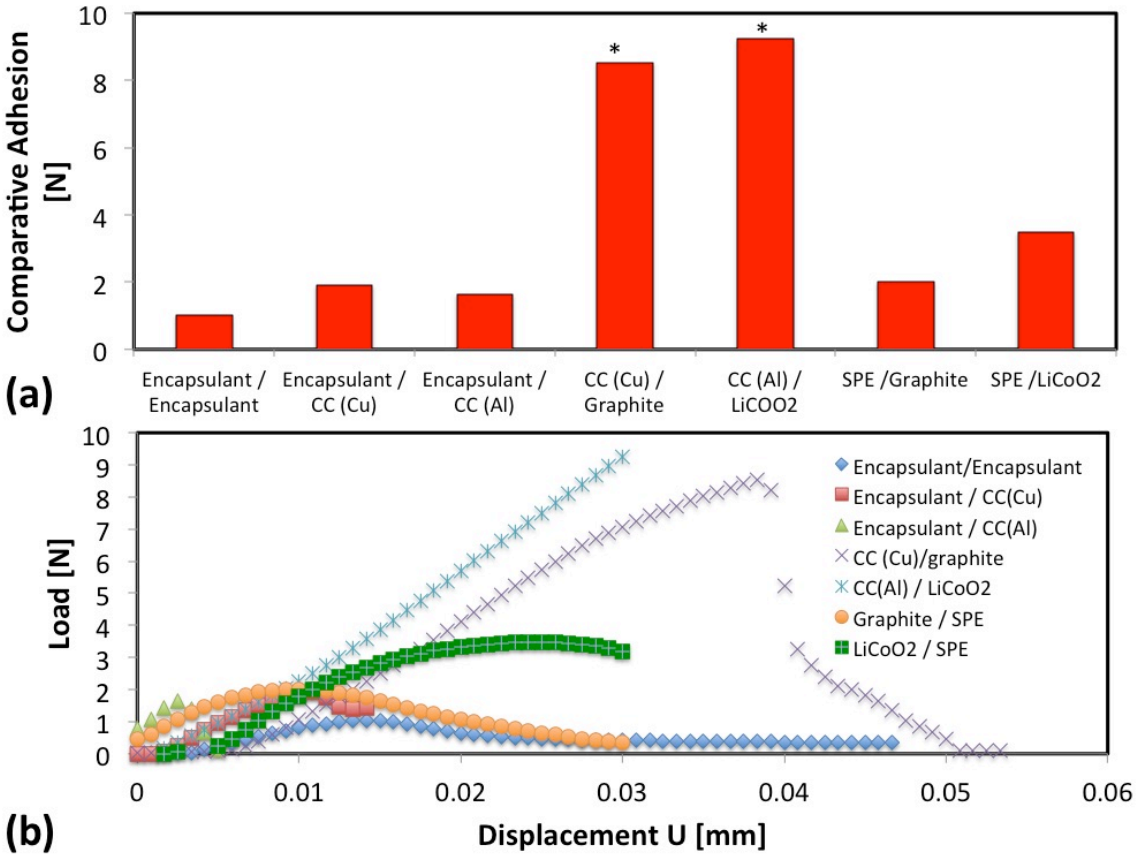

Figure B.S6: (a) Maximum tension load recorded before sliding/shear occurs and **(b)** displacement load profile between the different layers of the thin film battery.

Appendix C

Stretchable Thin-Film Spiral Battery Capable of Large Out-of-Plane Deformation

Properties of the Spiral Lithium-Ion Battery

Table C.S1 illustrates the characteristics of 3 spiral LIBs under fixed stretching conditions. All batteries were made with solid PEO+1%GO electrolyte.

Table C.S1: Typical material and physical properties of the spiral battery

		Battery1	Battery2	Battery3
Electrodes	Anode/ Cathode	Graphite/ $LiCoO_2$		
Current Collector		Cu/Al foil with a thickness of 10-30 μm		
Electrolyte		Solid PEO/1%GO/$LiClO_4$ (5 wt.% liquid $LiPF_6$ added to the electrode surface during the battery assembly)		
Seal & Format		Plastic seal, lamination		
Battery Area (cm^2)		9.09	9.09	9.09
Battery Thickness (mm)		0.735	0.746	0.755
Capacity (mAh/cm^2)		0.118	0.1052	0.0708
Capacity Fading (%)		22%	38%	53%
Output Voltage (V)		3.433	3.448	3.409
Energy Density (mWh/cm3)		5.520	4.862	3.196
Power Density (mW/cm3)		5.138	5.135	5.077
Stretching Distance		NA	5 mm	10 mm

Finite Element Analysis

Finite element analysis (FEA) was conducted to model the extension of the spiral battery using Abaqus 6.13-5 software. This software package offers extensive element,

material modeling and contact formulation options. The layers of the battery were stacked initially in contact and modeled in a spiral pattern with uniform prismatic cross-sections. The thicknesses of each battery layer and the materials were modeled based on the experiment, and a linear elastic material model was created. The finite element analysis was performed with the lamination/encapsulation of the battery followed by bending.

All layers were modeled with C3D20 elements. These are higher order elements that are capable of modeling the large strains and kinematics associated with the types of loading for this stretchable battery. Mesh refinement was completed to ensure that proper mesh convergence was achieved. The interactions between each layer were modeled with bonded contact to simulate adhesion between the layers. The lamination/encapsulation of the battery produces initial compressive stresses in the battery layers. The battery is compressed in the initial steps of the analysis using a combination of displacement, followed by surface pressure.

The purpose of the finite element analysis of the spiral battery was to determine the state of stress in the battery during the extension process. A fixed displacement boundary condition was applied to the outer end of the spiral to prevent it from movement during extension, and to provide a reaction point during the application of the extension load. The extension load was in the form of a displacement at the innermost part of the spiral of 200mm in the axial direction. After encapsulation, the extension was applied to the battery. Nodal forces were selected as a field output in order to obtain the magnitude and direction of net resultant nodal forces resulting from element stress during load application. At cross-sections of interest along the spiral length the net forces and

moments with respect to a local coordinate system and the cross-sectional centroid were determined via the program by accounting for the resulting directional nodal force variation through the cross-section due to element stress. This allowed us to determine the effects of torsion, the stress distribution and the change in local bending moment throughout the spiral with respect to the local moment arm: location along the spiral. The results of the analysis show that the stress distribution is more uniform throughout the spiral, though the local torsional and bending moments vary along the spiral, which is expected as the moment arm increases radiating outward on the spiral. The axial displacement and extension also follows this same pattern since this loading is directly related to the distribution of material during the loading.

Appendix D

Temperature Effects in Nanocomposite Polymer Based Lithium-Ion Batteries

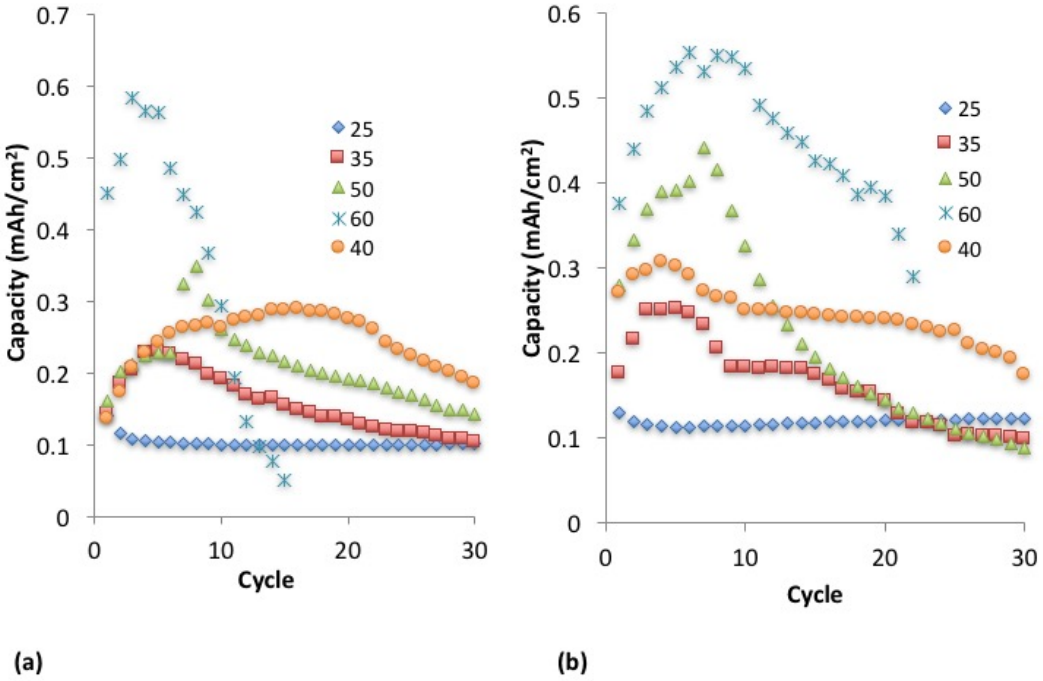

Figure D.S1: High Temperature cycling profile of the flexible batteries based (a) on pure PEO|$LiClO_4$ and (b) nanocomposite polymer PEO|LiClO4|GO